Advanced Schemes for Surface Plasmon Resonance and Plasmon-enhanced Fluorescence Biosensors

Dissertation
zur Erlangung des Grades
"Doktor der Naturwissenschafen"

am Fachbereich Biologie
der Johannes Gutenberg-Universität
in Mainz

vorgelegt von

Chun-Jen Huang
aus Changhua, TAIWAN

Mainz, November, 2010

Dekan: Prof. Dr. Erwin Schmidt

1. Berichterstatter: Prof. Dr. H. Paulsen

2. Berichterstatter: Prof. Dr. W. Knoll

3. Prüfer: Prof. Dr. N. Hellmann

4. Prüfer: Prof. Dr. C. Bubeck

Tag der mündlichen Prüfung: 24, November 2010

Die vorliegende Arbeit wurde unter Betreuung von Prof. Dr. W. Knoll und Dr. J. Dostalek im Zeitraum zwischen October 2007 bis November 2010 am Max-Planck-Institute für Polymerforschung, Mainz, Deutschland, und Austrian Institute of Technology, Wien, Österreich angefertigt.

To my Family and Yu-Chun

Abstract

Advanced optical biosensor platforms exploiting long range surface plasmons (LRSPs) and responsive N-isopropylacrylamide (NIPAAm) hydrogel binding matrix for the detection of protein and bacterial pathogen analytes were carried out. LRSPs are optical waves that originate from coupling of surface plasmons on the opposite sites of a thin metallic film embedded between two dielectrics with similar refractive indices. LRSPs exhibit orders of magnitude lower damping and more extended profile of field compared to regular surface plasmons (SPs). Their excitation is accompanied with narrow resonance and provides stronger enhancement of electromagnetic field intensity that can advance the sensitivity of surface plasmon resonance (SPR) and surface plasmon-enhanced fluorescence spectroscopy (SPFS) biosensors. Firstly, we investigated thin gold layers deposited on fluoropolymer surface for the excitation of LRSPs. The study indicates that the morphological, optical and electrical properties of gold film can be changed by the surface energy of fluoropolymer and affect the performance of a SPFS biosensor. A photo-crosslinkable NIPAAm hydrogel was grafted to the sensor surface in order to serve as a binding matrix. It was modified with bio-recognition elements (BREs) via amine coupling chemistry and offered the advantage of large binding capacity, stimuli responsive properties and good biocompatibility. Through experimental observations supported by numerical simulations describing diffusion mass transfer and affinity binding of target molecules in the hydrogel, the hydrogel binding matrix thickness, concentration of BREs and the profile of the probing evanescent field was optimized. Hydrogel with a up to micrometer thickness was shown to support additional hydrogel optical waveguide (HOW) mode which was employed for probing affinity binding events in the gel by means of refractometric and fluorescence measurements. These schemes allow to reach limits of detection (LODs) at picomolar and femtomolar levels, respectively. Besides hydrogel based experiments for detection of molecular analytes, long range surface plasmon-enhanced fluorescence spectroscopy (LRSP-FS) was employed for detection of bacterial pathogens. The influence of capture efficiency of bacteria on surfaces and the profile of the probing field on sensor response were investigated. The potential of

LRSP-FS with extended evanescent field is demonstrated for detection of pathogenic *E. coli* O157:H7 on sandwich immunoassays . LOD as low as 6 cfu mL^{-1} with a detection time of 40 minutes was achieved.

List of abbreviation

ACFDP	the Advisory Committee for Food and Dairy Products
ACT	Acetate buffer
AFM	Atomic force microscopy
AIBN	2,2'-Azobis(isobutyronitrile)
Benzophenone-thiol	S-3-(benzoylphenoxy) propyl ethanolthioate
β-hCG	human chorionic gonadotrophin-β subunit
BIA	Biomolecular interaction analysis
Biotin-thiol	Biotin-terminated triethylene glycol mono-11-mercaptoundecyl ether
BRE	Bio-recognition element
CCD	Charge-couple device
CDC	the Centers for Disease Control
cfu	Colony forming unit
COOH-dithiol	Dithiolalkanearomatic PEG6-COOH
cps	Count per second
Cyt	Cytop
DLS	Dynamic light scattering
DNA	Deoxyribonucleic acid
E. coli	*Escherichia coli*
EDC	1-Ethyl-3-[3-dimethylaminopropyl]carbodiimide hydrochloride
EG	Ethylene glycol
ELISA	Enzyme linked immunosorbent assay
FWHM	Full width of half maximum
hCG	human chorionic gonadotrophin
HEMA	2-hydroxyethyl methacrylate
HOW	Hydrogel optical waveguide
IUPAC	International Union of Pure and Applied Chemistry
LED	Light-emitting diode

LOD	Limit of detection
LRSP	Long range surface plasmon
LRSP-FS	Long range surface plasmon-enhanced fluorescence spectroscopy
MAA	Methacrylic acid
NHS	N-hydroxysulfosuccinimide
NIPAAm	N-isopropylacrylamide
P2VP	Poly(2-vinylpyridine)
PAEMA	Poly(2-aminoethyl methacrylate)
PBS	Phosphate buffered saline
PBST	Phosphate buffered saline containing 0.05% Tween 20
PDE	Partial differential equation
PEG	Poly(ethylene glycol)
PEG-dithiol	Dithiolalkanearomatic PEG3-OH
PEG-thiol	Triethylene glycol mono-11-mercaptoundecyl ether
PNA	Peptide nucleic acid
PSA	Prostate-specific antigen
PVA	Poly(vinylalcohol)
RIU	Refractive index unit
RMS	Root-mean-square
SA	Streptavidin
SAM	Self-assembled monolayer
SD	Standard deviation
SMA	Sodium methacrylate
SP	Surface plasmon
SPFS	Surface plasmon field-enhanced fluorescence spectroscopy
SPR	Surface plasmon resonance
SRSP	Short range surface plasmon
TE	Transverse electric
TFPS	para-tetrafluorophenol-sulfonate
TM	Transverse magnetic

Contents

Contents

1 Introduction

1.1 Biosensors

The first biosensor device was demonstrated by Updike and Hicks [1] for detection of glucose in the last century. Since then, wide range of biosensor technologies were developed and applied in medical diagnostics (e.g. detection of disease markers), food control (e.g. detection of food borne pathogens and toxins) or environmental monitoring (e.g. detection of pollutants). According to the definition of International Union of Pure and Applied Chemistry (IUPAC), a biosensor is an analytical device or unit for the detection of an analyte that integrates or associates a biological component (BRE) with a physico-chemical detector component (transducer) [2]. As shown in Fig. 1.1, the biosensor comprises of:

1. Bio-recognition elements (BREs) can be isolated from a living system or synthesized in a laboratory. Up to date, enzymes, molecular imprints, lectins, receptors, antibodies and nucleic acids were used as BREs which can specifically interact with the target analytes of interest.

2. Transducer translates the recognition events, e.g. analyte capture or enzymatic catalysis, into physical or chemical signals by means of electrical, electrochemical, optical, thermal, acoustic, piezoelectric components. They are designed to react to the presence of analyte sensitively, rapidly and quantitatively.

Design of interface between BREs and tranducer is essential for a stable, sensitive and accurate biosensor [3]. Biointerface science is defined as the study and control of biomolecular interactions with surfaces and has become a new catalog in a interdisciplinary research area [4]. The biointerfaces are typically highly hydrated in order to retain the activities of biomolecules. A good candidate of biointerface architechure has to accomondate BREs, maintain their bio-activity, be resistant against non-specific adsorption, and allow easy implementation [5]. Biointerfaces can be composed of bio-materials, synthesized polymers, or
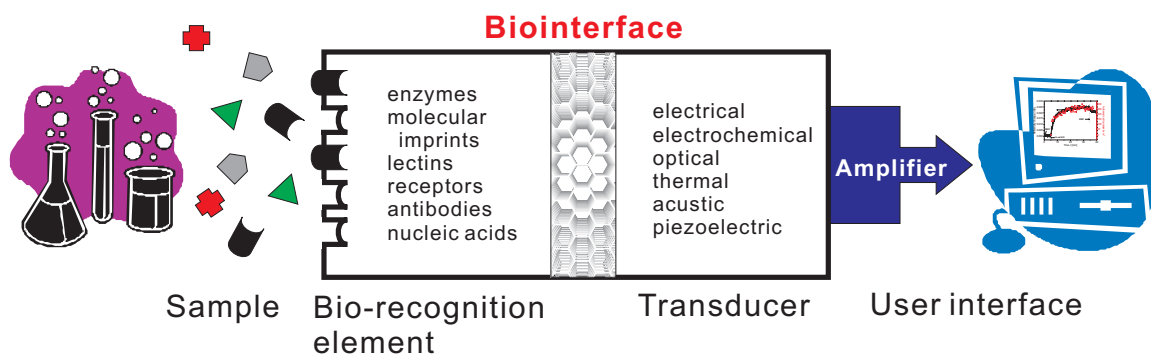
Figure 1.1: Configuration of a biosensor comprising of biorecognition, interface, and transduction elements.

inorganic materials and decorated with BREs via a wide range of chemical and physcial approaches. One challenge for the new generation of biointerfaces in applications of biosensing is to bring together the recent advances in material science and molecular biology in order to pursue ultra-sensitive detection in-field. In addition, a careful characterization for biointerfaces can be critical to meet the detection requirement and optimization.

Recently, biosensors with optical transducers have attracted a great deal of attention due to their potential for rapid and highly sensitive detection, easy integration and possible miniaturization [6]. Many types of optical sensors were pursued based on different principles for the specific applications [7]. Over the last two decades, those based on surface plasmon resonance (SPR) are rapidly gaining popularity as they allow for sensitive, label-free and real-time detection of molecular binding events [8, 9, 10, 11]. Since the invention of SPR biosensors in 1980's [12], we witnessed steady progress in their instrumentation as well as applications. SPR biosensors become an established technology for the interaction analysis of macromolecules in pharmaceutical and life sciences research [13] and their applications for rapid detection of chemical and biological compounds are continuously been pursued [14].

1.2 The state-of-art biosensors based on spectroscopy of surface plasmons

The SPR-based measurement of refractive index changes induced by the molecular binding events was proved to allow for sensitive and label-free detection of a wide range of analytes including proteins [15], nucleic acids [16] and carbohydrates [17]. In the early 1990s, an

SPR biosensor was successfully commercialized by Pharmacia Biacore and currently this technology is in the GE Healthcare portfolio. An other commercial SPR biosensor was developed later in a portable format by Texas Instruments, named Spreeta. This miniature SPR biosensor was integrated with plastic prism molded onto a microelectronic platform, infrared LED and a linear diode array detector [18]. This SPR system exhibited a refractive index resolution of 5×10^{-6} RIU [19].

Nowadays, numerous other SPR sensors based on spectroscopy of surface plasmons are commercially available. They include Multiskop system from Optrel (Kleinmachnow, Germany), SP 7000 platforms from Reichert Analytical Instrument (Depew, NY), Plasmonic from Hofmann Sensorsysteme (Wallenfels, Germany), Autolab Esprit and Springle SPR system from Eco Chemie (Ultrecht, The Netherlands), SPR-20 from DKK-TOA Corp. (Tokyo, Japan), Biosuplar 6 from Analytical μ-Systems (Sinzing, Germany), and Sensia β-SPR Research Platform (Madrid, Spain).

SPR biosensor technology has been pushed foward through improving the light source, photodetector, optics, microfluidics, surface chemistry and data analysis [20]. For instance, Homola's group integrated a special multilayer structure for supporting long-range surface plasmons into an SPR biosensor and demonstrated its resolution as low as 3×10^{-8} RIU [21]. However, the analysis of samples with extremely low analyte concentration or the detection of small molecules which do not produce sufficient refractive index changes remains a challenge for SPR biosensors. Therefore, SPR biosensors were combined with fluorescence spectroscopy in a method referred to as surface plasmon-enhanced fluorescence spectroscopy (SPFS) [22]. In this method, the surface plasmon-enhanced intensity of electromagnetic field allows for highly efficient excitation of captured fluorophore-labeled molecules which is directly translated to an increased fluorescence signal. By using SPFS, only fluorophores adhered to sensor surface are excited by the evanescent field of surface plasmons while those contained in the whole sample are not. In SPFS biosensors, a spacer between fluorophores and metal surface need to be used in order to avoid fluorescence quenching through Förster energy transfer. In order to suppress the fluorescence quenching and to increase the binding capacity within the evanescent field of surface plasmons, Yu et al. used a thin dextran brush with the thickness of about 100 nm as a three-dimensional binding matrix [23]. They showed that the SPFS readout of molecular binding events in such matrix allowed for the ultra-sensitive detection of chromophore-labeled molecules at concentrations as low as 0.5 fM.

1.3 Aim and outline of the study

The aim of this dissertation is to develop new schemes for surface plasmon resonance (SPR) and surface plasmon-enhanced fluorescence (SPFS) biosensors that allow rapid detection of molecular and biological analytes with advanced sensitivity which meets specific needs in important areas including food control and medical diagnostics. This goal is pursued through the employment of long range surface plasmon (LRSP) optics and responsive poly(N-isoproprylacrylamide)-based (pNIPAAm) hydrogel films. Long range surface plasmons are modes that can propagate with lower losses and exhibit more extended profile of electromagnetic field than regular surface plasmons. Hydrogels are cross-linked polymer networks that can be modified with bio-recognition elements in order to capture target analyte from a sample on the sensor surface with high efficiency. The thesis is structured to 6 chapters and chapters 3 - 7 describe the main results.

Chapter 3 presents the optimization of a layer structure for the excitation of LRSP modes on the sensor surface by using attenuated total reflection method with Kretschmann configuration. The used layer structure consists of a thin fluoropolymer buffer layer coated with a thin gold film. Surface modification of fluoropolymer is investigated in order to improve the adhesion strength and decrease the roughness of the gold film supporting LRSP modes.

The implementation of a carboxylated poly(N-isoproprylacrylamide) (NIPPAm)-based hydrogel to large binding capacity matrix is described in chapter 4. This material exhibits flexible, highly open 3D structure that can accommodate orders of magnitude larger amounts of catcher molecules compared to regular 2D architectures. Its responsive properties can be exploited for compacting of captured analyte on the sensor surface as discussed in chapter 4.1. Experimental and theoretical study that takes into account thickness of a hydrogel binding matrix, diffusion of target analyte, concentration of catcher molecules, binding rate constants, and profile of probing electromagnetic field was carried in order to maximize the sensor signal of SPR and SPFS biosensor as discussed in chapter 4.2. Refractometric and fluorescence spectroscopy-based biosensors that take advantage of the probing the sensor surface by hydrogel-guided waves are described in chapters 4.3 and 4.4, respectively.

Long range surface plasmon-enhanced fluorescence spectroscopy for detection of bacterial pathogens is investigated in chapter 5. The effect of profile of electromagnetic field that probes the capture of bacterial analyte on the sensor surface, sample flow rate affecting the diffusion rate of analyte to the surface and shear force were studied. The optimized LRSP-FS biosensor is applied for detection of *E. Coli* O157:H7.

1.4 Surface plasmon resonance

1.4.1 Electromagnetic theory of surface plasmons

In this section, an electromagnetic theory of surface plasmons propagating at an interface between a dielectric and a metal is presented by using the framework of the electromagnetic theory of optical waveguides [24, 25, 26]. In general, propagation of electromagnetic field is described by Maxwell's equations:

$$\nabla \times \vec{E}(\vec{r},t) + \mu \frac{\partial \vec{H}(\vec{r},t)}{\partial t} = 0, \tag{1.1}$$

$$\nabla \cdot (\mu \vec{H}(\vec{r},t)) = 0, \tag{1.2}$$

$$\nabla \times \vec{H}(\vec{r},t) - \varepsilon_0 \varepsilon(\vec{r}) \frac{\partial \vec{E}(\vec{r},t)}{\partial t} = 0, \tag{1.3}$$

$$\nabla \cdot (\varepsilon_0 \varepsilon(\vec{r}) \vec{E}(\vec{r},t)) = 0, \tag{1.4}$$

where $\vec{E}$ and $\vec{H}$ are the electric and magnetic field vectors, respectively, μ is magnetic permeability, ε is relative permittivity (dielectric constant) of the medium, ε_0 is the free-space permittivity and $\vec{r}$ is a spatial vector. For non-magnetic materials, the magnetic permeability μ is equal to the free-space permeability μ_0. We assume linear isotropic media and thus the Maxwell's equations (Eqs. 1.1-1.4) can be transformed to the following vector wave equations:

$$\Delta \vec{E}(\vec{r},t) - \varepsilon_0 \varepsilon(\vec{r}) \mu_0 \frac{\partial^2 \vec{E}(\vec{r},t)}{\partial t^2} = \nabla \left(\vec{E}(\vec{r},t) \right) \cdot \nabla \ln \varepsilon_0 \varepsilon(\vec{r})), \tag{1.5}$$

$$\Delta \vec{H}(\vec{r},t) - \varepsilon_0 \varepsilon(\vec{r}) \mu_0 \frac{\partial^2 \vec{H}(\vec{r},t)}{\partial t^2} = (\nabla \times \vec{H}) \times (\nabla \ln \varepsilon_0 \varepsilon(\vec{r})). \tag{1.6}$$

The Eq. 1.5 and 1.6 are further solved by using Cartesian coordinate system $\vec{r}(x\vec{x}_0, y\vec{y}_0, z\vec{z}_0)$, where $\vec{x}_0$, $\vec{y}_0$ and $\vec{z}_0$ are the vectors.

Let us consider an optical waveguide consisting of three homogeneous media (Fig. 1.2) with a permittivity profile:

$$\varepsilon(x) = \varepsilon_1 = n_1^2, x < -d; \text{ for the substrate}, \tag{1.7}$$

$$\varepsilon(x) = \varepsilon_2 = n_2^2, -d \leq x \leq d; \text{ for the waveguiding layer}, \tag{1.8}$$

$$\varepsilon(x) = \varepsilon_3 = n_3^2, x > d; \text{ for the superstrate}, \tag{1.9}$$

where d is the waveguide layer half-width and ε_i and n_i ($i = 1, 2, 3$) are generally complex permittivities and refractive indices. Due to translational invariance of the waveguide and the time dependence of the field vectors in the form of $\exp(-i\omega t)$, where ω is the angular frequency and $i = \sqrt{-1}$, the field components can be expressed as:

$$\vec{E} = \vec{e}(x)\exp(i(\beta z - \omega t)), \tag{1.10}$$

$$\vec{H} = \vec{h}(x)\exp(i(\beta z - \omega t)), \tag{1.11}$$

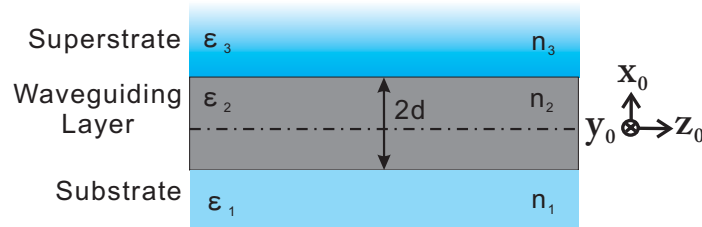where β is the propagation constant.

Figure 1.2: Section of a planar waveguide with a step refractive index profile.

Two linearly independent sets of modes, which are the transverse magnetic (TM, $\vec{H} = (0, \vec{h}_y, 0)$ and $\vec{E} = (\vec{e}_x, 0, \vec{e}_z)$) and transverse electric (TE $\vec{E} = (0, \vec{e}_y, 0)$ and $\vec{H} = (\vec{h}_x, 0, \vec{h}_z)$), can be formed from the following equations:

$$\frac{\partial^2 \vec{e}_y(x)}{\partial x^2} + (\omega^2 \varepsilon_0 \varepsilon \mu_0 - \beta^2)\vec{e}_y(x); \text{ for the TE modes,} \tag{1.12}$$

$$\frac{\partial^2 \vec{h}_y(x)}{\partial x^2} + (\omega^2 \varepsilon_0 \varepsilon \mu_0 - \beta^2)\vec{h}_y(x); \text{ for the TM modes.} \tag{1.13}$$

In each medium the solution of Eq. 1.12 and 1.13 can be described as a linear combination of functions: $\exp(i\kappa_i x)$ and $\exp(-i\kappa_i x)$, where $\kappa_i^2 = \omega^2 \varepsilon_0 \varepsilon_i \mu_0 - \beta^2 (i = 1, 2, 3)$:

$$\vec{e}_y(x) = a_i^+ \exp(i\kappa_i x) + a_i^- \exp(-i\kappa_i x), \tag{1.14}$$

$$\vec{h}_x(x) = \frac{\beta}{\mu_0 \omega}\left[a_i^+ \exp(i\kappa_i x) + a_i^- \exp(-i\kappa_i x)\right], \tag{1.15}$$

$$\vec{h}_z(x) = -\frac{\kappa_i}{\mu_0 \omega}\left[a_i^+ \exp(i\kappa_i x) - a_i^- \exp(-i\kappa_i x)\right] \tag{1.16}$$

for TE modes, and

$$\vec{h}_y(x) = b_i^+ \exp(i\kappa_i x) + b_i^- \exp(-i\kappa_i x), \tag{1.17}$$

$$\vec{e}_x(x) = -\frac{\beta}{\varepsilon_0 \varepsilon_i \omega} \left[b_i^+ \exp(i\kappa_i x) + b_i^- \exp(-i\kappa_i x) \right], \tag{1.18}$$

$$\vec{e}_z(x) = \frac{\kappa_i}{\varepsilon_0 \varepsilon_i \omega} \left[b_i^+ \exp(i\kappa_i x) - b_i^- \exp(-i\kappa_i x) \right] \tag{1.19}$$

for TM modes.

In the superstrate and substrate media, the fields of guided waves exponentially decay with a distance away from the waveguide. Therefore, the amplitudes of a_1^+ and a_1^-, and a_3^+ and a_3^- are equal to zero for TE and TM modes, respectively. The requirement of continuous field components that are parallel to the interfaces leads to the eigenvalue equation:

$$\tan(\kappa d) = \frac{\gamma_1/\kappa + \gamma_3/\kappa}{1 - (\gamma_1/\kappa)(\gamma_3/\kappa)} \tag{1.20}$$

for the TE modes, and

$$\tan(\kappa d) = \frac{\gamma_1 \varepsilon_2/\kappa\varepsilon_1 + \gamma_3 \varepsilon_2/\kappa\varepsilon_3}{1 - (\gamma_1 \varepsilon_2/\kappa\varepsilon_1)(\gamma_3 \varepsilon_2/\kappa\varepsilon_3)} \tag{1.21}$$

for the TM modes, where $\gamma_i^2 = \beta^2 - \omega^2 \mu_0 \varepsilon_0 \varepsilon_i$ (i is 1 or 3).

Considering the surface plasmons at an interface between metal and dielectric, we re-define the layer structures as: (a) d is equal to zero in Fig. 1.2; (b) the layer structure consists of a semi-infinite metal with a complex permittivity $n_1^2 = \varepsilon_1 = \varepsilon_1' + i\varepsilon_1''$, and a semi-infinite dielectric with permittivity $n_3^2 = \varepsilon_3 = \varepsilon_3'$ (Fig. 1.3a). There can be shown that there exist any one solution of Eq. 1.21 for the guided TM mode:

$$\frac{\gamma_1}{\varepsilon_1} = -\frac{\gamma_3}{\varepsilon_3}. \tag{1.22}$$

The Eq. 1.22 can further reduced to the well known dispersion relation of SPs as:

$$\beta_{SP} = k_0 \sqrt{\frac{\varepsilon_3 \varepsilon_1}{\varepsilon_3 + \varepsilon_1}}, \tag{1.23}$$

where $k_0 = 2\pi/\lambda$ is the free-space wavenumber and λ is the free-space wavelength.

The electromagnetic field of SPs can be described by the following nonzero components: magnetic intensity parallel to the interface h_y, electric intensity parallel to the interface e_z and electric intensity perpendicular to the interface e_x. As seen in Fig. 1.3b, the SP field decays exponentially from the metal - dielectric interface with the penetration depths L_{pen}^1 and L_{pen}^3 into the metal and the dielectric, respectively. The penetration depth is defined as the distance perpendicular to the surface at which the field amplitude decreases by a factor of $1/e$ ($L_{pen}^j = Re\left\{\beta^2 - k^2 n_j^2\right\}^{-1/2}$ where j is 1 or 3 for the metal and dielectric, respectively). The energy of SP dissipates while it propagates along the metal surface due to
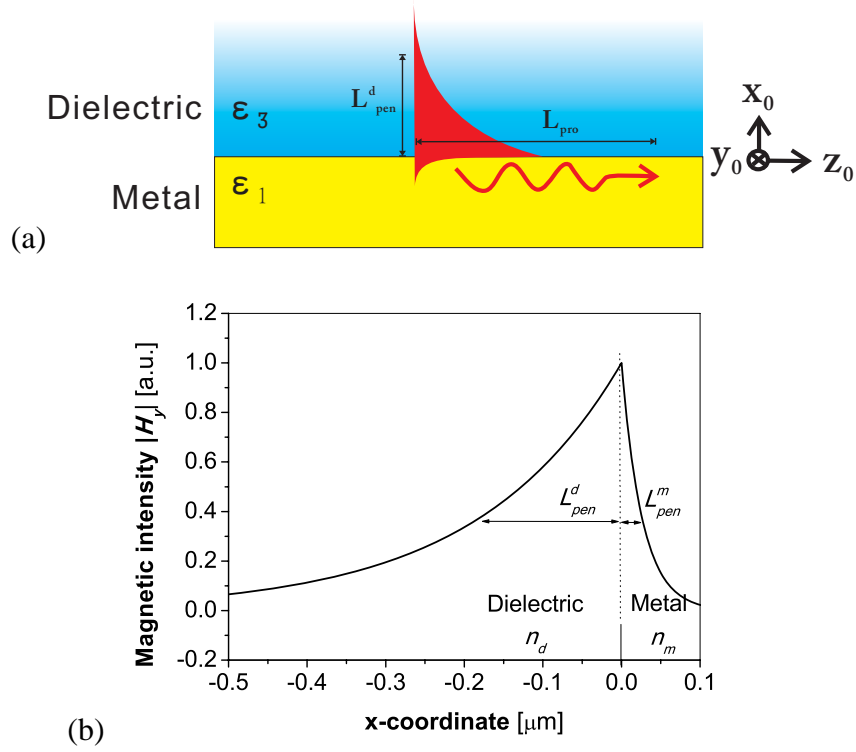
Figure 1.3: (a) A metal-dielectric layer structure supporting surface plasmon mode. (b) The profile of the magnetic intensity field H_y of the SP propagating along the interface of gold ($n_1 = 0.1 + 3.5$) and a dielectric ($n_3 = 1.33$) at a wavelength of $\lambda = 633$ nm.

the Ohmic losses within the metal film. This damping can be described by the propagation length $L_{pro} = 1/(2Im\{\beta\})$ as the distance along the metallic surface at which the intensity of the SP mode drops to $1/e$.

1.4.2 Long range surface plasmons

Considering another geometry of waveguide supporting surface plasmons, a thin metal film with refractive index of n_1 is sandwiched between two semi-infinite dielectric media with identical refractive indices of n_3 (Fig. 1.4). If thickness of metal film d_1 is comparable with the penetration depth of SPs in the metal, two SP waves on the opposite side of metal film penetrate through the film. Their interaction gives rise to new coupled SP modes with symmetrical and anti-symmetrical profile of fields. These modes are referred to as long range surface plasmon (LRSP) and short range surface plasmon (SRSP), respectively, shown in Fig. 1.4. These SP modes have been firstly theoretically investigated by Sarid [27]. He
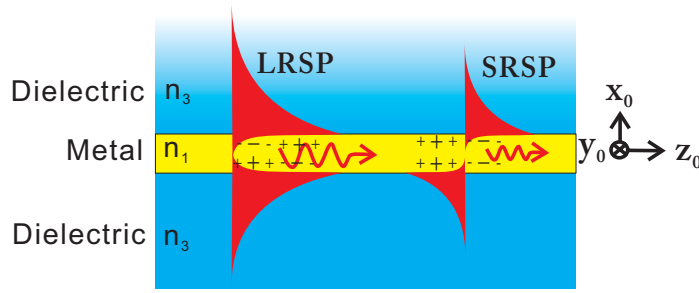
Figure 1.4: Symmetrical and anti-symmetrical SP modes propogating along a thin metal film embedded between dielectrics with identical refractive index

showed that two coupled SP waves are guided along the metallic film with propagation constant that can be obtained from a simplied Eq. 1.21 in the form:

$$\tan(\kappa d_1) = \frac{2\gamma n_1^2/\kappa n_3^2}{1 - (\gamma n_1^2/\kappa n_3)^2}, \tag{1.24}$$

where d_1 is the thickness of the metal film, $\kappa^2 = (k_0^2 n_1^2 - \beta^2)$ and $\gamma^2 = (\beta^2 - k_0^2 n_3^2)$. By solving the Eq. 1.24, one can see that LRSP exhibits smaller $Re\{\beta\}$ and a larger propagation length L_{pro} than those of SRSP [28, 21].

1.4.3 Excitation of surface plasmons by prism coupler

The most common approach to excite surface plasmons is by means of a prism coupler and the attenuated total reflection method (ATR) in the Kretschmann geometry (Fig. 1.5a). In this method, a thin metal film with a refractive index of n_1 is deposited on a glass prism and is in contact with a dielectric with a refractive index of n_3. The refractive index of the prism is higher than that of dielectric ($n_p > n_3$). A light beam is launched into the glass prism. The momentum of the photon in the z-direction k_{ph}^z can be expressed as:

$$k_{ph}^z = k_0 \cdot n_p \cdot \sin(\theta), \tag{1.25}$$

where θ is the angle of incidence.

Above the critical angle, $\theta_c = \arcsin(n_p/n_3)$, the light beam is totally internally reflected from the prism base. This wave penetrates into the metal layer via its evanescent tail (Fig. 1.5a). If the thickness of the metal layer is thin enough ($d_m \sim 50$ nm) the evanescent wave can couple with a surface plasmon at the outer metal/dielectric interface. This coupling is resonant and occur when the momentum of the light beam in the z-direction k_{ph}^z is matched
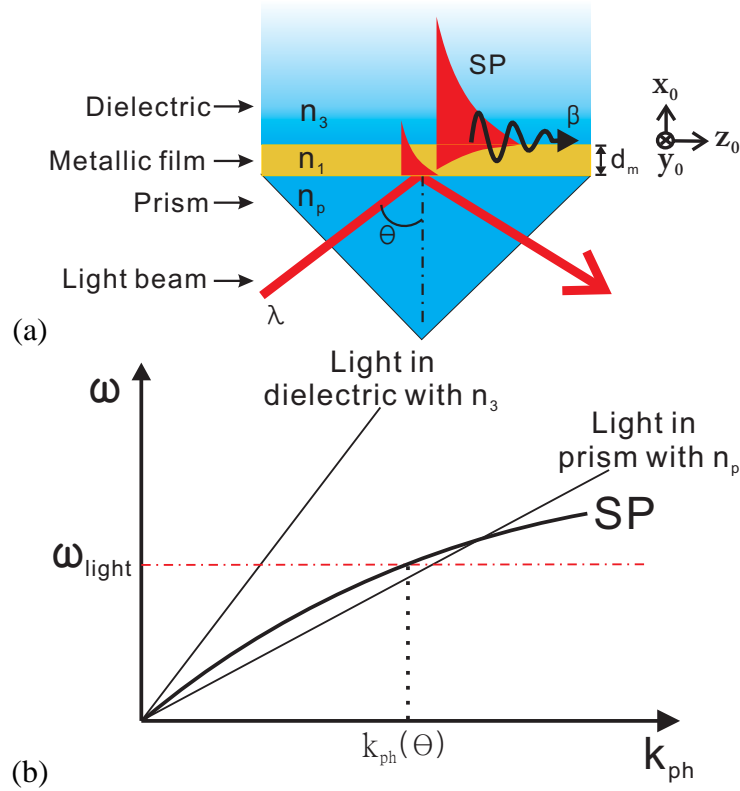
Figure 1.5: (a) Excitation of surface plasmons in the Kretschmann geometry of the attenuated total reflection (ATR) method. (b) The dispersion relation of a photon traveling as a plane wave in a dielectric.

to that of SP on the outer interface (Fig. 1.5b)as:

$$k_0 \cdot n_p \sin(\theta) = Re \left\{ \beta_{sp} \right\}. \tag{1.26}$$

The coupling of a light beam to the surface plasmon modes is manifested as a characteristic resonant dip in a angular reflectivity spectrum as seen in Fig. 1.6. At the resonant angle, the excitation of SP provides a strongly enhanced electromagnetic field intensity at the interface of metallic film and dielectric. For instance, on a layer structure of glass ($\varepsilon_p = 3.4036$) and Ag ($\varepsilon_{Ag} = -17 + 0.5i$, d = 50 nm) in water ($\varepsilon_d = 1.778$) at λ = 633 nm, the interfacial SP field intensity is enhanced by a factor of 80 with respect to the incident light beam (the enhancement factor is equal to the ratio of the electric field intensity $|E|^2$ of incident beam and SP).
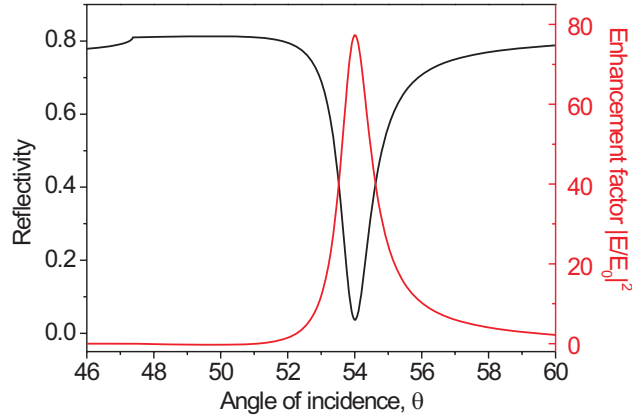
Figure 1.6: Reflectivity (black, left axis) and enhancement factor (red, right axis) of the interfacial optical intensity for a layer structure of glass ($\varepsilon_p = 3.4036$) and Ag ($\varepsilon_{Ag} = -17 + 0.5i$, d = 50 nm) in water ($\varepsilon_d = 1.778$). Reproduced from Ref. [29]

1.4.4 Surface plasmon resonance biosensors

In surface plasmon resonance (SPR), biosensors bio-recognition elements (BREs) are im-mobilized on a metallic sensor surface for specific capture of analyte molecules contained in a liquid sample, see Fig. 1.7a. As the binding of analyte molecules induces a change in the refractive index δn_f in the vicinity to the metallic surface, the propagation constant of SP is altered and thus the momentum of photon required to fulfill the phase matching condition. Therefore, molecular binding events can be detected by the measuring variations of the characteristics of a light beam which is resonantly coupled to surface plasmons e.g. as a shift in the SPR reflectivity dip shown in Fig. 1.7b.

For small changes, the resonance shift can be observed from variations of reflectivity δR at a fixed angle of incidence set closed to the resonance:

$$\delta R = \frac{dR}{d\theta}\delta\theta, \tag{1.27}$$

where $dR/d\theta$ is the slope of the SPR reflectivity curve.

We firstly consider the refractive index variations within the whole evanescent field of SP, which are referred to as bulk refractive index changes, δn_b:

$$\delta\theta_b = S_b\delta n_b, \tag{1.28}$$

where the factor S_b is denoted as the bulk refractive index sensitivity. The sensitivity S_b depends on the wavelength and on optical parameters of the involved materials [30]. For
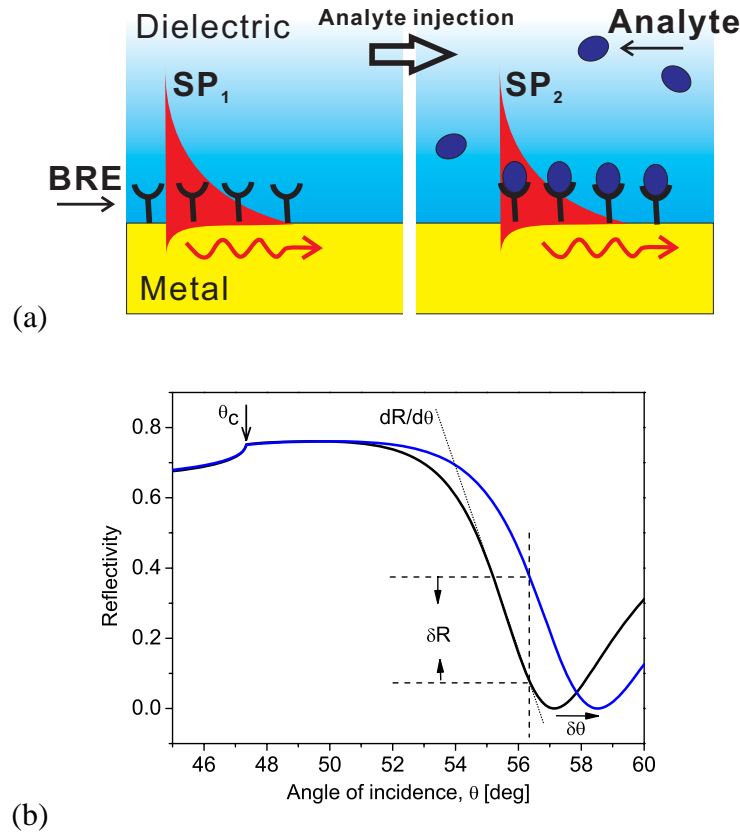
11

(a)

(b)

Figure 1.7: (a) Interaction of biorecognition elements with an analyte on a metallic sensor surface. (b) SPR angular reflectivity spetra measured prior and after the binding of analyte.

a layer with a refractive index n_f and the thickness d which is much lower than the SP penetration depth $d \ll L_{pen}^3$, a shift in the coupling angle of incidence $\delta\theta_s$ is proportional to a change in the optical thickness $\delta n_f d$:

$$\delta\theta_s = S_s \delta n_f d, \qquad (1.29)$$

where the factor S_s is denoted as surface refractive index sensitivity. The surface refractive index sensitivity can be shown to relate to bulk refractive index sensitivity as $S_s = 2S_b / L_{pen}^d$ from perturbation theory [30] or numerically from Fresnel reflectivity theory. From the magnitude of the binding-induced change $\delta\theta_s$, the surface concentration of captured molecules γ can be obtained as:

$$\gamma = \frac{\delta\theta_s}{S} \frac{\delta c}{\delta n_f}, \qquad (1.30)$$

where S is equal to the surface refractive index sensitivity S_s if the analyte binds directly to the surface (e.g. binding of medium size protein to a monolayer of receptors). For the binding which occur within the whole evanescent field of SP, the coefficient S is equal to $S_b d^{-1}$

(e.g. ligands immobilized within a three-dimensional binding matrix with the thickness d comparable or larger than L_{pen}^3). The coefficient $\delta c/\delta n_f$ expresses how the refractive index increases with the concentration of analyte molecules. For most proteins, the coefficient $\delta c/\delta n_f$ lies in a range 0.14-0.2 μL mg^{-1} [31].

1.4.5 Surface plasmon field-enhanced fluorescence spectroscopy

A fluorophore is a molecule that can adsorb a photon with a specific wavelength and re-emit it at another higher wavelength. As seen in the Jablonski diagram in Fig. 1.8, the fluorophore can be excited from its ground state S_0 to a higher singlet state S_1, followed by spontaneous relaxation. In a free space, the excited flourophore can return to the ground state S_0 through emitting another photon at a higher wavelenght (radiative decay channel) or without emitting a photon, e.g. due to collisional quenching (nonradiative decay channel). The fluorescence emission rate of P_{em} depends on the excitation rate P_{ex}, the radiative decay rate P_r, and the nonradiative decay rate P_{nr} as:

$$P_{em} \propto P_{ex}\frac{P_r}{P_r+P_{nr}}. \tag{1.31}$$

Let us note that the quantum yield defined as $Q = P_r/(P_r+P_{nr})$ is in the range of 0.5-0.9 and the lifetime $\tau = (P_r+P_{nr})^{-1}$ is between 1 and 10 ns for most used organic chromophores.
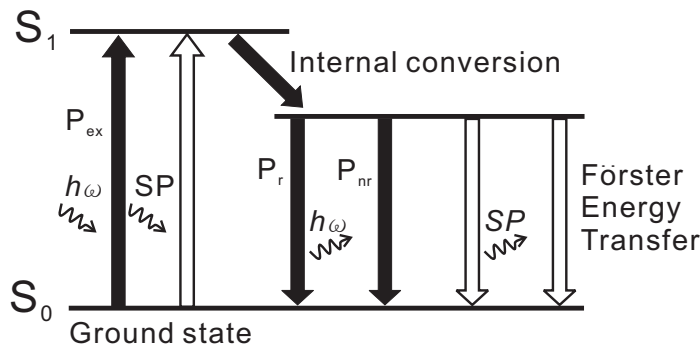

Figure 1.8: Jablonski diagram showing transitions taking place with a fluorophore in a free space (black arrows) and additional excitation of decay channels occuring in the vinicity of a metallic surface (black and white arrows).

From Eq. 1.31 follows that the fluorescence emission rate P_{em} increases with the excitation rate P_{ex}. If the fluorophore is placed within the SP field with wavelength matching the adsorption band, strong emitted fluorescence light is detected due to the enhanced EM field intensity [32]. If a fluorophore is in a close proximity to a metallic surface , besides the SP excitation channel, two additional decay channels are opened (Fig. 1.8). Firstly, when the

separation distance of the fluorophore from the surface is less than $\sim$ 15 nm the Förster energy transfer between the fluorophore and electrons in the metal quenches the fluorescence signal [33]. Secondly, a strong coupling of fluorescence light to SP occurs at distances up to several hundreds of nanometers from the metallic surface [34]. This fluorescence light emitted via SPs can be subsequently out-coupled via a glass prism, which provides a highly directional fluorescence emission pattern [35].
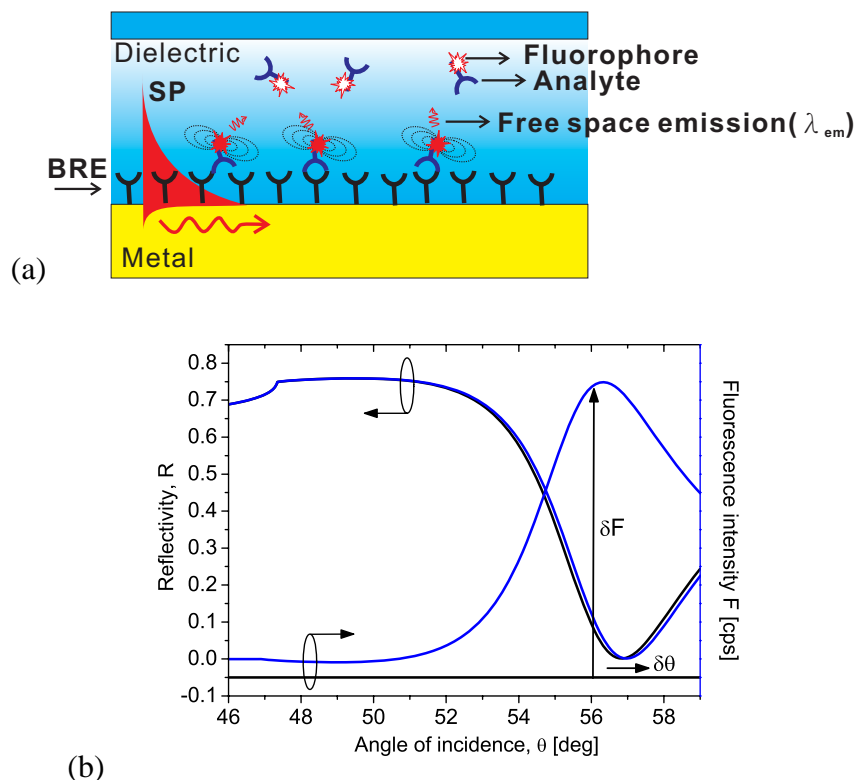

Figure 1.9: (a) The excitation of fluorophores labeled on captured analytes within the SP field. (b) Angular reflectivity and fluorescence spectra before (black) and after (blue) the binding of fluorophore-labeled molecules on surface.

The feature of SP-mediated fluorescence excitation has been employed and integrated into SPR device in order to develop an ultra sensitive biosensor, which is referred to as surface plasmon field-enhanced fluorescence spectroscopy (SPFS). In biosensing applications, the binding of molecules labeled with fluorophores of which absorption band matches the wavelength of an excitation laser beam is depicted in Fig. 1.9a. These molecules are captured on surface and the enhanced intensity of the optical field that is accompanied with the coupling to surface plasmons provides an efficient excitation of fluorophores manifested as an increase in the fluorescence intensity, as seen in Fig. 1.9b. The strength of fluores-

cence signal is several orders of magnitude higher than that of measurements based on the shift of angle or reflectivity in SPR biosensors [22].

1.5 Surface architectures for molecular immobilization

In SPR biosensors, stable linkage between bio-recognition elements (BREs) and the sensor surface needs to be established. Moreover, the immobilized biomolecules have to retain their biological activity and the surface architecture should exhibit non-fouling properties minimizing the non-specific interactions with analyzed samples. Within this section, most common immobilization methods, relying on self-assembled monolayers and hydrogel binding matrix and bio-affinity binding platforms are introduced.

1.5.1 Self-assembled monolayer

Self-assembled monolayers (SAMs) are highly organized layers of amphiphilic molecules and provide a convenient, flexible, and simple platforms to modify interfacial properties of metals, metal oxides and semiconductors [36]. SAMs are organic assemblies prepared by the adsorption of molecular constituents from solution or the gas phase onto the surface of solids. In SPR biosensors, the mixed SAMs provide a practical experimental system in which the surface can be modified by biomolecules of interest and repel the non-specific adsorption. The anchor group of the SAM molecular constituents has a chemical functionality with a specific affinity to a substrate. The thiol molecules are widely applied as anchor groups to establish stable metal-thiol bonds for attach of SAM materials. In the SPR sensor applications, the most extensively studied class of SAMs is derived from the adsorption of alkanethiols on gold. This alkanethiols form a tightly packed SAMs due to the van der Waals interactions through reducing its own free energy as seen in Fig. 1.10. Non-fouling property of the sensing surface is a critical factor affecting the performance of the biosensor in a complex media, such as blood serum or plasma. Up to date, good non-fouling surfaces were prepared when the following conditions were fulfilled: (a) zero net charge, (b) hydrophilic nature, (c) presence of groups that are hydrogen acceptors instead of hydrogen bound donors [37, 38, 39]. The alkanethiols terminated with tri- or hexa-(ethylene glycol) groups are the most popular materials used to resist the nonspecific adsorption of other biomolecules. The terminal ethylene glycol end-group adopts either a helical conformation aligned perpendicular to the surface or an amorphous conformation [40, 41]. The other ma-

terials of interest for non-fouling are zwitterionic materials comprising of poly(sulfobetaine) and poly(carboxybetaine) polymers [42], carboxymethyl cellulose [43] and poly(2-aminoethyl methacrylate)(PAEMA) comprising of polyeletrolytes [44]. For functionalization of the surface, the ligand groups separated from the background by linker/spacer are presented on the most top of the surface. The lignads can be chemically and biologically modified with biomolecules of interest in a structurally well-defined manner and its surface density can be controlled through adjusting the ratio of two thiol constituents. Thus, such surface modification strategy through bifunctional SAMs is able to resist non-specific binding, and to anchor specific biomolecules that remain biological activities in their native conformations [45]. This planar format of the bifunctional SAMs, therefore, makes it convenient to determine the specific bio-affinity reaction for the molecular detection by using SPR biosensors.
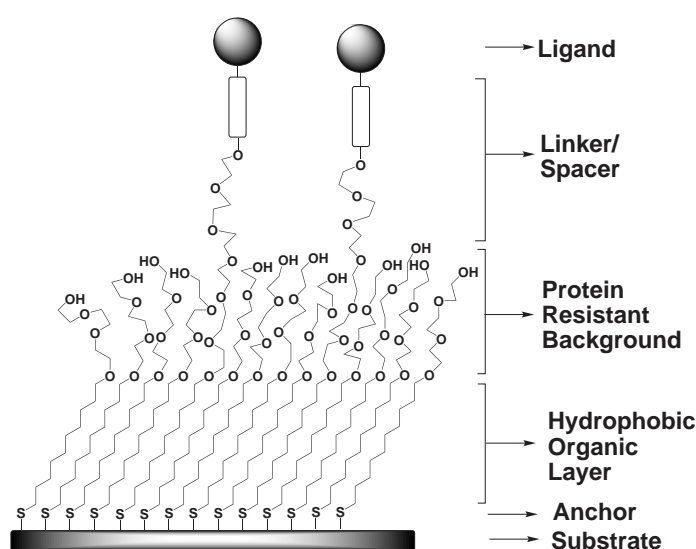

Figure 1.10: Mixed self-assembled monolayer comprising of tri-ethylene glycol thiols and functional thiols.

1.5.2 Hydrogel binding matrix

Hydrogels are insoluble, cross-linked water-swollen polymer networks of hydrophilic homopolymers or copolymers. Owing to their highly open structure and large inner surface, hydrogels can accommodate large amounts of molecules with specific functions. Hydrogels become irreplaceable materials in numerous important fields including pharmaceutical applications (e.g. drug delivery or tissue engineering) [46, 47] and biosensor technologies for detection of chemical or biological analytes [48, 49, 50].

In biosensor applications, hydrogel materials are employed at an interface between an analyzed aqueous sample and a transducer. Typically, the hydrogel interface is modified with bio-recognition elements (BREs) such as antibodies, enzymes or with biomimetic molecular imprinted moieties in order to specifically recognize target analytes. Compared to the other types of biointerfaces (e.g. based on SAMs), hydrogels can accommodate orders of magnitude larger amounts of recognition elements [51], provide more natural microenvironment for remaining the bio-activity of biomolecules [48] and offer routes for implementing of additional functionalities (e.g. separation of target analyte from other molecules in a sample [52]). In addition, the class of "smart" gels that response to external stimuli become of increasing interest in biosensor research. For instance, a miniature holographic hydrogel elements based on these materials were integrated in a contact lens for the real-time analysis of glucose in a tear fluid [53]. Various organic polymers were synthesized and applied for hydrogel biointerface architectures as reported in literature. These include chitosan [54], dextran [51], poly(vinylalcohol) (PVA) [55], 2-hydroxyethyl methacrylate (HEMA) [56, 57], poly(2-vinylpyridine) (P2VP) [58], poly(ethylene glycol) (PEG) [59] and poly(N-isopropylacrylamide) (NIPAAm) [60, 51].

1.5.3 Bioaffinity immobilization

The mostly used bioaffinity immobilization is based on avidin-biotin which strong noncovalently interact ($K_d = 10^{15}$ M^{-1}). This bond is stable enough in harsh conditions and this specific interaction permits well-oriented biomolecule immobilization [61]. Avidin is a tetrameric glycoprotein soluble in aqueous solutions and stable over a wide range of pH values and temperatures. It can bind up to four molecules of biotins. Streptavidin is a closely related tetrameric protein with similar affinity to biotin. Biotin is a natural vitamin found in all living cells. Since biotin is a small molecule, its conjugation to biomolecules does not affect their conformation, size, or functionality.

Other bioaffinity immobilization methods are suitable for antibodies based on specific interaction of protein A/protein G with the Fc region of IgG molecules. The advantage of this method is that the binding sites of antibody, located on the Fab variable region, remain well accessible [62]. However, the disadvantage of the protein A-mediated immobilization is that only certain classes of antibodies are able to bind protein A. The protein G shows a broad binding activity for immunoglobulines of different species and subclasses.

1.6 Molecular interactions

1.6.1 Langmuir adsorption kinetics on surface

SPR and SPFS-based sensor can be employed for the observation of the molecular binding kinetics on a surface [63, 64]. A simple molecular adsorption model is introduced in this section. The bio-recognition elements B are immobilized on the sensor surface to capture the A molecules from a liquid sample as seen in Fig. 1.11a. Let us assume that the dynamic equilibrium of the reaction between molecules A and B is expressed as:

$$A + B \overset{k_d, k_a}{\longleftrightarrow} AB, \tag{1.32}$$

where k_a and k_d are the association and dissociation rate constants, respectively. In the model, let us assume that the interaction of molecules, A and B, fulfills following conditions of 1:1 Langmuir isotherm: (a) all capture molecules B are equivalent and can only accommodate one analyte molecule A; (b) the ability of analyte to bind to the given capture molecule is independent of the occupation of neighboring sites. In some cases, the reactions are controlled by the mass transport of analytes in the flow-cell, and thus the analyted results present the effective association k_{on} and dissociation k_{off} rate constants which involve diffusion rate k_m. The kinetics of formation of the complex AB can be described by the following pseudo first order differential equation:

$$\frac{d\gamma}{dt} = k_{on}\alpha(\beta - \gamma) - k_{off}\gamma, \tag{1.33}$$

where γ is the concentration of the complex AB on the surface, α is the concentration of molecule A in the solution, β is the concentration of molecule B on the sensor surface and t is time. In this equation, the kinetics of the rate of the formation of complex AB is expressed by the term $k_{on}\alpha(\beta - \gamma)$ and the dissociation of the complex AB is determined by the term $k_{off}\gamma$. k_{on} and k_{off} are defined as:

$$k_{on} = \frac{k_a}{1 + k_a\left[\beta - \gamma(t)\right]/k_m}, \tag{1.34}$$

$$k_{off} = \frac{k_d}{1 + k_a\left[\beta - \gamma(t)\right]/k_m}. \tag{1.35}$$

The k_m can be obtained by using a two compartment model [65] as:

$$k_m = \xi\left(\frac{v_{max}D^2}{hL}\right), \tag{1.36}$$

where D is the diffusion constant, v_{max} is the flow velocity in the middle of the flow-cell, h and L are the height and the length of the flow-cell, respectively, and ξ is a constant ($\xi = 1.378$ was derived by Edwards et al. [66] and 0.98 was published by Sjolander et al. [65]). For spherical molecules with the radius a, a solution with the viscosity η, the absolute temperature T and Boltzmann constant k_B, the diffusion constant D can be expressed from Stokes formula as:

$$D \approx \frac{k_B T}{6\pi a \eta}. \tag{1.37}$$

In order to quantify the effect of the mass transfer to the reaction kinetics, a Damköhler number is used:

$$Da = k_a \beta \left(\frac{hL}{v_{max}D^2} \right)^{1/3}. \tag{1.38}$$

For $Da >> 1$, the mass transfer of molecule A to the surface is much slower than the as-
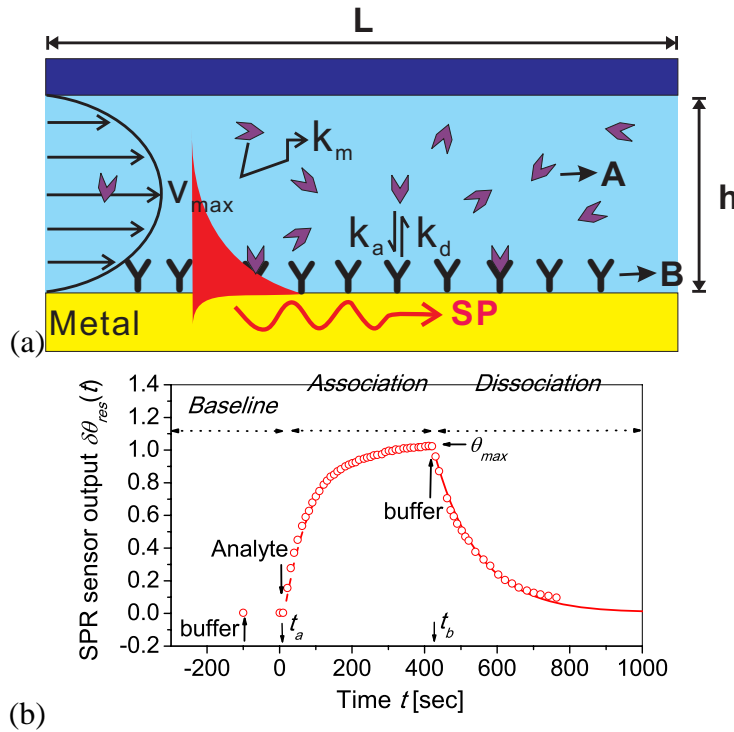
Figure 1.11: (a) Scheme of typical affinity recognition events occuring on the surface. (b) The kinetics of molecular binding in SPR.

sociation rate, i.e. $k_m << k_a\beta$, and the reaction is referred to as mass transport-controlled. In this regime, the effective association and dissociation constants can be expressed as $k_{on} \approx k_m\beta^{-1}$ and $k_{off} \approx k_m k_d (k_a\beta)^{-1}$, respectively. In order to analyze the molecular interaction, the effect of the mass transport can be minimized through decreasing the surface

coverage of molecule β, or increasing the flow rate v_{max} in order to minimize D_a. If $Da << 1$, the mass transport is much faster than the reaction association rate, i.e. $k_m >> k_a\beta$ and the reaction is referred to as interaction controlled reaction and the effective binding constants approaches the association and dissociation rate constants $k_{on} \approx k_a$ and $k_{off} \approx k_d$.

   In the interaction-controlled reaction, the association k_a and dissociation k_d constants can be obtained by fitting the kinetics response from SPR measurements for the association and dissociation phases. Fig. 1.11b shows that the baseline is established in buffer solution before analyte injection. A sample with molecule A is flowed through a the flow-cell at the time t_a and at the time t_b the analyte sample is removed by flushing with buffer. On the kinetics of the dissociation phase, the exponentially decaying sensor output can be described by the following solution of Eqs. 1.33-1.35:

$$\delta\theta_{res}(t) = S\frac{\partial n_f}{\partial c}M_w\gamma(t_b)\exp\left(-k_d(t-t_b)\right) = \delta\theta_{res}(t_b)\exp\left(-k_d(t-t_b)\right), \qquad (1.39)$$

where the term $S(\delta n_f/\delta c)$ is the sensitivity factor, M_w is the molecular weight of molecule A, $\gamma(t_b)$ is the molar concentration of captured molecule A at the time t_b and δ is $\theta_{res}(t_b)$ is the sensor output at the time t_b. For the association phase, the time evolution of the sensor output is:

$$\delta\theta_{res}(t) = S\frac{\partial n_f}{\partial c}M_w\frac{k_a\alpha\beta}{k_a\alpha-k_d}\left(1-\exp(-k_a\alpha+k_d)(t-t_a)\right) = \delta\theta_{res}^{eq}\left(1-\exp(-k_a\alpha+k_d)(t-t_a)\right),$$
$$(1.40)$$

where the constant $\delta\theta_{res}^{eq}$ is sensor output for the equilibrium of the reaction at a concentration of $\gamma_{eq} = k_a\alpha\beta(k_a\alpha-k_d)$ for which the association rate $k_a\alpha(\beta-\gamma)$ and dissociation rate $k_d\gamma$ are equal. Thus, in order to obtain k_a and k_d from the time revolution of the measured sensor responses $\delta\theta_{res}(t)$, firstly, the kinetics curve in the dissociation phase is fitted by using the Eq. 1.39 for k_d. The obtained k_d is put to Eq. 1.40 and the sensor output in the association phase is fitted to Eq. 1.40 to get the association constant k_a.

2 Methods

2.1 Materials

Cytop fluoropolymer (CTL-809M, 9 weight % in the solvent of CT-solv 180) was obtained from Asahi Glass (Tokyo, Japan) and 99.99%-Au grains were from Edelmetall (Neuss, Germany). 99.5% absolute ethanol, phosphate buffered saline (PBS), 95% triethylene glycol mono-11-mercaptoundecyl ether (PEG-thiol), Cy5-conjugated streptavidin (SA) and ethanolamine hydrochloride were purchased from Sigma-Aldrich (St. Louis, MO). Biotin-terminated triethylene glycol mono-11-mercaptoundecyl ether (Biotin−thiol) was from Pro-Chimia Surface (Sopot, Poland). Dithiolalkanearomatic PEG6-COOH (COOH-dithiol) and dithiolalkanearomatic PEG3-OH (PEG-dithiol) were purchased from SensoPath (Bozeman, MT). N-Isopropyl-acrylamide (NIPAAm), Methacrylic acid (MAA), 2,2'-Azobis (isobutyroni-trile) (AIBN), sodium methacrylate (SMA) and methanol were obtained from Sigma-Aldrich (St. Louis, MO). 1-Ethyl-3-[3-dimethylaminopropyl] carbodiimide hydrochloride (EDC) and N-hydroxy-succinimide (NHS) were obtained from Thermo (Rockford, IL). The Hellmanex II, LASFN9 glass substrates (76 mm×25 mm×1.5 mm) were acquired from Hellma Optik (Jena, Germany). BK7 glass substrates (76 mm×26 mm×1 mm) were obtained from VWR (Wien, Austria). The para-tetrafluorophenol-sulfonate (TFPS) and S-3- (benzoylphenoxy) propyl ethanthioate (benzo-phenone-thiol) was systhesized in house [67].

2.2 Preparation of layer structure supporting SPs and LRSPs

Firstly, glass substrates were cleaned by sonicating in 2% Hellmanex II detergent for 20 min followed by extensive rinsing in H_2O and ethanol and drying under a stream of nitrogen. Cytop fluoropolymer was spin-coated on a BK7 glass substrate, dried at room temperature for 1 hour and incubated at a temperature of $T = 160°$C for 1 hour. The thickness of Cy-

top layers was controlled by adjusting the rotation speed. Thin gold films were deposited by means of thermal evaporation (Edwards FL400, Boc Edwards, East Sussex, UK) with the evaporation rate of ~1.5 Å/s in a vacuum better than $\sim 2.6 \times 10^{-6}$ mbar or by using magnetron sputtering (UNIVEX 450C from Leybold Systems, Germany). The prepared gold substrates were transfered immediately into a thiol solution.

2.3 Surface modification

2.3.1 Thiol SAM

The chemical structures of all used thiol molecules are presented in Fig. 2.1. Two thiols with functional groups for biomolecule conjugation were used in this dissertation, which are biotinylated thiol (biotin-thiol) and carboxylated thiol (COOH-thiol). The thiols with PEG moieties were employed to form "inert" background that is resistant against the non-specific adsorption. A mixture of monothiolalkane(C11) PEG3-Biotin (Biotin-thiol) and monothiolalkane(C11) PEG3-OH (PEG-thiol) at a molar ratio of 9:1 dissolved in absolute ethanol at a total concentration of 0.2 mM in order to form a self-assembled monolayer [68]. We used the same protocol as described above for the preparation of biotin-functionalized thiol SAM surface comprising of dithiolalkanearomatic PEG6-COOH (COOH-dithiol) and dithiolalkanearomatic PEG3-OH (PEG-dithiol). After more than 24 hour incubation, substrates were removed from the solution, rinsed with absolute ethanol and dried in a stream of nitrogen.

Biomolecules were immobilized on gold surface with carboxylic acid terminated thiol SAM by using the following procedure. Firstly, a solution with EDC and NHS mixed in water at the concentrations of 0.4 M and 0.1 M, respectively, was flowed over the sensor surface with carboxylic group terminated thiol SAM for 20 min. Afterwards, biomolecules dissolved in 20 mM in ACT with pH 5.5 at a given concentration were flowed for 50 min in order to react with NHS moieties on the surface. Finally, 1 M ethanolamine hydrochloride solution was injected for 20 min in order to deactivate unreacted NHS ester groups and the sensor surface was rinsed with PBST buffer.

For the immobilization of biomolecules on the biotinylated SAM, a streptavidin solution in PBS at a concentration of 10 μg mL^{-1} was flowed over the sensor surface in order to form a monolayer of streptavidin. The vacancies of biotin binding sites facing the aqueous phase on streptavidin were used for immobilization of biotin-conjugated biomolecules.
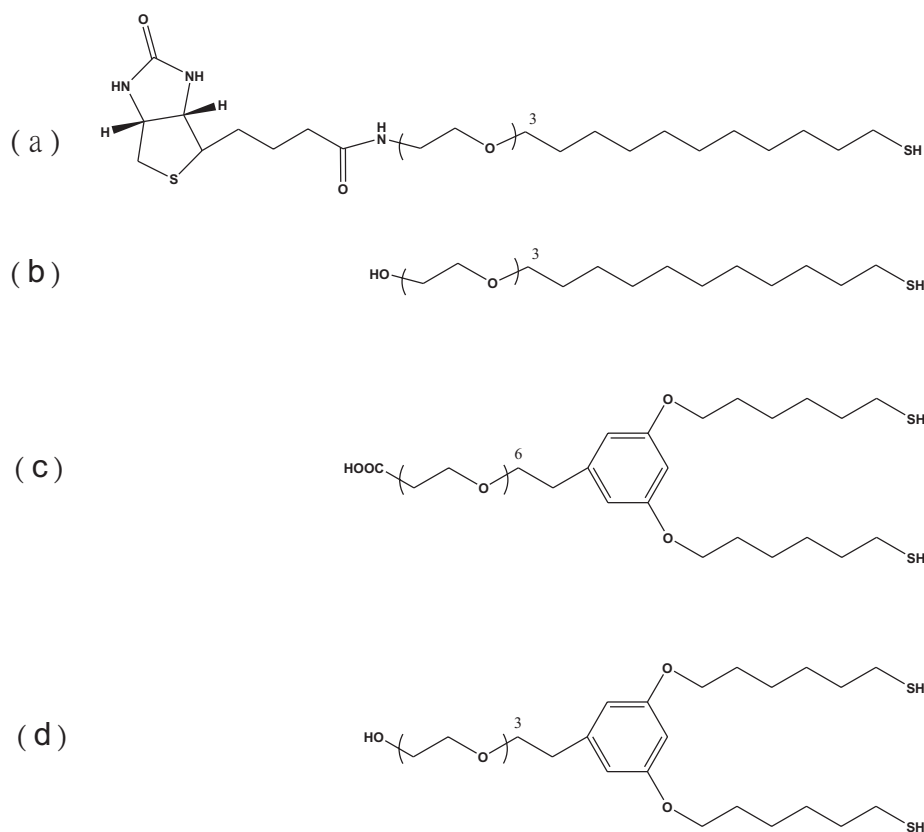
Figure 2.1: Chemical structures of SAM components including (a) monothiolalkane(C11) PEG3-Biotin, (b) monothiolalkane(C11) PEG3-OH, (c) dithiolalkanearomatic PEG6-COOH and (d) dithiolalkanearomatic PEG3-OH

2.3.2 NIPAAm hydrogel binding matrix

Synthesis of photo-crosslinkable NIPAAm hydrogel and benzophenone thiol was done by Basit Yameen, Alena Aulasevich and Martina Knecht at the Max-Planck Institute for polymer research, Germany. The synthesis processes are described in the literature [60]. The NIPAAm terpolymers were prepared by free radical polymerization of NIPAAm, sodium methacrylate (SMA) or methacrylic acid (MAA), and MaBP, initiated by AIBN as seen in Fig. 2.3a. The polymerization solvent for the SMA terpolymers was methanol, and that for the MAA terpolymers was dioxane. The reactions were performed at 60 °C under argon for 24 h. The polymers were precipitated directly from the reaction mixture in ice-cold diethyl ether, purified by reprecipitation from methanol into ice-cold diethyl ether and freeze-dried from tert-butanol in vacuum. The yield was between 64 and 83%.

NIPAAm films were deposited on gold surfaces and exploited as 3D binding matrices
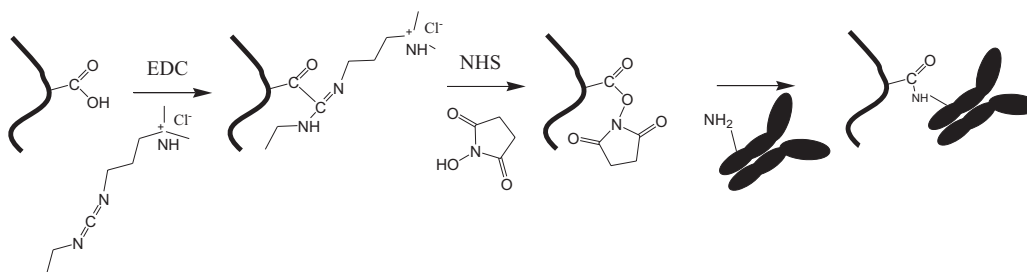
Figure 2.2: Biomolecule conjugation on surface through EDC/NHS coupling chemistry.
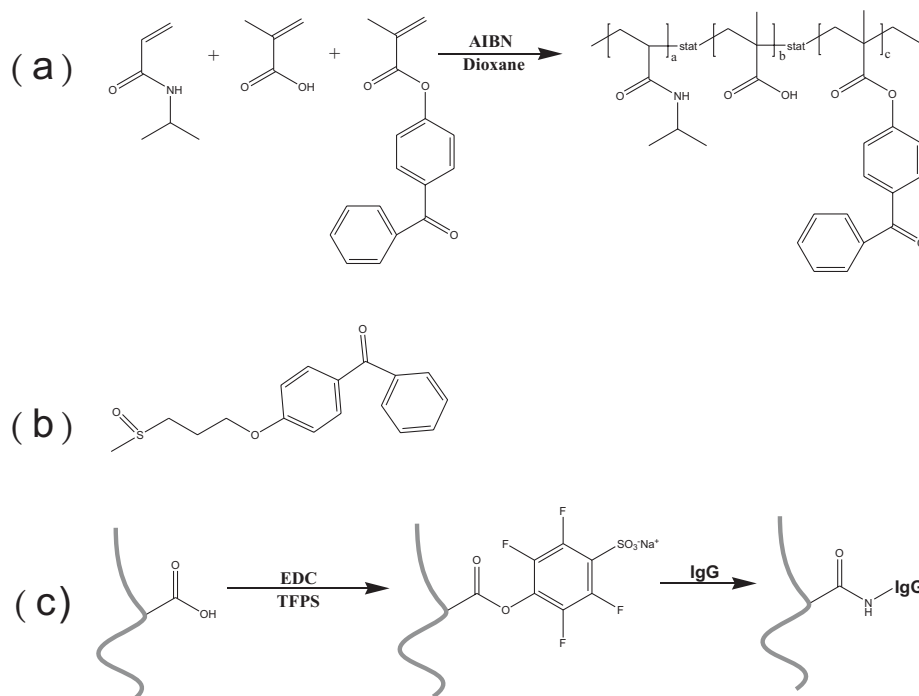
Figure 2.3: (a) Synthesis of photo-crosslinkable NIPAAm hydrogel. (b) Chemical structure of benzophenone-terminated thiol. (c) Modification of biomolecules in hydrogel through EDC/TFPS coupling chemistry.

in SPR biosensors. After preparation of gold films, the substrate was soaked overnight in a solution of benzophenone-terminated thiol (Fig. 2.3b, dissolved at a concentration of 1 mM in absolute ethanol that was purged with argon) in order to form a self-assembled monolayer (SAM). The modified gold surface was rinsed with absolute ethanol, dried in the stream of nitrogen and a thin NIPAAm-based polymer was deposited on its top by using spin-coating. A rotating speed of 2000 rpm was applied for 120 s and the thickness of the NIPAAm-based film was controlled by adjusting the concentration of the polymer (between 1 and 20 mg mL^{-1} in ethanol). Finally, the NIPAAm-based hydrogel was dried in a vacuum

oven at 50 °C followed by its simultaneous crosslinking and attachment to the gold surface via benzophenone groups by exposing to UV light (with an irradiation dose of 2 J cm^{-2} at a wavelength of λ = 365 nm) for 10 min.

Biomolecules were *in situ* covalently immobilized to the NIPAAm-based hydrogel matrix via its carboxylic moieties by using a protocol reported by Aulasevich [69]. Firstly, the hydrogel was swollen in ACT buffer at pH 4 followed by 20 min flow of a mixture of TFPS and EDC (dissolved at concentrations of 21 mg mL^{-1} and 75 mg mL^{-1}, respectively, in water) in order to form terminal TFPS ester moieties. Then, the surface was rinsed with ACT buffer for 3 minutes and a solution containing biomolecules was flowed through the flow-cell for 90 min. After the diffusion of biomolecules into the gel and their reaction with activated carboxylic groups, the gel was subsequently washed with ACT buffer for 10 min, incubated for 20 min in 1 M ethanolamine solution at pH 8.5 in order to block unreacted TFPS ester groups and then rinsed with the ACT buffer for 15 min, see Fig. 2.3c.

2.4 Optical setup for SPR and SPFS measurements

We used a home-built optical setup based on the attenuated total reflection (ATR) method with angular modulation of SPR. As shown in Fig. 2.4, a monochromatic light beam from a He-Ne laser emitting at a wavelength of λ = 632.8 nm (PL610P, Polytec, Germany, power 2 mW) or at a wavelength of $\lambda = 543.5$ nm (LK54010P, Laser Graphics, Germany, power 5mW) was linearly polarized using a polarizer, passed through a chopper (Princeton Applied Research, TN) and was coupled to a 90 degree LASFN9 glass prism. Onto the prism base, a glass slide with a layer structure supporting LRSPs (Cytop layer coated by a gold film with a thickness of d_m = 14.6 nm) or regular SPs (gold film with the thickness of d_m = 45 nm) was optically matched using immersion oil (Cargile, NJ). The intensity of the light beam reflected at the prism base was measured using a photodiode and a lock-in amplifier (Model 5210, Princeton Applied Research, TN). The angle of incidence of the light beam was controlled by using a rotation stage (Hans Huber AG, Germany) and the angular scans of the intensity of reflected light were measured as a function of the external angle of incidence θ. A flow-cell consisting of a poly(dimethylsiloxane) gasket and a glass support with drilled input and output ports (volume approximately 25 μL) was attached to the sensor surface to contain liquid samples. The input and output port of the flow-cell was connected to a peristaltic pump (Reglo, Ismatec, Switzerland) using rubber tubing (Tygoon R3607, from Ismatec, Switzerland) in order to flow the liquid sample along the sensor surface (a flow

rate of 500 μL min^{-1} was used). The fluorescence light emitted from chromophore-labeled molecules bound to the sensor surface was collected through the flow-cell by using a lens, the light at the excitation wavelength was blocked by a bandpass filter (670FS10-25, L.O.T.-Oriel, Germany) and the intensity of fluorescence light was detected by a photomultiplier tube (H6240-01, Hamamatsu, Japan) that was connected to a counter (53131A, Agilent, CA). If the fluorescence signal F exceeded the 10^6 counts per second (cps), attenuation filters were used in order to operate the photomultiplier in the linear regime. The control of the optical setup and the data collection were performed by using the software Wasplas developed at the Max Planck Institute for Polymer Research in Mainz, Germany.

Measured reflectivity spectra were fitted with transfer matrix-based model [70] implemented in Winspall software developed at the Max Planck Institute for Polymer Research in Mainz, Germany. The enhancement of the electromagnetic field upon the excitation of surface plasmon modes was calculated by using a transfer matrix-based algorithm written in Maple (Waterloo Maple Inc. Canada) by Jakub Dostalek.
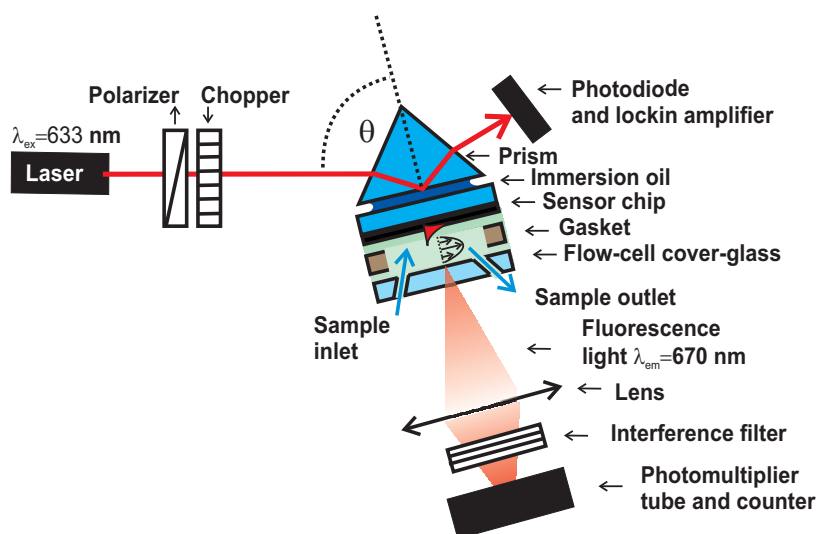
Figure 2.4: An optical setup supporting a biosensor based on SPFS integrated with prism coupler and the angular modulation of SPR.

2.4.1 Characterization methods

2.4.1.1 Atomic force microscopy

The examination of surface morphology was performed with the MultiMode scanning probe microscope (Veeco Instrumens, Santa Barbara, CA). Images were acquired in tapping mode

using micro cantilever (Olympus, Tokyo, Japan) with a spring constant of 42 Nm^{-1} and resonance frequency of 300 kHz. The root-mean-square (RMS) surface roughness was obtained from the height data and calculated from

$$RMS = \sqrt{\frac{\Sigma(Z_i - Z_{avg}^2)}{N}} \qquad (2.1)$$

where Z_i is the ith height sample out of N total samples and Z_{avg} is the mean height.

2.4.1.2 Contact angle measurement

Contact angle measurement is a simple method for surface analysis related to surface energy. We placed a 5 μL droplet of water onto the surface and the measurement system comprising with a charge-couple device (CCD) camera and an image processing software (DataPhysics Instruments, Filderstadt, Germany) was employed to determine the contact angle.

2.4.1.3 4-point collinear probe

The four-point collinear probe method was used for determining the conductivity of the novel metallic layers. The device was purchased from Keithley (Cleveland, OH) equiping with four equally spaced, 1 mm, probes to contact with a material with unknown resistance. The two outer probes are used for sourcing current and the other two inner probes are used for measuring the resulting voltage drop across the surface of the sample. The volume resistivity is calculated as follows:

$$\rho = \frac{\pi}{\ln 2} \times \frac{V}{I} \times t \qquad (2.2)$$

where ρ is volume resistivity (Ω·cm), V is the measured voltage (volts), I is the source current (amperes), and t is the sample thickness (cm).

2.4.1.4 Surface profiler

The thickness of thin films was determined by surface profiler (KLA-Tencor, P-10 and Alpha-step IQ, Milpitas, CA). The height step was prepared by scratching or patterning the thin film and it was measured by a scanning probe in a cross section profile. The measurement for vertical height can reach nanometer resolution.

2.4.1.5 Ellipsometry

Ellipsometry is an optical technique for surface analysis through measuring the shift in the phase of the reflected light. It was used for determing the refractive index of Cytop film. The Cytop film was spin-coated on a silicon wafer and baked at 160 $^\circ C$ for 1 h. The thickness of Cytop film was measured by using surface profiler. Afterwards, the refractive indices of Cytop was determined by an ellisometer at wavelengths ranging from $\lambda = 500$ to $\lambda = 700$ nm(EP[3]-MW, Nanofilm Technologie GmbH, Germany).

2.4.1.6 Particle size measurement

The particle size was measured by dynamic light scattering (DLS) with Zetasizer from Malvern Instruments (Worcestershire, UK). DLS measures the Brownian motion relevant to the size of particle in an aueous solution. The size of the particle is calculated according to the Stokes-Eistein equation:

$$d_H = \frac{kT}{3\pi\eta D} \tag{2.3}$$

where d_H is the hydrodynamic diameter, k Boltzmann's constant, D the diffusion coefficient and η viscosity. The temperture of the device was controlled at 25 $^\circ C$.

3 Excitation of long range surface plasmons

3.1 Optimization of layer structure supporting LRSPs

In this section, we investigate the excitation of LRSPs on a biosensor-compatible layer structure consisting of a Cytop fluoropolymer, thin gold film modified by thiol self assembled monolayer for coupling of receptor biomolecules and an aqueous sample on its top. The morphology, optical and electrical properties of the layer structure are determined and related to the performance of a SPFS biosensor. Through increasing the surface energy of Cytop fluoropolymer by O_2 plasma, more compact gold films that exhibit lower roughness were prepared, which resulted in a higher binding capacity, decreased non-specific adsorption of biomolecules to the biosensor surface and in a larger enhancement of electromagnetic field intensity accompanied with the excitation of LRSPs.

3.1.1 Introduction

As LRSP mode can propagate with orders of magnitude lower damping and its excitation is associated with narrower resonance compared to regular SPs, LRSPs attracted a great deal of attention in areas including integrated optical circuits [71, 72] non-linear optics [73, 74, 75] photo-acoustics [76], characterization of thin films [77] and biosensors [28, 21, 78, 79, 80, 81]. In biosensor applications, LRSPs are used to probe the binding of target molecules contained in an aqueous sample to biomolecular recognition sites anchored on a metallic sensor surface. The spectroscopy of LRSP was employed for the measurement of refractive index changes induced by molecular binding [79, 80]. Due to their lower damping, LRSPs allow the measurement of smaller refractive index variations [21] and thus provide more accurate detection of biomolecular binding events than the conventional surface plasmon resonance (SPR) sensors. In addition, LRSPs were employed in surface

plasmon-enhanced fluorescence spectroscopy (SPFS) biosensors [28, 80]. In this method, the binding of molecules labeled with a fluorophore is observed from changes in the intensity of fluorescence light emitted from the metallic sensor surface. SPFS takes advantage of the strong enhancement of the intensity of electromagnetic field upon the excitation of surface plasmons which directly increases the fluorescence signal from fluorophore-labeled molecules adhered to the surface [22, 82].

The majority of biosensors that exploit LRSPs relies on a layer structure consisting of a low refractive index buffer layer and a thin noble metal film (gold or silver). In these implementations, the refractive index of the buffer layer has to match to that of aqueous samples (close to 1.33 at the wavelength of $\lambda = 632.8$ nm) in order to achieve a symmetrical refractive index structure needed for the excitation of LRSPs. Up to date, fluoropolymers deposited by spincoating [79, 81] or sputtering [83] and low refractive index dielectric layers such as aluminum fluoride [84] or magnesium fluoride [81] prepared by thermal evaporation were used for the construction of layer systems supporting LRSPs. In this contribution, we investigate thin gold films deposited on a Cytop fluoropolymer for the excitation of LRSPs on the surface of a SFPS biosensor, see Fig. 3.1. The characteristics of these films are related to the performance of this method by using a model experiment in which the affinity binding of protein molecules was observed through probing by LRSPs.
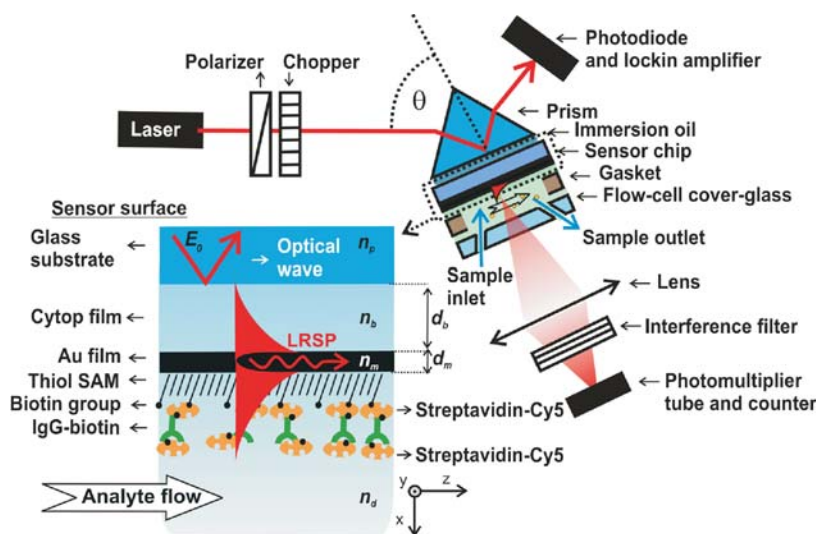
Figure 3.1: Layer structure and optical setup for the excitation of LRSPs and its implementation of SPR and SPFS biosensing.

3.1.2 Materials and methods

Cy5-conjugated streptavidin (SA) and ethanolamine hydrochloride were purchased from Sigma-Aldrich (St. Louis, MO, USA). Biotin-labeled polyclonal antibody (IgG) was from Acris Antibodies (Hiddenhausen, Germany).

The surface morphology of the prepared layers was observed by using the MultiMode atomic force microscopy (AFM, Veeco Instrumens, Santa Barbara, CA). Images were acquired in the tapping mode using a micro cantilever (Olympus, Tokyo, Japan) with a spring constant of 42 Nm^{-1} and resonance frequency of $\sim$300 kHz. Thicknesses of thin films were determined by using a surface profiler (KLA-Tencor P-10). An ellipsometer EP^3-MW (Nanofilm Technologie GmbH, Germany) was used for the measurements of the refractive index of the thin Cytop films. The changes in surface energy were investigated at room temperature by using contact angle measurements and image processing software (DataPhysics Instruments, Filderstadt, Germany). The four-point collinear probe method was used for determining the resistivity of the gold layers deposited on top of Cytop. The device was equipped with four equally spaced (1 mm) probes and was purchased from Keithley (Cleveland, OH). The two outer probes are used for sourcing current and the other two inner probes are used for measuring the resulting voltage drop across the surface of the sample. The volume resistivity is calculated as $\rho = \pi(\ln 2)^{-1}VI^{-1}d_m$, where ρ is volume resistivity (Ω cm), V is the measured voltage, I is the source current, and d_m is the gold layer thickness.

3.1.3 Results and discussion

3.1.3.1 Characterization of multilayer structure

The refractive index of a Cytop layer was measured by ellipsometry at wavelengths between λ = 500 and λ = 700 nm. The obtained data presented in Fig. 3.2a reveal that Cytop exhibits the refractive index of $n_b = 1.340$ and $n_b = 1.337$ at the wavelengths of $\lambda = 543.5$ nm and $\lambda = 632.8$ nm, respectively. In general, fluoropolymers exhibit a low surface energy which complicates their coating or bonding. In order to increase their surface energy, plasma or chemical etching was used [85]. As seen in Fig. 3.2b, exposing the Cytop layer to O_2 plasma etching for 30 seconds resulted in an increase in the surface energy which is manifested as a decrease in the contact angle from 117.0 deg to 102.9 deg. Further increasing the O_2 plasma etching time did not change the contact angle significantly but the AFM characterization revealed that the root means square (rms) roughness σ of the Cy-

top surface gradually increased with the plasma etching time. For instance, 30 second O_2 plasma etching caused an increase in the rms roughness from 0.47 to 0.84 nm. In further experiments, we deposited gold films on Cytop surface not etched with plasma (abbreviated as Cyt), on the Cytop surface that was exposed to plasma etching for 30 seconds (abbreviated as Cyt-O_2) and directly on LASFN9 glass. The rms roughness of the gold film with the thickness of $d_m = 14.6$ nm deposited on Cyt-O_2 surface ($\sigma = 1.1$ nm) was approximately 2.5-fold lower than that observed on the Cyt surface ($\sigma = 2.8$ nm) and it was comparable to the roughness of 45 nm thick gold film deposited on a polished LASFN9 glass slide ($\sigma = 1.0$ nm).
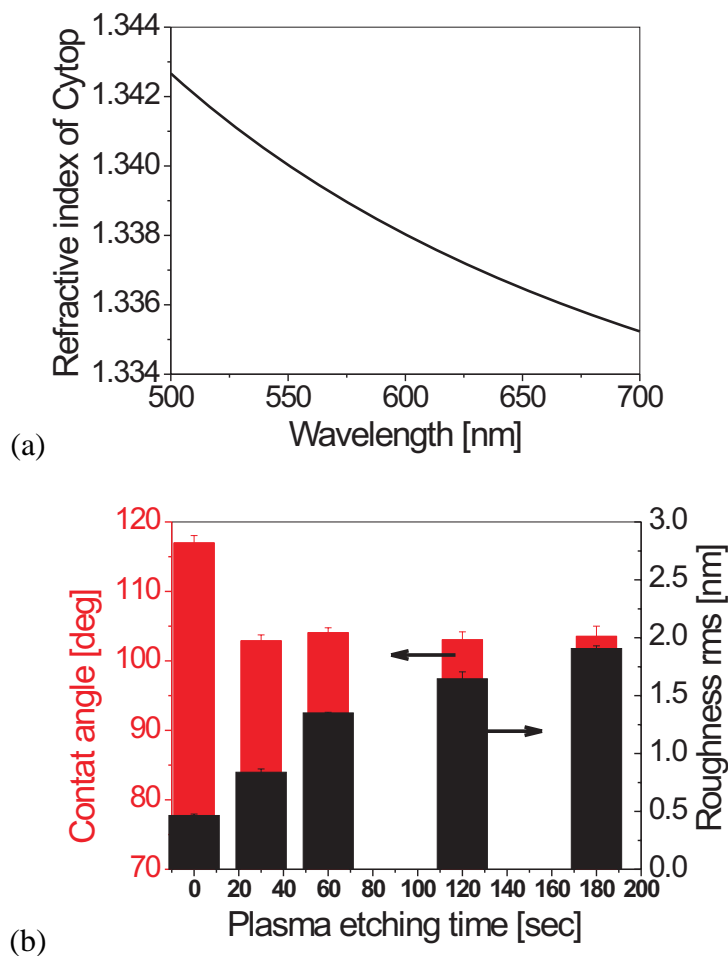
Figure 3.2: (a)Refractive index dispersion n_b and (b) the dependence of contact angle and roughness on the O_2 plasma etching time of Cytop polymer. (Courtesy to Dr. Andreas Unger for ellipsometry measurements)

Fig. 3.3a shows the dependence of the resistivity of gold films deposited on Cyt-O_2 and

Cyt surfaces on their thickness d_m. On the Cytop polymer not exposed to O_2 plasma etching, the coalescence transition was observed at a thickness of roughly $d_m = 20$ nm. In contrast to that, the resistivity below 3×10^{-5} Ω cm was observed for gold films prepared on plasma-etched Cytop with the thickness down to $d_m = 7$ nm. These data indicate that more compact gold films can be prepared on a Cyt-O_2 surface than on a pristine Cyt surface. In addition, let us note that the adhesion strength of gold film to the Cytop polymer on Cyt-O_2 surface was greatly increased compared to that on Cyt surface as tested by the "scotch tape test". Fig. 3.3b shows the comparison of the thickness of gold films d_m deposited under identical conditions on Cyt-O_2 and glass surfaces. It reveals that the thickness measured on the Cytop surface is lower than the one on glass. The reason for this observation is probably due to the lower surface density of clusters from which the layer starts to grow on the Cytop.

3.1.3.2 Excitation of long range surface plasmons

We used a layer structure comprising a gold film with a thickness of $d_m = 14.6$ nm sandwiched between water and the Cytop layer on the top of a glass substrate for the excitation of LRSPs. In order to achieve full coupling to LRSPs, the thickness of the Cytop buffer layer was adjusted to $d_b = 1150$ nm for a wavelength $\lambda = 632.8$ nm and to $d_b = 521$ nm for a wavelength $\lambda = 543.5$ nm. As Fig. 3.4a shows, the measured angular reflectivity spectra exhibit a dip associated with the resonant excitation of LRSPs centered at the angles of incidence $\theta = 48.2$ and 46.7 deg for the wavelength $\lambda = 632.8$ and 543.5 nm, respectively. For the gold film on Cyt-O_2, the full width in the half minimum (FWHM) of the LRSP resonance of $\Delta\theta = 0.18$ deg and $\Delta\theta = 0.9$ deg were measured at the wavelengths $\lambda = 632.8$ nm and $\lambda = 543.5$ nm, respectively. The LRSP resonance width $\Delta\theta$ for the Cyt-O_2 structure was of about 20 per cent lower compared to that on the Cyt structure. Moreover, the excitation of regular surface plasmons (SP) on a structure with a gold film deposited on glass substrate with the thickness of $d_m = 45$ nm is presented in Fig. 3.4b. The coupling to SPs is manifested as resonant dip centered at a higher angles of incidence and with an order of magnitude larger FWHM compared to that for LRSPs. FWHM of $\Delta\theta = 4.1$ deg at a wavelength of $\lambda = 632.8$ nm and $\Delta\theta > 10$ deg at the wavelength $\lambda = 543.5$ nm were observed for the excitation of SPs.

The measured reflectivity spectra in Fig. 3.4a and Fig. 3.4b were fitted by using the method of least squares and transfer matrix-based model in order to determine the optical properties of gold films [70]. In this analysis, we approximated the gold film as a homoge-

(a)

(b)
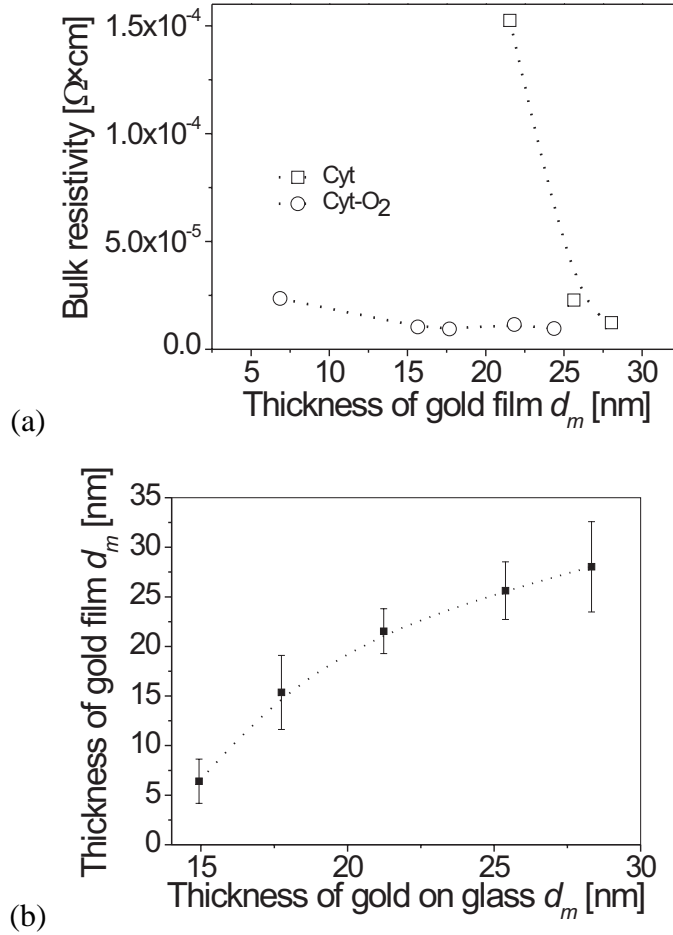
Figure 3.3: (a) Thickness dependence of the bulk resistivity of gold film deposited on Cytop surface etched with O_2 plasma (Cyt-O_2) and not etched with O_2 plasma (Cyt). (b) The difference of the thickness of gold film d_m deposited by using thermal evaporation on a LASFN9 glass and on Cyt-O_2 surface.

nous slab with an (effective) refractive index n_m and a thickness d_m that was measured by a surface profiler. The refractive index n_b and thickness d_b of Cytop layer, refractive index of water n_d and LASFN9 glass substrate n_p were determined by other methods or taken from literature as summarized in the Tab. 3.1. The refractive index of a gold film deposited with the thickness of $d_m = 45$ nm was fitted as $n_m = 0.12 + 3.561i$ for the wavelength $\lambda = 632.8$ nm and as $n_m = 0.41 + 2.32i$ for the wavelength $\lambda = 543.5$ nm. These values lie within the range reported in the literature [86, 87, 88]. For 14.6 nm thick gold film on Cyt-O_2 surface, the refractive indices of $n_m = 0.31 + 2.9i$ and $n_m = 0.66 + 2.4i$ were determined at a wavelengths of $\lambda = 632.8$ nm and $\lambda = 543.5$ nm, respectively. These data show that a thinner

(a)

(b)
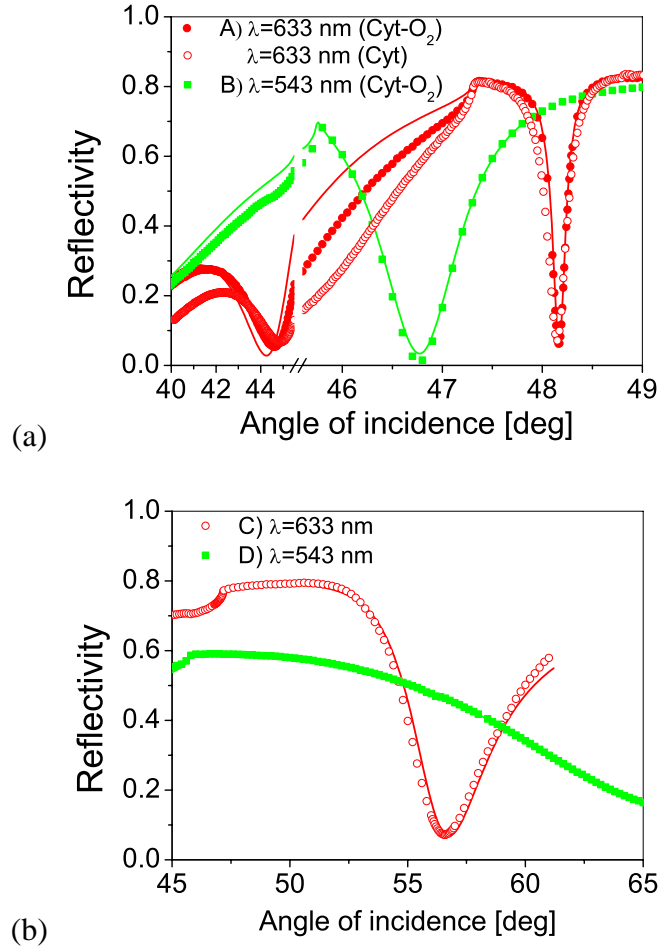
Figure 3.4: ((a) Reflectivity spectra for the excitation of LRSPs on a gold film with the thickness of $d_m = 14.6$ nm deposited on Cyt-O_2 and Cyt surfaces. (b) Reflectivity spectra for the excitation of regular SPs on a 45 nm thick gold deposited on LASFN9 glass surface. The spectra were measured at the wavelengths of $\lambda = 543.5$ (squares) and $\lambda = 632.8$ nm (circles) and fitted with a transfer matrix-based model (lines).

gold film on Cyt-O_2 surface exhibits changed real part of the refractive index $Re\{n_m\}$ and a decreased imaginary part of the refractive index $Im\{n_m\}$ which can be ascribed to the morphology changes. Let us note that the reflectivity spectrum for gold film deposited on Cytop surface without plasma etching (Cyt) was not possible to fit under the aforementioned approximations. Based on the determined parameters of the layer structures stated in Tab. 3.1, we calculated the electric intensity field enhancement at the gold surface upon the resonant coupling to LRSPs and regular SPs. These simulations presented in Fig. 3.5 show that the excitation of LRSPs at the wavelength $\lambda = 632.8$ nm provides larger enhancement of the

electric intensity field in the vicinity to the gold surface ($|E|^2/|E_0|^2 = 88$) compared to that at the wavelength of $\lambda = 543.5$ nm ($|E|^2/|E_0|^2 = 19$) for which the Ohmic losses in the gold are higher. As LRSPs propagate with lower damping than regular SPs, their excitation on the metallic surface provides stronger enhancement of electromagnetic field. In comparison to the excitation of regular SPs, the coupling to LRSPs on the prepared structures provides approximately two and three-fold increased enhancement of electric intensity field at the wavelength $\lambda = 632.8$ nm and $\lambda = 543.5$ nm, respectively. Let us note that the changes in the $Re\{n_m\}$ and the decrease in the $Im\{n_m\}$ of gold films prepared with the thickness of $d_m = 14.6$ nm on Cytop shortens the propagation length of LRSPs and thus reduces the enhancement of electromagnetic field intensity. For instance, the simulations predict that at the wavelength of $\lambda = 632.8$ nm the excitation of LRSPs is accompanied with the enhancement of electric intensity field $|E|^2/|E_0|^2 = 282$ assuming a Cytop layer ($d_b = 1390$ nm) and gold film ($d_m = 14.6$ nm) with the refractive index identical to that for the 45 nm thick gold layer ($n_m = 0.12 + 3.561i$). This field intensity enhancement is approximately three-fold higher than that for the prepared gold film of which refractive index was determined as $n_m = 0.31 + 2.9i$.

3.1.3.3 SPR and SPFS observation of affinity binding

Fig. 3.6 shows the angular scans of the reflected and fluorescence light intensity measured after the successive binding of SA, IgG and SA layers on a gold surface with thiol SAM biotin moieties. Fig. 3.6a reveals that upon the binding of protein layers on the gold film deposited on Cyt-O_2 surface, the dip in the reflectivity spectrum due to the resonant excitation of LRSP shifts to the higher angles of incidence. After the binding of streptavidin labeled with Cy-5 chromophore, strong peak in the fluorescence spectrum rises at the angles of incidence for which the excitation of LRSP provides strongest enhancement of electromagnetic field. Similarly, Fig. 3.6b shows the changes in the reflectivity and fluorescence intensity spectra upon the assembly of protein layers on the 45 nm thick gold film probed with regular SPs. By fitting the measured reflectivity spectra and by assuming that the refractive index n on the sensor surface changes with the protein concentration c as $\partial n/\partial c \approx 0.17$ μL mg^{-1} [31], we calculated the surface coverage Γ of protein layers adhered to the metallic surface as summarized in Tab. 3.2. These results show that the first and second streptavidin layers were immobilized with the surface coverage in the range $\Gamma = 1$-2 ng/mm^2 that is comparable with previously published results [68]. Probably owing to the more compact thiol SAM on a gold surface with lower roughness, approximately 20 per cent larger surface coverage Γ of

Table 3.1: Parameters of layer structures and characteristics of LRSPs (A and B) and regular SPs (C and D) excited at wavelengths $\lambda = 632.8$ and 543.5 nm.

Sample	Wavelength (nm)	Substrate and superstrate	Buffer layer	Gold film	Resonance FWHM (deg)	$|E|^2/|E_0|^2$
A	$\lambda = 632.8$	$n_p = 1.845$ $n_d = 1.333^a$	$n_b = 1.337$ $d_p = 1150$ nm	$Re\{n_m\} = 0.31 \pm 0.07$ $Im\{n_m\} = 2.9 \pm 0.3$ $d_m = 14.6 \pm 0.5 nm$	$\Delta\theta = 0.18$	88
B	$\lambda = 543.5$	$n_p = 1.845$ $n_d = 1.335^a$	$n_b = 1.340$ $d_p = 521$ nm	$Re\{n_m\} = 0.66 \pm 0.05$ $Im\{n_m\} = 2.4 \pm 0.2$ $d_m = 14.6 \pm 0.5$ nm	$\Delta\theta = 0.9$	19
C	$\lambda = 632.8$	$n_p = 1.845$ $n_d = 1.333^a$	$\cdots$	$Re\{n_m\} = 0.124 \pm 0.002$ $Im\{n_m\} = 3.561 \pm 0.002$ $d_m = 45 \pm 1$ nm	$\Delta\theta = 4.1$	43
D	$\lambda = 543.5$	$n_p = 1.845$ $n_d = 1.335^a$	$\cdots$	$Re\{n_m\} = 0.41 \pm 0.01$ $Im\{n_m\} = 2.32 \pm 0.003$ $d_m = 45 \pm 1$ nm	$\Delta\theta > 10$	6.3

[a]Reference [89].
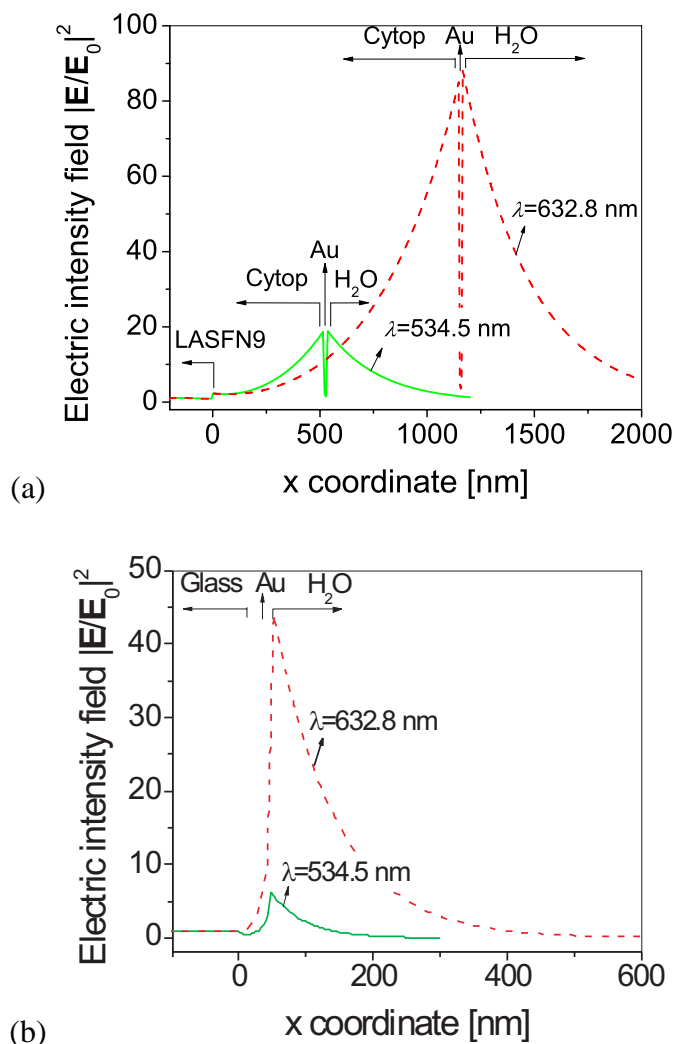
Figure 3.5: Simulations of profile of electric intensity field upon the resonant coupling to (a) LRSP and (b) SP at wavelengths of $\lambda = 543.5$ nm (solid line) and $\lambda = 632.8$ nm (dashed line) calculated for the layer parameters in Tab. 3.1

.

SA layers was observed on the 45 nm thick gold film compared to that on the 14.6 nm thick gold film. Due to the higher enhancement of electric field intensity, 2.1 and 1.8 fold stronger peak fluorescence signal was observed upon the probing the first and second streptavidin layer, respectively, by LRSPs on 14.6 nm gold film attached to Cyt-O_2 surface (16.5×10^4 and 82.5×10^4 counts per second (cps), respectively) compared to that probed with regular surface plasmons on 45 nm thick gold film (8.1×10^4 and 45×10^4 cps, respectively). The fluorescence signal from the second SA film is approximately 5-fold higher compared to that from the first SA layer owing to the decreased fluorescence quenching by Förster energy

transfer [22]. The angular scans of the fluorescence intensity measured after the 30 min flow of a streptavidin solution across the thiol SAM without biotin moieties revealed that the peak fluorescence signal increased due to the non-specific sorption to the surface of 0.3×10^4 and 0.9×10^4 cps for the probing with regular SPs and LRSPs, respectively. The sensor surface supporting the excitation of regular SPs showed smaller nonspecific signal because of the lower enhancement of electromagnetic field intensity and lower non-specific sorption on the SAM with lower amount of defects. In addition, prior to the affinity binding of protein layers, the background signal was measured. Higher fluorescence signal of 3.6×10^4 was observed for the excitation of LRSPs compared to 0.8×10^4 cps observed for the excitation of regular SPs. The reason for this observation is probably due to the higher scattering on rougher surface and higher intensity of the auto-fluorescence light emitted transmitted from the prism through the thinner metallic film supporting LRSPs.

The time kinetics of the reflectivity and fluorescence signal were measured at an angle of incidence fixed to $\theta = 48.02$, 48.08 and 56.02 deg for the excitation of LRSPs on a gold film deposited on Cyt-O_2 and Cyt surface and for the excitation of regular SPs, respectively. The Fig. 3.7a shows the time evolution of the fluorescence signal and surface coverage Γ during the successive growth of SA, IgG and SA layer on the sensor surface. In addition, Fig. 3.7b compares in detail the reflectivity and fluorescence signal kinetics upon the growth of the first SA layer on the thiol SAM with biotin moieties on the 14.6 nm thick gold films deposited on Cyt and Cyt-O_2 surface and on the 45 nm thick gold film deposited on glass. On all surfaces, the fluorescence signal increases due to the binding of SA labeled with Cy5 chromophore and it saturates after 3 minutes. However, the time evolution of reflectivity changes reveals that on smoother 45 nm thick gold film on glass the response saturates faster (approximately after 3 minutes) compared to that on rougher 14.6 nm thick gold film on Cyt surface (more than 30 min). The reason for this observation is probably that two binding mechanisms are superimposed. The fast changes in the sensor signal within 3 minutes after the sample injection is probably due to the affinity binding of SA to biotin moieties in the surface. The slower response can be attributed from nonspecific binding on a surface due to the defects in the thiol SAM that are more pronounced on rougher surfaces. The fact that this binding mechanism does not change the fluorescence signal indicates that the binding probably occurs directly on the gold surface where it is strongly quenched.

Table 3.2: The summary of surface coverages and excited peak fluorescence intensities of bound protein layers on the biotin-functionalized metallic surfaces deposited on $Cyt\text{-}O_2$, Cyt and glass.

	LRSP (Au/Cyt-O_2/glass)	LRSP (Au/Cyt/glass)	SP (Au/glass)
Gold surface rms roughnes (nm)	1.1	2.8	1.0
First SA layer: Γ (ng/mm^{-2})	1.3	...	1.6
IgG layer: Γ (ng/mm^{-2})	0.7	...	1.7
Second SA layer: Γ (ng/mm^{-2})	1.1	...	1.3
First SA layer: F (10^4 counts/s)	16.9	12.3	8.1
Second SA layer: F (10^4 counts/s)	82.5	32.6	45
None-specific binding: F (10^4 counts/s)	0.9	1.3	0.3
Background: F (10^4 counts/s)	3.6	2.8	0.8

(a)

(b)
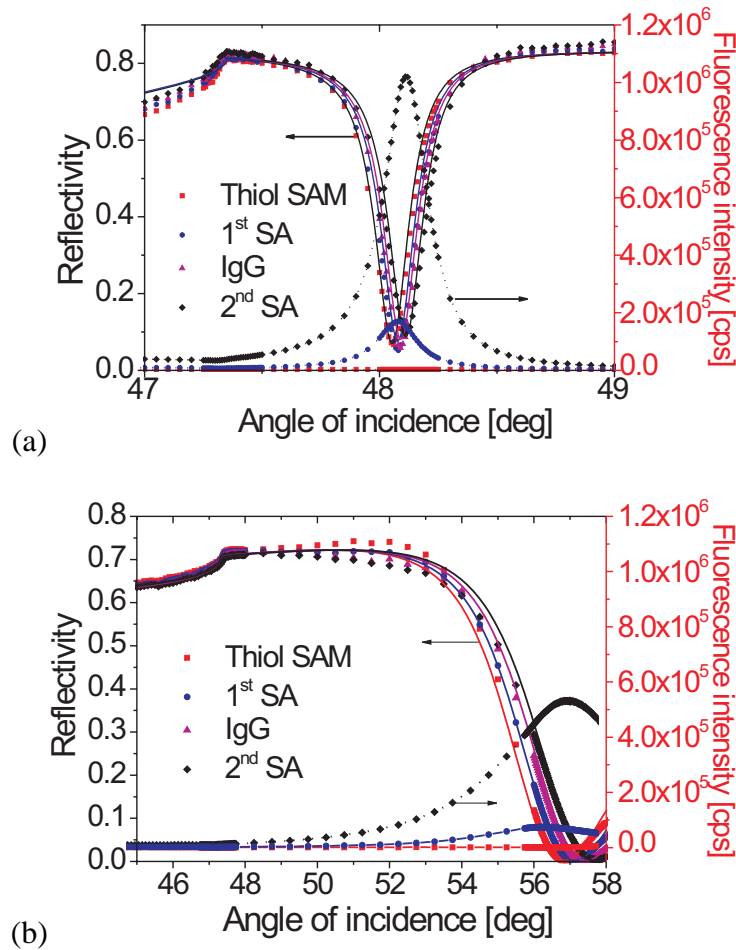
Figure 3.6: (a) Angular scans of reflectivity and fluorescence signal measured for protein layer assembly and the excitation of LRSPs on the surface with 14.6nmthick gold surface on Cyt-O_2. (b) Angular scans of reflectivity and fluorescence signal measured for protein layer assembly and the excitation of SPs on the surface with 44 nm thick gold surface on glass.

3.1.4 Summary

We examined the characteristics of thin gold films deposited by thermal evaporation on Cytop fluoropolymer layer and investigated how they affect the performance of biosensors based on surface plasmon resonance (SPR) and surface plasmon-enhanced fluorescence spectroscopy (SPFS) employing the excitation of long range surface plasmons (LRSPs). We observed that the roughness of gold films deposited on Cytop is higher compared to that for gold films deposited on glass due to the low surface energy of Cytop fluoropolymer. The increasing surface energy of Cytop by etching with O_2 plasma allowed the preparation
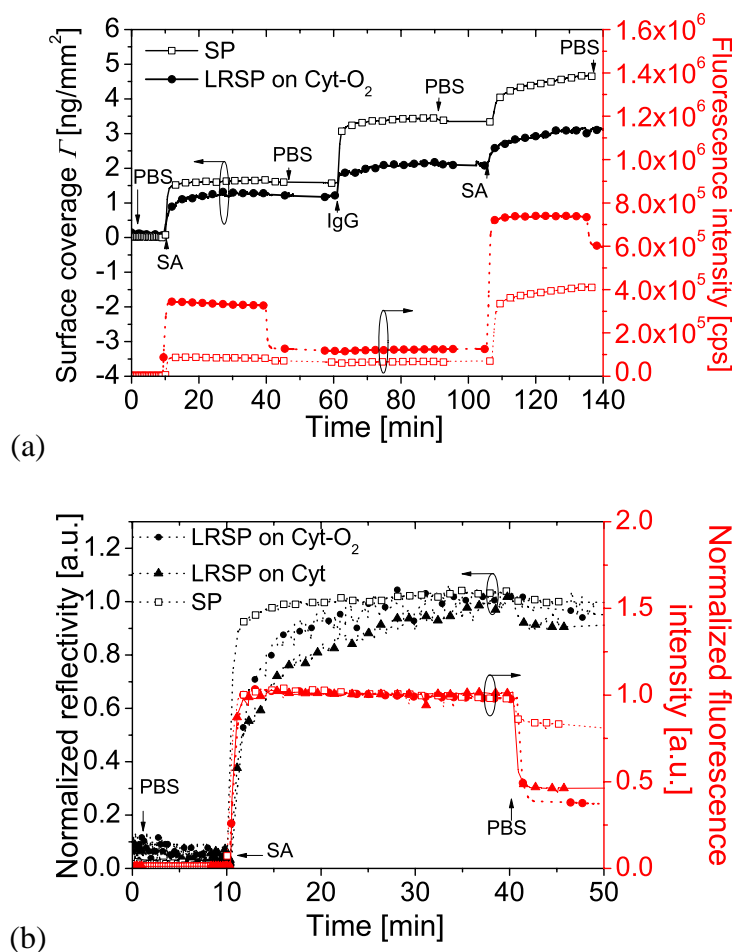
Figure 3.7: (a) Comparison of the time evolution of the reflectivity and fluorescence signal measured upon the affinity binding of Cy-5-labeled streptavidin to the thiol SAM with biotin moieties on the surface with 14.6 nm thick gold film deposited on Cyt and Cyt-O_2 surface and on the 45 nm thick gold film deposited on glass. (b) Time evolution of the surface coverage and fluorescence signal upon the successive affinity binding of streptavidin, IgG and streptavidin on the surface with 14.6 nm thick gold surface on Cyt-O_2 probed with LRSPs and on 45 nm thick gold film on glass probed with SP.

of smoother and more compact gold films. The prepared layer structures were used for the SPR and SPFS-based observation of affinity binding of protein molecules to the sensor surface that was modified by mixed thiol SAM. The results revealed that the gold roughness affects the binding capacity and non-specific interactions of protein molecules with the surface. By using the prepared structures for excitation of LRSPs, approximately two-fold increased enhancement of electric intensity field and fluorescence signal in close proximity

to the surface was observed with respect to conventional SPFS. The simulations predict that further improving of the quality gold films on Cytop surfaces would allow for additional three-fold increasing the enhancement of electric intensity field through the excitation of LRSP on a surface of studied SPFS biosensor.

4 Implementation of hydrogel binding matrix for evanescent wave biosensors

In this dissertation, SPR- and SPFS-based biosensor platforms with a responsive N-isopropyl-acrylamide (NIPAAm) hydrogel binding matrix were developed. This binding matrix highly swells in aqueous environment and it can be modified with receptor biomolecules by using active ester coupling chemistry. The implementation of a large-binding capacity NIPAAm-based matrix for sensitive detection of target analyte was carried out. The results presented in this chapter are structured as follows:

1. Amplification of the SPFS signal through triggering the collapse of hydrogel is discussed in Section 4.1. We demonstrate that the collapse of the hydrogel matrix results in the enhancement of measured fluorescence intensity owing to the increase in the concentration of captured molecules within the evanescent field of surface plasmons.

2. The role of diffusion mass transfer in functionalized hydrogel binding matrix on the performance of LRSP-FS is introduced in Section 4.2. Experimental observations were supported by numerical simulations of mass transfer and affinity binding of target molecules in the hydrogel in order to optimize the hydrogel thickness and profile of the probing evanescent wave.

3. Immunoassay-based experiments in hydrogel optical waveguide spectroscopy (HOWS) and hydrogel optical waveguide mode-enhanced fluorescence spectroscopy (HOW-FS) are shown in Sections 4.3 and 4.4, respectively. The hydrogel films attached to metallic surfaces can serve as hydrogel optical waveguides (HOWs) which exhibit more than an order of magnitude lower damping than surface plasmons. We applied HOW modes in a refractometric- and fluorescence-based biosensors for detection of model immunoassay system and hCG biomarker.

4.1 Stimuli-responsive hydrogel for enhancement of fluorescence intensity in SPFS

4.1.1 Motivation

The responsive hydrogel based on poly(N-isopropylacrylamide) (NIPAAm) [60] can be used as a binding matrix in an SPFS biosensor and that offers additional features enabling increasing its sensitivity. The used NIPAAm-based hydrogel matrix can be prepared with higher thickness (up to several micrometers) and it can be functionalized by receptor molecules with a high surface density [69]. We observe the affinity binding of antibodies against mouse IgG antibodies covalently anchored in the NIPAAm-based hydrogel via detection of the induced refractive index variations (SPR) and fluorescence light emission (SPFS), see Fig. 4.1. However, the binding events taking place beyond the evanescent SP field can not be probed. Therefore, the intrinsic responsive property of hydrogel can be utilized to compact the bound analytes into the sensing field through the collapse of the NIPAAM-hydrogel triggered by external stimulus.
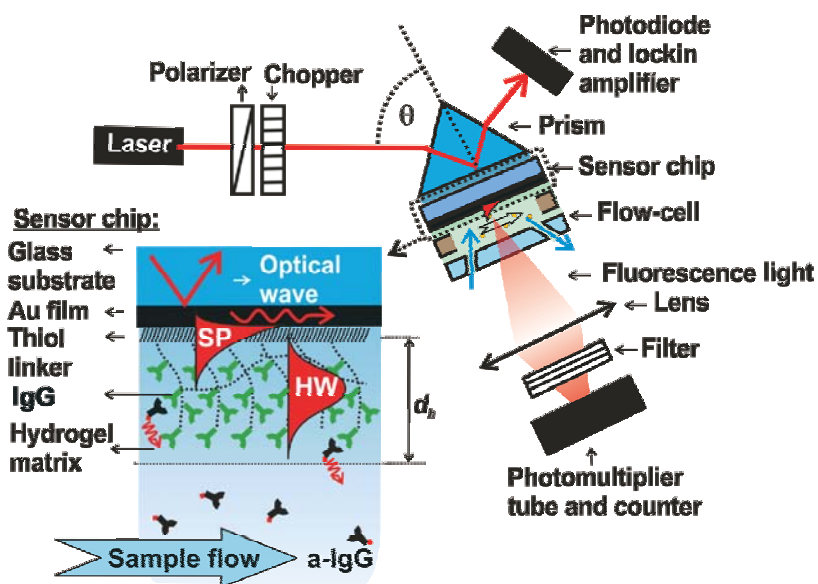
Figure 4.1: Scheme of the optical setup of SPFS sensor with a hydrogel binding matrix.

4.1.2 Materials and methods

Mouse immunoglobulin G (IgG) and goat anti-mouse IgG (a-IgG) labeled with Alexa 633 were obtained from Abcam (Cambridge, UK). The synthesis and modification of the NIPAAm-based hydrogel were described in Subsection 2.3.2.

4.1.3 Results and discussion

4.1.3.1 Immobilization of ligands and affinity binding of target molecules

The *in situ* immobilization of mouse IgG molecules was probed with surface plasmons excited at the interface between the gold and the hydrogel film, see Fig. 4.1. The time kinetics of the reflectivity measured at the angle of incidence of $\theta = 58.2°$ upon the immobilization of IgG molecules can be found in Fig. 4.2a. Firstly, the ACT buffer was flowed through the flow-cell for 30 min in order to stabilize the sensor response. The fitting of the angular reflectivity spectrum measured upon the flow of ACT buffer revealed that the swollen hydrogel film exhibited the thickness of $d_h = 607$ nm and its refractive index was $n_h = 1.349$, see Fig. 4.2a. In order to covalently conjugate mouse IgG with the hydrogel film, the carboxyl groups within the gel were activated by the incubation in a solution with EDC/TFPS followed by the flow of IgG molecules dissolved in ACT buffer at a concentration of 100 μg mL, incubation in ethanolamine and rinsing with ACT in order to wash out unbound molecules. The analysis of reflectivity spectrum measured after the ACT rinsing showed that the thickness of hydrogel decreased to $d_h = 454$ nm and its refractive index increased to $n_h = 1.370$. Afterwards, the PBS at pH 7.4 was injected to the flow-cell resulting in the increase of hydrogel thickness to $d_h = 684$ nm and a decrease in the refractive index to $n_h = 1.353$. The variations in the thickness d_h upon the modification of the hydrogel matrix by IgG molecules were probably due to the changes in its net charge. As summarized in Tab. 4.1, the measured optical parameters of the gel film corresponds to its surface mass of $\Gamma = 42$ ng/mm^2 and $\Gamma = 67$ ng/mm^2 prior and after the binding of mouse IgG molecules, respectively. These data indicate that the surface mass density of covalently coupled mouse-IgG was of 25 ng/mm^2.

The affinity binding of anti-mouse IgG antibodies (a-IgG) tagged with Alexa 633 chromophore was observed from the variations in surface plasmon resonance as well as by surface plasmon-enhanced fluorescence spectroscopy. In this experiment, we changed the angle of incidence to $\theta = 58.7$ deg and measured time evolution of the reflectivity and fluorescence intensity upon 100 minute flow of a-IgG molecules dissolved in PBS at the con-
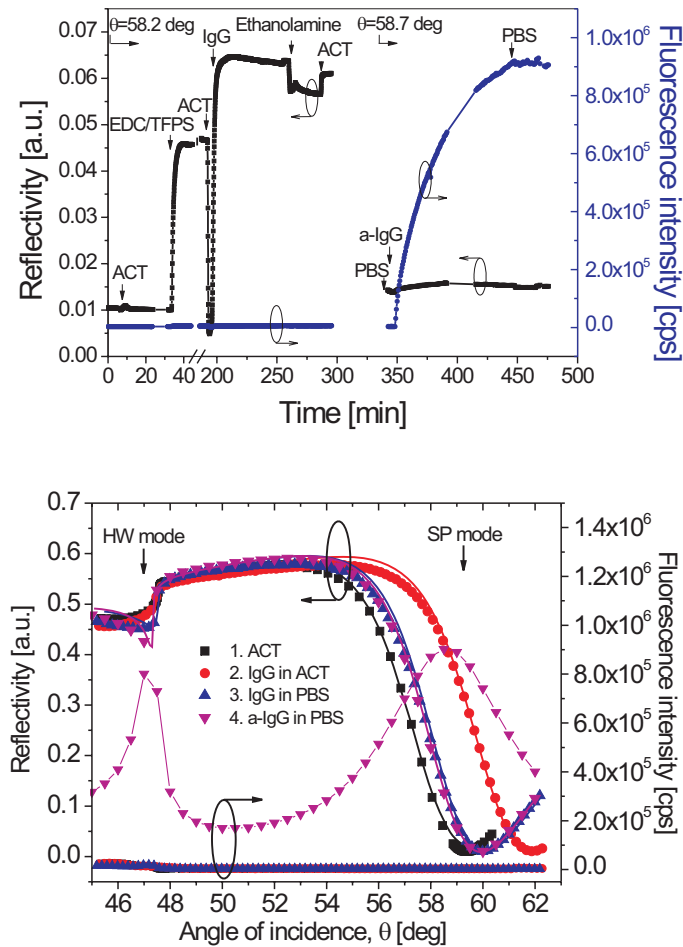
Figure 4.2: (a) Time evolution of the reflectivity and fluorescence signal measured at a fixed angle of incidence and (b) the angular reflectivity and fluorescence intensity spectra upon the covalent coupling of mouse-IgG and affinity binding of anti-mouse IgG labeled with a chromophore in NIPPAm-based hydrogel.

centration of 40 μg/mL followed by rinsing PBS. As seen in Fig. 4.2, the affinity binding of a-IgG was manifested as a gradual increase in the fluorescence signal in the angular regions where the hydrogel waveguide mode and surface plasmons were resonantly excited. This figure shows a negligible change in the SPR reflectivity. This effect can be explained by the analysis of the angular reflectivity spectrum measured after the affinity binding of a-IgG. As seen in Fig. 4.2a, the binding of a-IgG did not induce a pronounced shift of the SPR dip however the excitation of hydrogel waveguide mode was altered significantly. The analysis of the spectrum revealed that the refractive index was $n_h = 1.353$ was not changed

however the thickness of the hydrogel matrix increased to $d_h = 750$ nm. Based on these results, the surface mass density Γ after the affinity binding of IgG was determined as 75 ng/mm^2. Therefore, the resulting mass density of captured a-IgG of $\Gamma = 8$ ng/mm^2 indicates that approximately one third of IgG molecules was capable to react with affinity partners in the sample. The reason for this observation is probably due to the steric hindrance of the molecular binding within the hydrogel matrix.

Table 4.1: Summary of the characteristics of hydrogel binding matrix prior and after protein conjugation.

Spectrum	buffer	Thickness d_h	n_h	Γ [ng/mm^2]
1	ACT	607	1.349	42
3	PBS	687	1.353	67
4	PBS	750	1.353	75

4.1.3.2 Amplification of the fluorescence signal through hydrogel collaspe

Further, we demonstrate the increase of the fluorescence signal due to molecular binding events by externally triggered collapse of the NIPAAm-based hydrogel binding matrix. In this experiment, the concentration of NaCl in buffer solution flowed over the hydrogel was sequentially increased from 0.1 M to 5 M. As seen in Fig. 4.3a, the SPR dip and critical angle in the reflectivity spectrum shift towards high angles when increasing the concentrations of NaCl. From these spectra, the changes of refractive index of the buffer and the refractive index and thickness of hydrogel were determined. As shown in Fig. 4.4, the hydrogel collapses (thickness d_h decreases and the refractive index n_h increases) when increasing the ionic strength of the buffer due to the osmotic and electrostatic screening effects [90, 91, 92]. By the collapse of the gel, the hydrogel binding matrix is compressed leading to an increase in the concentration of captured analyte within the evanescent field of SPs and subsequent enhancement of the fluorescence signal, see Fig. 4.3b. For the 5M concentration of NaCl in the buffer, the thickness of the gel of $d_h = 240$ closely matches the penetration depth of surface plasmons into the hydrogel (approximately 180 nm). As Fig. 4.4 shows, the dependence of the measured fluorescence signal is inversely proportional to the thickness d_h.

The enhancement of the fluorescence signal in the 5M NaCl solution was increased by the factor of 3.2 with respect to those measured in PBS buffer. In addition the 3.1 fold decrease in the hydrogel film thickness d_h was observed.

(a)

(b)
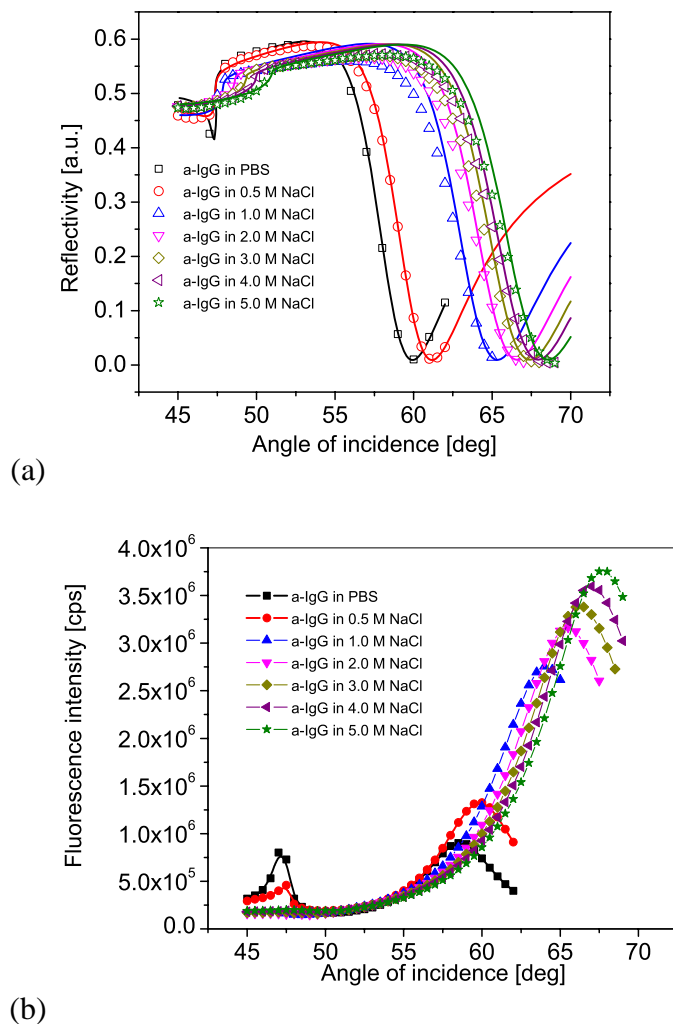
Figure 4.3: Angular spectrum of (a) reflectivity and (b) fluorescence intensity measured for the incubation of a hydrogel matrix with affinity bound a-IgG in buffer solutions with ionic strengths between 0.1 and 5M.

4.1.4 Summary

We demonstrated that a highly swollen responsive NIPAAm-based hydrogel film can serve as an efficient binding matrix in surface plasmon-enhanced fluorescence spectroscopy (SPFS)
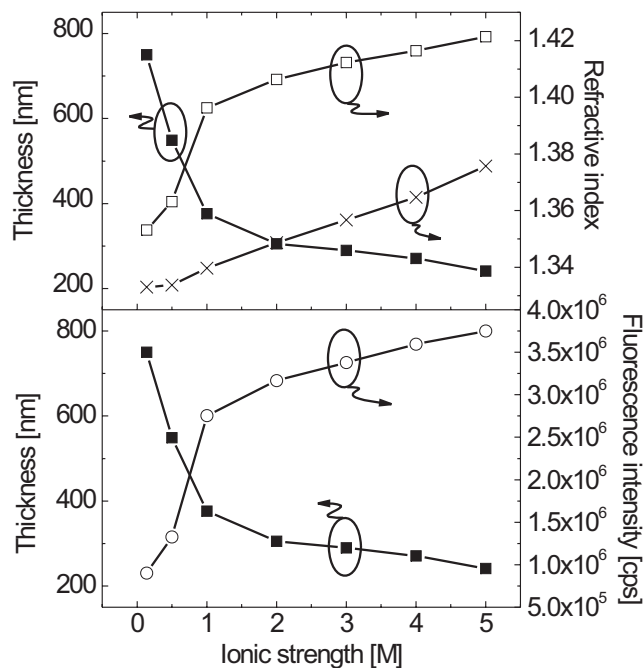
Figure 4.4: The upper panel: The changes of the hydrogel thickness (solid square) and refractive index of hydrogel (hollow square) and buffer (cross) as a function of ionic strength. Lower panel: The dependence of hydrogel thickness (solid square) and maximum fluorescence signal (hollow circle) as a function of ionic strength.

biosensors. In a model experiment, we functionalized the gel with IgG antibodies and observed the affinity binding of antibodies against IgG by SPR and SPFS. Through the measurement of induced refractive index and thickness changes, we determined the ligand surface mass density of 25 ng/mm^2 when IgG molecules were covalently immobilized into a gel with the thickness of approximately 700 nm. In this binding matrix, around 32% of covalently bound IgG molecules reacted with their affinity partners contained in a liquid sample. We showed the enhancement of the SPFS signal by compacting the captured analyte molecules on the sensor surface through a externally triggered collapse of NIPAAm-based hydrogel. In this study, a 3.1 fold decrease in the thickness of the gel resulted in the enhancement of fluorescence intensity with a similar factor.

4.2 LRSP-FS biosensor with hydrogel matrix: on the role of diffusion mass transfer

4.2.1 Motivation

In order to increase the sensitivity of SPR biosensors, three-dimensional binding matrices composed of polymer materials with highly open structure were employed to accommodate large amounts of bimolecular recognition elements on the surface and to reduce the steric hindrance through linking biomolecules to flexible polymer chains. The thickness of a binding matrix grafted to a SPR biosensor surface is adjusted with respect to the size of target analyte molecules and typically does not exceed 100 nm in order to match the penetration depth of surface plasmon field between 100 and 200 nm. The effect of diffusion-limited mass transfer of a target analyte to the SPR sensor surface with dextran brush binding matrix was subject to extensive study in order to enable accurate evaluation of biomolecular interaction analysis (BIA) [93, 94, 95]. However, to the best of our knowledge the dependence of the sensitivity of SPR-based biosensors for detection of molecular analytes on the diffusion mass transfer to and through an extended large binding capacity hydrogel matrix was not yet investigated in detail. This study addresses design of three-dimensional binding matrices in order to reach ultra-low detection limits and it takes into account the concentration and affinity constants of biomolecular recognition elements, thickness of a hydrogel film, mass transfer of target analyte to and through the hydrogel biointerface as well as the spatial profile of probing evanescent wave. In the experimental part of the work, long range surface plasmon (LRSP) field-enhanced fluorescence spectroscopy (LRSP-FS) were used for the detection of fluorophore-labeled analyte molecules captured in a functionalized NIPAAm-based hydrogel binding matrix. Results obtained from a model immunoassay experiment were supported by a theoretical model which described the temporal and spatial evolution of the affinity binding events and analyte diffusion through the functionalized hydrogel film.

4.2.2 Materials and methods

The synthesis of the NIPAAm-based hydrogel was described in Section 2.3.2. Mouse immunoglobulin G (IgG) and goat anti-mouse immunoglobulin G (a-IgG) were purchased from Invitrogen (Camarillo, CA). a-IgG molecules were labeled with Alexa Fluor 647 and the dye-to-protein molar ratio was of 4.9 determined by UV spectrometry.

4.2.2.1 Optical setup and profile of electromagnetic field

For the design of optical setup, we described in detail in Section 2.4 and sketched in Fig. 4.5a. To the sensor surface, there was attached a flow-cell composed of a poly(dimethylsiloxane) gasket and a transparent quartz slide with input and output ports. The depth of the flow cell was $h = 0.3$ mm, length $L = 8$ mm and width $w = 5$ mm. The flow-cell input and output ports were connected to a peristaltic pump with a rubber tubing to flow liquid samples at the flow rate of 500 μL min^{-1}.

As simulations in Fig. 4.5b show, the resonant coupling to LRSP and HOW modes propagating along the sensor surface is accompanied with enhanced electromagnetic field intensity. This field intensity enhancement provided means for efficient excitation of Alexa Fluor-647 chromophores (absorption wavelength close to 633 nm) in vicinity to the surface. Upon the excitation of LRSPs, the electric field intensity exponentially decays into the hydrogel with the penetration depth of $L_p/2 = 460$ nm. The maximum field intensity enhancement of $|E/E_0|^2 = 55$ occurs at the interface between gold and gel (the electric intensity E was normalized with the intensity of incident light beam E_0). The coupling to HOW provides higher field enhancement of $|E/E_0|^2 = 110$ at a distance of 1400 nm from the gold surface.

4.2.2.2 Characterization of hydrogel films

The refractive index n_h and the thickness d_h of swollen hydrogel films and refractive index n_{h-dry} and thickness d_{h-dry} of dry hydrogel films were determined by the spectroscopy of LRSP and HOW modes as described in literature [69]. For gels with sufficiently large thickness, two resonance dips due to the excitation of LRSP and HOW modes can be observed in the angular reflectivity spectrum $R(\theta)$ centered at distinct angles of θ_{LRSP} and θ_{HOW}, respectively. Due to different profiles of electromagnetic field of LRSP and HOW modes (see Fig. 4.5b), hydrogel thickness d_h and refractive index n_h can be independently determined by the analysis of reflectivity spectrum $R(\theta)$. The measured reflectivity spectra $R(\theta)$ were fitted by a model based on Fresnel equations and transfer matrix formalism [70] that was implemented in the software Winspall. All parameters of the layer structure except n_h and d_h were fixed at values that were determined by other methods or taken from literature [89, 96]. These include the refractive index of the LASFN9 glass $n_p = 1.845$, the thickness $d_b = 715$ nm and refractive index $n_b = 1.337$ of Cytop layer, the thickness $d_m = 13.2$ nm and refractive index $n_m = 0.269 + 2.58i$ of gold film, the thickness $d_t = 2$ nm and refractive index $n_t = 1.5$ of benzophenone thiol SAM and the refractive index of buffer $n_s = 1.333$. In

(a)

(b)
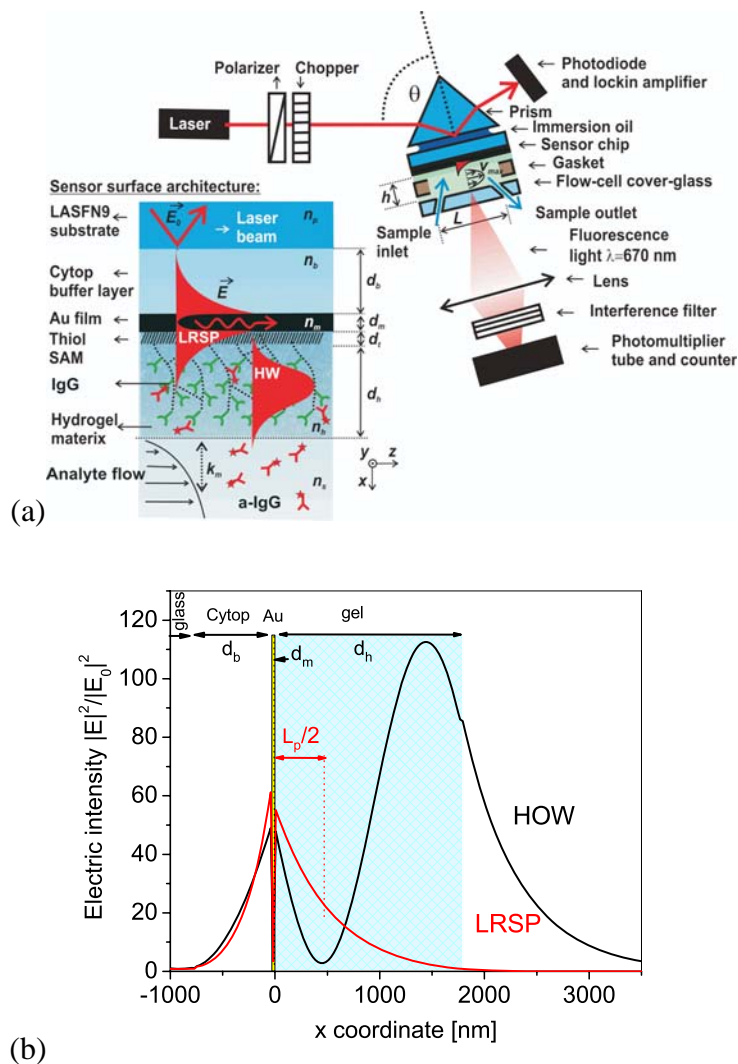
Figure 4.5: (a) Setup for the angular spectroscopy of LRSP and HOW modes with a fluorescence spectroscopy module and a scheme of LRSP-supporting layer structure with NIPAAm-based hydrogel binding matrix. (b) Simulated electric intensity profile upon the resonant excitation of LRSP (at the angle of incidence of θ_{LRSP}) and HOW (at the angle of incidence of θ_{HOW}) modes in the the hydrogel with a thickness of $d_h = 1.8$ μm and the refractive index of $n_h = 1.345$.

the fitting of angular reflectivity spectra $R(\theta)$, we assumed that the hydrogel refractive index n_h is constant perpendicular to the surface ("box mode"). The gel surface mass density was calculated as $\Gamma = (n_h - n_b)d_h\partial c/\partial n_h$, where the factor of $\partial c/\partial n_h = 0.185$ mm^3 mg^{-1} was used [97]. Based on the effective medium theory, the polymer volume fraction f of the

swollen hydrogel was determined as:

$$f = \frac{n_h^2 - n_s^2}{n_h^2 + 2n_s^2} \frac{n_{h-dry}^2 + 2n_s^2}{n_{n-dry}^2 - n_s^2}.$$

(4.1)

4.2.2.3 Molecular interactions in a 3D matrix layer

When a three-dimensional matrix is employed for the immobilization of BREs, the binding kinetics measured with SPR biosensors deponds on the diffusion of analytes through the matrix. In this thesis, a numerical model was established based on Schuck's works [94] for the evaluation of affinity binding constants by using SPR biosensor technology with a thin dextran brush binding matrix [95, 93]. In this model, we take the same 1:1 Langmuir model as Eq. 1.32. We assumed that biomolecular recognition elements B are distributed homogeneously in the gel with a concentration β and their interaction with analyte molecules A was described by the association and dissociation affinity rate constants k_a and k_d, respectively. A flow-channel geometry is depicted in Fig. 4.6 and it is described by using Cartesian coordinates with axis x perpendicular to the surface and axis z parallel to the sample flow. Laminar flow of a sample through the flow-cell is assumed which holds for the geometries with Reynolds number $Re < 2100$. In contrast to the 2D binding system, the concentration of the complex γ not only change with time t but also with the thickness of hydrogel d. Thus, we need an equation to describe the diffusion of analyte A through the gel that is depleted due to the reaction with unoccupied catcher molecules for solving the time and spatial dependence of the AB complex concentration $\gamma(x,t)$ as:

$$\frac{\partial \alpha}{\partial t} = D_g \frac{\partial^2 \alpha}{\partial x^2} - \frac{\partial \gamma}{\partial t},$$

(4.2)

where D_g is the analyte diffusion coefficient in the gel. In addition, the reaction of molecules A and B is expressed as:

$$\frac{\partial \gamma}{\partial t} = k_a \alpha (\beta - \gamma) - k_d \gamma.$$

(4.3)

In order to solve the set of partial differential equation (PDE) from Eq. 4.2 and 4.3, the initial and boundary conditions are applied as:

$$\alpha(x, t = 0) = 0,$$

(4.4)

$$\gamma(x, t = 0) = 0,$$

(4.5)

$$\frac{\partial \alpha}{\partial x}(x, t = 0) = 0,$$

(4.6)

$$\frac{\partial \alpha}{\partial x}(x = 0, t) = 0, \tag{4.7}$$

$$\frac{\partial \alpha}{\partial x}(x = d, t) = \frac{k_m}{D_g}\left[\alpha_0 - \alpha(d, t)\right], \tag{4.8}$$

where α_0 is the concentration of molecule A in the bulk solution, k_m is the diffusion rate of molecule A to the surface of the gel. Eq. 4.4 and 4.5 define the zero concentration of free α and captured γ analyte at $t = 0$, respectively. Eq. 4.6 ensures the absence sources of the analyte α in the gel at time $t = 0$, Eq. 4.7 defines the analyte flux through the inner hydrogel interface (i.e. analyte cannot pass through the solid support on which gel is attached) and Eq. 4.8 describes that the analyte flux through the outer interface (with the sample) is driven by the mass diffusion rate k_m.

With initial and boundary conditions (Eqs. 4.4- 4.8), the set of PDE of Eqs. 4.2 and 4.3 can be solved for studying the spatial and time profiles of the analyte captured in the gel.
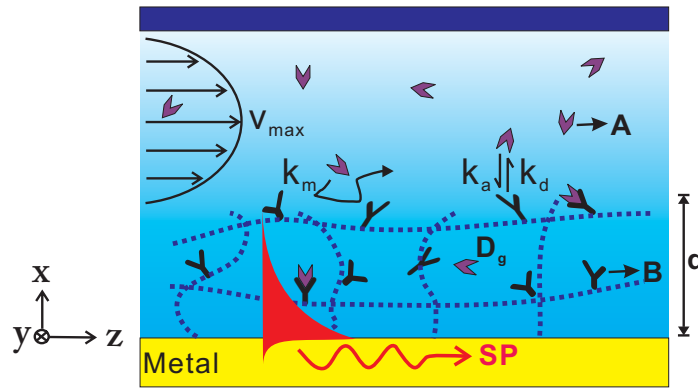
Figure 4.6: Mass transport and molecular interactions in matrix layer.

4.2.2.4 Modeling of diffusion and affinity binding in the hydrogel matrix

A numerical model was adopted for the simulation of affinity binding of analyte and diffusion mass transfer based on the theory which was introduced to SPR biosensors with dextran binding matrix [94]. A set of partial differential equations describing the mass transfer of an-alyte from a liquid sample (flowed in a flow-cell) to the hydrogel surface, diffusion of analyte through the hydrogel and its affinity binding to biomolecular recognition elements was nu-merically solved as described in last Subsection 4.2.2.3. By using this model, we calculated the temporal and spatial dependence of the concentration of free $\alpha(x, t)$ and captured $\gamma(x, t)$ analyte in the gel (where x axis is perpendicular to the surface, see Cartesian coordinates in Fig. 4.5a). Laminar flow of a sample through the flow-cell was assumed and the dependence

of the concentration of free α and captured γ analyte on y and z axis (parallel to the sensor surface) was neglected. These approximations are valid as Reynolds and Peclet numbers were equal to $Re = 28$ and $Pe = 3100$, respectively. Mass transfer of analyte molecules to the sensor surface was taken into account by using two compartment model [93]. The diffusion rate k_m of analyte molecules from an aqueous sample flowed through the flow-cell to the sensor surface was described as:

$$k_m = 1.378 \left(\frac{v_{max} D_s^2}{hL} \right)^{1/3},$$ (4.9)

where D_s is the diffusion coefficient in the bulk solution and $v_{max} = 1.5 \upsilon/(hw)$ is the flow velocity in the center of the flow-cell. For the used volumetric flow rate υ, flow-cell geometry (specified in Subsection 4.2.2) and the diffusion constant of IgG molecules in aqueous environment of $D_s = 3 \times 10^{-5}$ mm^2 s^{-1} [98], the analyte molecules diffuse to the sensor surface with the diffusion rate of $k_m = 2 \times 10^{-3}$ mm s^{-1}. The simulated sensor signal F_{sim} corresponding to the intensity of the fluorescence light F was assumed to be proportional to the overlap between the concentration of captured molecules $\gamma(x,t)$ and the profile of the field intensity $|E(x)|^2$ of LRSP or HOW modes:

$$F_{sim} \propto \int_0^{d_h} \left| \frac{E(x)}{E_0} \right|^2 \gamma(x,t) dx.$$ (4.10)

Fluorescence quenching due to the Förster energy transfer in the close proximity to the metal surface was omitted in the model as the hydrogel thickness d_h was typically much larger than the distances up to $\sim$15 nm for which the quenching occurs. In addition, the angular distribution of fluorescence emission that is altered through the interaction of fluorophores with the surface waves [33] was not taken into account.

4.2.3 Results and discussion

4.2.3.1 Characteristics of hydrogel films

LRSP-supporting substrates were coated by NIPAAm-based hydrogel layer with a thickness between $d_{h-dry} = 8$ nm and 200 nm in the dry state. These gels were swollen in PBST buffer and characterized *in situ* by the spectroscopy of LRSP and HOW modes. Fig. 4.7a shows the angular reflectivity spectra $R(\theta)$ measured for the hydrogel films with a thickness of $d_{h-dry} =$0, 7.4, 82 to 198 nm. The measured reflectivity curves were fitted by Fresnel reflectivity-based model in order to determine hydrogel thickness d_h and refractive index n_h

in swollen state. For thicknesses d_{h-dry} >100 nm, two resonance dips can be observed due to the excitation of LRSP and HOW modes in the swollen gel. Owing to the different profiles of electromagnetic field of LRSP and HOW modes (see Fig. 4.5b), both n_h and d_h can be determined for these films. For the thickness d_{h-dry} <100 nm, the swollen hydrogel film does not support HOW and therefore only one of these two parameters can be determined. For such thin gel films, the refractive index n_h was fixed at the value determined for the thicker films and the thickness d_h was determined by fitting the LRSP reflectivity dip in the spectrum $R(\theta)$. The obtained results revealed that the thickness of the gel increased after its swelling by a factor of $d_h/d_{h-dry} = 10.2 \pm 1$ (standard deviation - SD). The refractive index of the hydrogel film changed upon the swelling in PBST from $n_{h-dry} = 1.503$ in the dry state to $n_h = 1.345 \pm 0.002$ (SD) in the swollen state. This change corresponds to the polymer content in the swollen gel of $f = 7.3 \pm 2.4\%$ (SD). Prior to the affinity binding studies, hydrogel films were modified with IgG molecules by using the protocol described in Subsection 2.3.2. Fig. 4.7b shows measured angular reflectivity spectra $R(\theta)$ for a gel with the thickness $d_h = 1800$ nm before and after the immobilization of IgG. One can see that the LRSP dip shifted from $\theta_{LRSP} = 48.67$ deg to 48.95 deg and HOW mode dip moved from $\theta_{HOW} = 47.63$ deg to 47.60 deg. The fitting of reflectivity spectra revealed that the gel surface mass density Γ increased by $15 \pm 4\%$ (SD) due to the coupling of IgG. In addition, gel thickness d_h decreased by $20 \pm 2\%$ (SD) which is probably due to a lower charge density associated with the converting of negatively charged carboxylic moieties to IgG and neutral ethanolamine groups. The concentration of IgG catcher molecules in the hydrogel β was determined as the increase of the surface mass density Γ divided by the thickness of the gel d_h. The IgG concentration in the gel of $\beta = 16 \pm 4$ mg mL^{-1} (SD) was obtained, which corresponds to $\beta = 9 \times 10^{-4} \pm 2.4 \times 10^{-4}$ M for the molecular weight of IgG of 160 kDa. Let us note that for the hydrogel in swollen state with $d_h = 1440$ nm, the surface mass density of the immobilized IgG was 16 ng mm^{-2} which corresponds to about four densely packed monolayers (based on the surface mass density of 4 ng mm^{-2} per monolayer reported by [99]).

4.2.3.2 Kinetics of affinity binding in the hydrogel matrix

LRSP evanescent wave was excited in order to probe the affinity binding of a-IgG contained in a liquid sample to IgG molecules immobilized in the NIPAAm-based gel. The dependence of the intensity of the binding-induced fluorescence signal F on a) the hydrogel thickness d_h and b) on the spatial profile of the probing evanescent wave was investigated. LRSPs

(a)

(b)
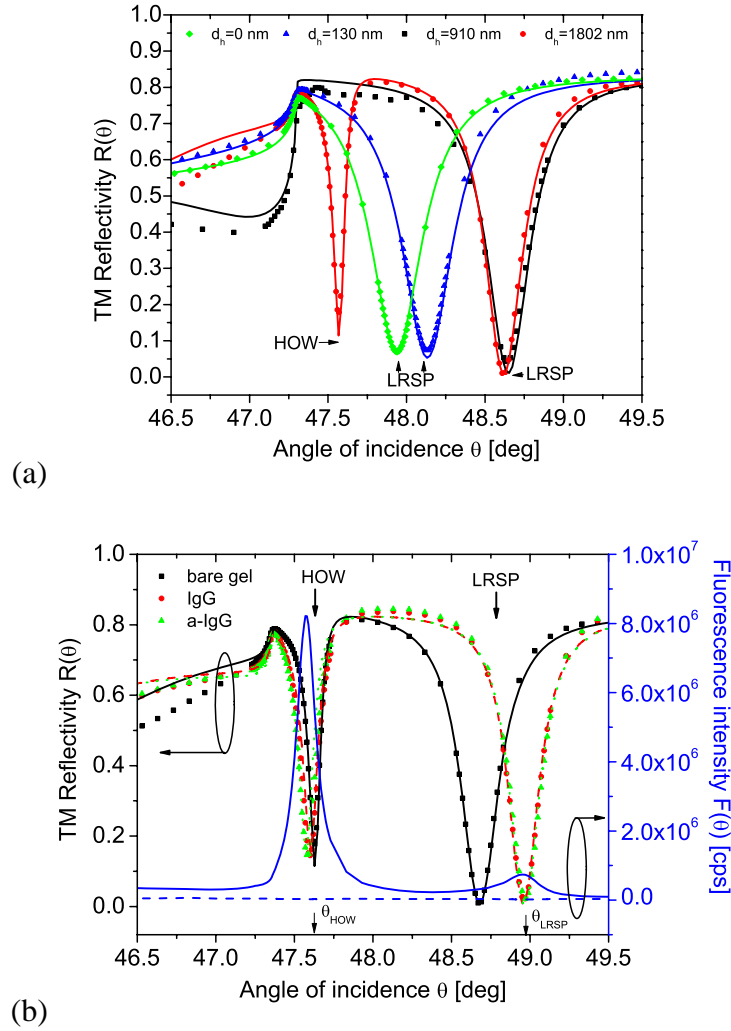
Figure 4.7: (a) Angular reflectivity spectra $R(\theta)$ measured for hydrogel films swollen in PBST with the thickness of $d_h = 0$ nm (solid diamond), 160 (solid triangle), 910 nm (solid square), and 1800 nm (solid circle) and refractive index $n_h = 1.345$ as determined by fitting with a Fresnel equations-based model (lines). (b) Angular reflectivity spectra $R(\theta)$ for hydrogel with the thickness $d_h = 1800$ nm (solid square) that is swollen in PBST, after its modification with IgG (solid circle) and after the affinity binding of a-IgG labeled with Alexa Fluor-647 (solid triangle) flowed at the concentration of $\alpha_0 = 6.7$ nM for $\Delta t = 30$ min. The measured reflectivity curves were fitted with Fresnel equations-based model (lines). Fluorescence angular spectrum $F(\theta)$ before (dotted line) and after (solid line) the capture of a-IgG labeled with Alexa Fluor 647.

with the maximum field intensity at the inner interface of the hydrogel were employed for the observation of hydrogel binding matrices with a thickness between $d_h = 64$ and 1440 nm

(measured after the coupling of IgG). The capture of a-IgG analyte molecules labeled with Alexa Fluor 647 chromophores is manifested as an increase in the fluorescence intensity F. Fig. 4.7b illustrates that after the capture of a-IgG molecules in the gel with the thickness of $d_h = 1400$ nm, the angular fluorescence spectrum $F(\theta)$ exhibits two strong fluorescence peaks located at the angles $\theta_{LRSP} = 48.95$ deg and $\theta_{HOW} = 47.60$ deg at which the LRSP and HOW modes are excited, respectively.

The fluorescence sensor signal $F(t)$ was measured upon a successive flow of series of samples with increasing concentration of a-IgG α_0. After a baseline was established, each sample was flowed for $\Delta t = 30$ min across the hydrogel surface followed by 10 min rinsing with a PBST buffer. As Fig. 4.8 shows, the affinity binding of a-IgG molecules into the gel is manifested as a gradual increase in the fluorescence signal F. During the rinsing with PBST, a decrease of the signal F occurs due to the dissociation of a-IgG and IgG pairs. For low analyte concentrations α_0 between 6.7 fM to 6.7 pM, the fluorescence signal $F(t)$ linearly increases in time with the slope dF/dt that is proportional to the concentration α_0. For the concentrations α_0 between 6.7 nM to $1.3 \ \mu$M (see the inset of Fig. 4.8), the fluorescence signal $F(t)$ become saturated for the hydrogel matrices with $d_h < 1 \ \mu$m.

Prior to the simulation of the diffusion mass transfer of analyte in the hydrogel binding matrix probing with LRSPs, the association and dissociation rate constants of the IgG and a-IgG pair has to be determined and the surface plasmon-enhanced fluorescence biosensor was employed. This method was shown to provide identical affinity binding constants as regular SPR [100]. A surface architecture based on thiol self assembled monolayer (SAM) was used for the immobilization of ligand molecules on the surface through the procedure in previous Subsection 2.3.1. Low IgG surface coverage of 0.44 ng mm^{-2} (corresponds to $\beta = 3 \times 10^{-15}$ mol mm^{-2}) was used in order to assure that the binding is not diffusion limited ($k_a\beta/k_m$ of ~ 0.07). The time dependence of the fluorescence signal $F(t)$ that is proportional to the amount of a-IgG molecules adhered to the surface was recorded (see Fig. 4.9). In the association phase, a-IgG molecules dissolved in the PBST buffer at concentrations of 0.07, 0.67 and 6.7 nM were flowed over the sensor surface with IgG molecules. The binding of analyte to ligands was observed as a gradual increase in the fluorescence signal F (association phase). Afterwards, a gradual decrease in the fluorescence signal was observed upon a rinsing PBST owing to the disruption of a-IgG and IgG pairs (dissociation phase). Corresponding injection times are indicated in the Fig. 4.9. The measured association and dissociation kinetics $F(t)$ were fitted by using 1:1 Langmuir adsorption model in order to determine the association and dissociation affinity rate constants k_a and k_d, respec-
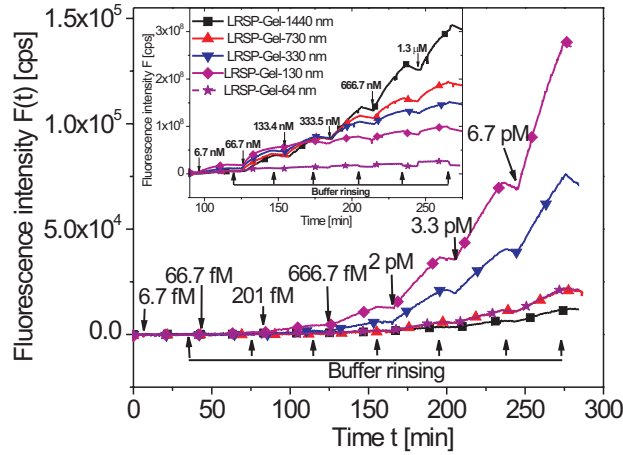
Figure 4.8: The binding kinetics observed from the fluorescence signal $F(t)$ that was measured upon the successive flow of samples with a-IgG molecules (labeled with Alexa Fluor-647) at concentrations increasing from $\alpha_0 = 6.7$ fM to 1.3 μM. IgG-functionalized hydrogel binding matrices with the thickness of $d_h = 64$ (cross), 130 (solid diamond), 330 (solid circle), 730 (solid triangle) and 1440 nm (solid square) were probed by LRSP mode. Injection times for each sample with a-IgG molecules and rinsing of the sensor surface with buffer are clearly indicated.

tively, as described in literature [94]. For the used IgG and a-IgG pair, the association and dissociation rate constants were evaluated as $k_a = 6.48 \times 10^4 \pm 0.05 \pm 10^4$ M^{-1} s^{-1} and $k_d = 4.46 \times 10^{-5} \pm 0.03 \pm 10^{-5}$ s^{-1}, respectively (the errors represent SD).

For the probing hydrogel binidng matrix with LRSP, the fluorescence light intensities F measured after the binding of a-IgG molecules from a sample with high ($\alpha_0 = 1.3 \mu$ M) and low ($\alpha_0 = 0.67$ pM) concentrations of a-IgG were compared with simulations. In these simulations, we used association and dissociation rate constants as determined above. From data presented in Fig. 4.10a follows that after the binding of analyte from a sample with large concentration $\alpha_0 = 1.3 \mu$M the measured fluorescence intensity F increases with the hydrogel thickness d_h. The simulation curves exhibit a similar trend and reach a plateau for a thickness larger than the penetration depth $L_p/2 = 460$ nm. The simulated curves depend weakly on the analyte diffusion coefficient in the gel between $D_g = 3 \times 10^{-7}$ and 3×10^{-5} mm^2 s^{-1}. For of about six orders of magnitude lower analyte concentration $\alpha_0 = 0.67$ pM, the measured fluorescence signal F is approximately five orders of magnitude smaller and its thickness dependence exhibits different behavior, see Fig. 4.10b. A max-
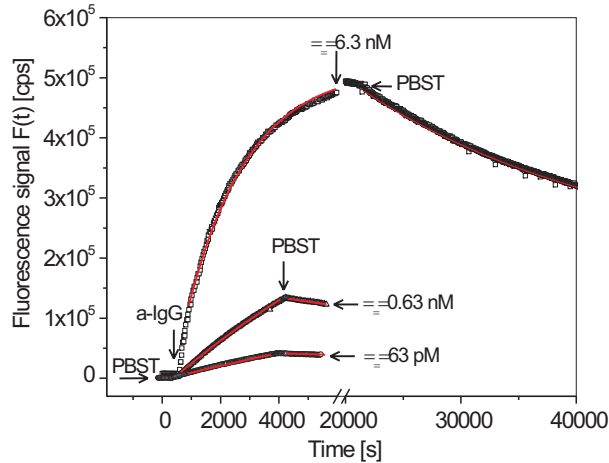
Figure 4.9: Association and dissociation kinetics of the affinity binding of a-IgG from a PBST at the concentration of 0.067 (solid circle), 0.67 (solid triangle) and 6.7 (solid square) nM to the IgG molecules immobilized on the sensor surface. The curves were fitted with the Langmuir adsorption isotherm model (lines). Injection times of samples and rinsing with a buffer are clearly indicated in the graph.

imum fluorescence signal F was measured for the hydrogel thickness between d_h = 130 and 410 nm and it sharply decreases when increasing the thickness above these values. The hydrogel thickness for which the simulations predict the maximum fluorescence signal is shifting with the diffusion coefficient in the gel from $d_h = 300$ nm for D_g=3×10^{-7} mm^2 s^{-1} to d_h = 580 nm for $D_g = 3 \times 10^{-5}$ mm^2 s^{-1}. The comparison of experimental dependence of fluorescence signal F on the hydrogel thickness d_h presented in Fig. 4.10b indicates that the diffusion coefficient of a-IgG molecules in the gel D_g was more than order of magnitude lower than that in the aqueous sample D_s. This observation agrees with the results obtained by fluorescence correlation spectroscopy for proteins diffusing to NIPAAm-based hydrogel [101].

4.2.3.3 The spatial distribution of captured analyte

In order to elucidate the observations presented in Subsection 4.2.3.2, the spatial distribution of captured analyte $\gamma(x)$ was calculated by using a numerical model. The simulations predict that after a 30 minute flow of a sample with large concentration of α = 1.3 μM, the hydrogel binding matrix becomes saturated and $\gamma \approx \beta$ in the whole gel. Therefore, the fluorescence signal F depends weakly on the diffusion of the analyte through the gel and it

(a)

(b)
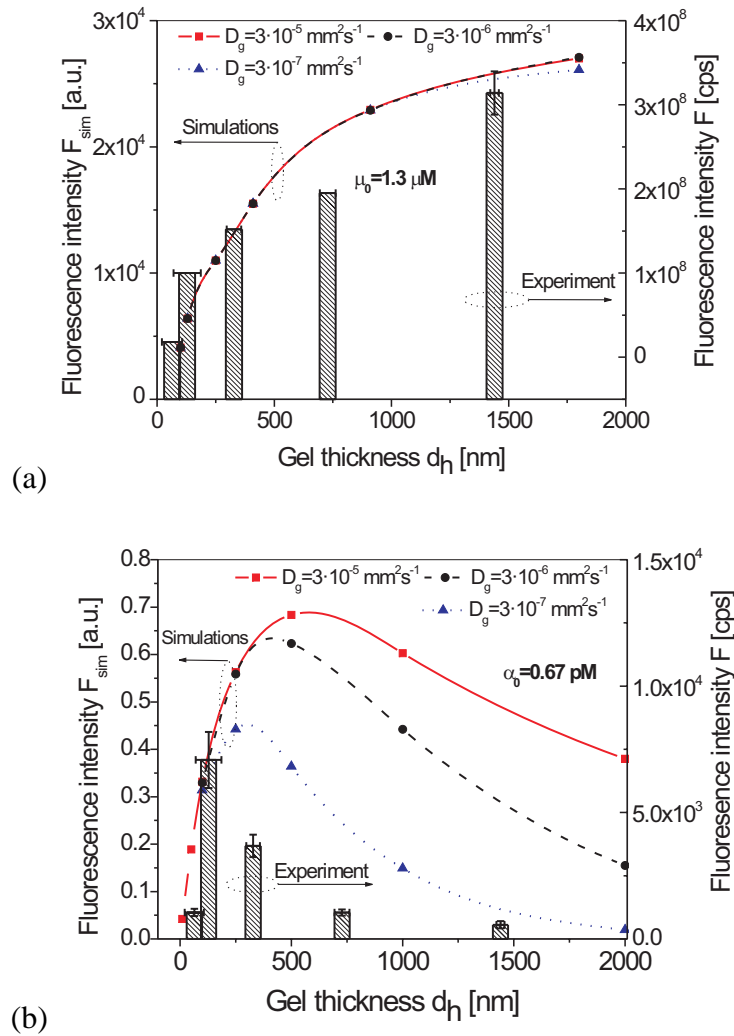
Figure 4.10: The comparison of simulated (left axis) and measured (right axis) dependence of the fluorescence signal F on thickness of the hydrogel binding matrix d_h. The hydrogel matrix was probed by LRSP mode the fluorescence signal after the 30 minute flow of a-IgG dissolved at (a) low concentration of $\alpha_0 = 0.67$ pM and (b) high concentration of α_0 = 1.3 μM. Diffusion coefficient in the gel of $D_g = 3 \times 10^{-5}$ mm^2 s^{-1} (red, square), $D_g = 3 \times 10^{-6}$ mm^2 s^{-1} (black circle) and $D_g = 3 \times 10^{-7}$ $mm^2 s^{-1}$ (blue triangle) was assumed. The errors bar of measured fluorescence signal F represent standard deviation obtained from a triplicate measurement (three prepared sensor chips).

increases with the number of biomolecular recognition elements within the LRSP evanescent field. The maximum fluorescence signal is achieved for thicknesses d_h that exceeds the LRSP penetration depth $L_p/2 = 460$ nm. For the analyte concentrations α_0 below pM level,

the simulations reveal that concentration of the captured analyte is much smaller than that of biomolecular recognition elements $\gamma \ll \beta$. In such gel, the analyte molecules diffusing from a sample into the the gel become captured within a charateristic time t_a and thus can diffuse only to a limited distance from the outer gel interface. The average diffusion time can be shown to be $t_a = \ln(2)/(k_a\beta)$ which corresponds to the following diffusion depth d_p derived by using Fick's law:

$$d_p = \sqrt{\frac{4D_g \ln(2)}{k_a\beta}}. \tag{4.11}$$

The numerical simulations shown in Fig. 4.11 confirm that the binding events preferably occur within an outer hydrogel slice with the thickness d_p. For example, the diffusion penetration depth reaches d_p = 380 nm for the diffusion coefficient of $D_g = 3\times10^{-7}$ mm^2 s^{-1} and increases to d_p = 1.2 μm for $D_g = 3\times10^{-6}$ mm^2 s^{-1}. These data illustrate that a more homogeneous distribution of $\gamma(x)$ is established in gel with small thickness d_h or for large diffusion coefficients D_g. Let us note that as far as $\gamma \ll \beta$, the established profile of captured analyte does not change in time and the amount of bound analyte is proportional to the flow time $\gamma(x,t) \propto \gamma(x)\Delta t\alpha_0$.

The comparison of the spatial distribution $\gamma(x,t)$ with the profile of the electromagnetic field of LRSP mode probing the hydrogel biointerface is also presented in Fig. 4.11. It indicates that LRSP with exponentially decaying field from the inner gel interface is suitable for probing of gels with the thickness d_h that is comparable with the LRSP penetration depth $L_p/2$ and the analyte diffusion depth d_p. For a binding matrix with larger thickness $d_h > L_p/2$ and $d_h > d_p$, the majority of the binding events occurs in the volume outside the LRSP field and thus does not contribute to the sensor signal F.

Finally, we discuss the effect of mass transfer of the analyte to the surface that was taken into account by using the diffusion rate k_m. When the condition $k_a\beta d_h \gg k_m$ (for large analyte diffusion depth $d_p > d_h$) or $k_a\beta d_p \gg k_m$ (for large hydrogel thickness $d_h > d_p$) holds, the binding of target molecules to the surface is strongly diffusion limited (let us note, that these conditions relates to Damköhler number [93] that can be expressed as $Da \sim d_{h,p}\beta k_a/k_m$ for the herein studied architecture). This effect is illustrated in Fig. 4.11 which shows the dependence of the concentration of captured analyte molecules $\gamma(x,t)$ for the hydrogel thickness d_h = 1440 nm. When increasing the diffusion coefficient from $D_g = 3\times10^{-7}$ mm^2 s^{-1} to $D_g = 3\times10^{-6}$ mm^2 s^{-1}, one can see that the binding of the analyte occurs deeper in the gel but the maximum concentration of $\gamma(x)$ is decreased due to the finite diffusion rate k_m. Therefore, increasing the thickness of the hydrogel d_h or diffusion
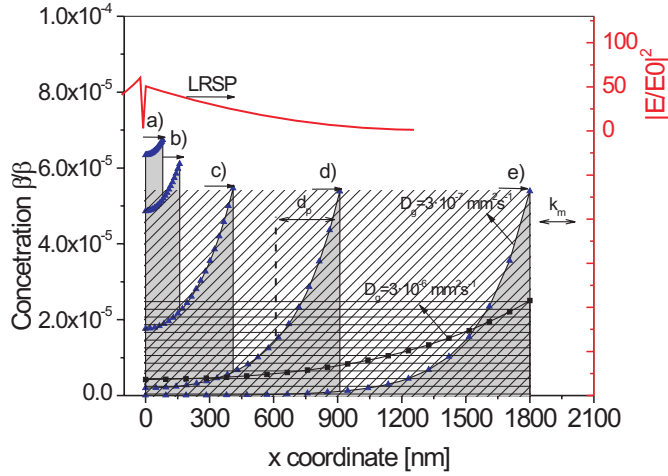
Figure 4.11: The comparison of spatial distribution of captured analyte $\gamma(x)$ for the hydrogel thickness of (a) $d_h = 64$ nm, (b) $d_h = 130$ nm, (c) $d_h = 330$ nm, (d) $d_h = 730$ nm and (e) $d_h = 1440$ nm. In these simulations, the $\gamma(x)$ were calculated for the binding of analyte with concentration of $\alpha_0 = 0.67$ pM in a sample for 30 min and diffusion coefficient in the gel of $D_g = 3 \times 10^{-7}$ mm^2 s^{-1} was assumed. In addition, $\gamma(x)$ for diffusion coefficient of $D_g = 3 \times 10^{-6}$ mm^2 s^{-1} (black square) and $D_g = 3 \times 10^{-7}$ mm^2 s^{-1} (blue triangle) is shown for the hydrogel thickness of $d_h = 1800$ nm. The profiles of electric intensity field of LRSP mode is presented in the upper part of the graph.

penetration depth d_p such that surface mass density of catcher molecules within the whole gel $d_h\beta$ or within the analyte diffusion depth $d_p\beta$ is much larger than k_m/k_a will not lead to an enhanced amount of captured analyte and thus will not provide higher sensor response F. For the investigated architecture, the thickness of the hydrogel providing binding capacity that is sufficient for the efficient capture of target analyte diffusing to the sensor surface with the rate $k_m = 2 \times 10^{-3}$ mm s^{-1} is of $k_m/k_a\beta = 345$ nm which is consistent with the experimental data and numerical simulations presented in Fig. 4.10b.

4.2.4 Summary

In this work, a high capacity hydrogel binding matrix for evanescent wave affinity biosensors was experimentally and theoretically investigated. The results show that for detection of target analyte with maximum sensitivity, a delicate design of three-dimensional hydrogel binding matrix needs to be carried out. Particularly, the interplay of parameters including the profile of a probing wave, diffusion characteristics of an analyte to and through a gel, overall

binding capacity and affinity rate constants k_a and k_d have to be taken to account. The presented data indicate that large binding capacity schemes would be particularly beneficial for biosensing with lower-affinity biomolecular recognition elements or small molecules that diffuse fast from sample to the sensor surface and through the hydrogel binding matrix.

4.3 Label-free immunoassay-based biosensor exploiting hydrogel optical waveguide spectroscopy

4.3.1 Motivation

Among various technologies, optical biosensors allowing direct detection of target analytes without the need of additional labels are pushed forward for the applications in areas such as medical diagnostics, food control and environmental monitoring [14, 102, 103]. Recently, carboxylated photocrosslinkable hydrogel polymer networks based on NIPAAm and dextran copolymers were synthesized in our laboratory for high capacity binding matrices in surface plasmon resonance (SPR) and surface plasmon-enhanced fluorescence spectroscopy (SPFS) biosensors [60, 69, 104, 105]. If attached to a metallic surface, these films can serve as optical waveguides which exhibit more than an order of magnitude lower damping than surface plasmons [60, 69, 106]. In this section, we show that the hydrogel optical waveguide spectroscopy (HOWS) allows monitoring the variations of refractive index on the sensor surface with greatly increased accuracy compared to regular SPR. Moreover, a thin hydrogel film can serve both as a waveguide and as an affinity binding matrix and thus it provides full overlap of the electromagnetic field of a probing wave with the region where molecular binding events occur. The performance of HOWS is characterized by means of a refractometric study and its implementation for label-free biosensing is demonstrated through a model immunoassay experiment. The obtained results are compared to those measured by regular SPR biosensor relying on thiol SAM surface architecture. This work was done in collaboration with Yi Wang (AIT), Dr. Ulrich Jonas (RORTH/IESL) and Prof. Tianxin Wei (Beijing Institute of Technology).

4.3.2 Materials and methods

The chemicals and biomaterials used in this section are the same as in Sections 4.1 and 4.2 for the model system of immunoassay, i.e. the pair of mouse IgG and anti-mouse IgG.

For the detection of Human Chorionic Gonadotropin beta subunit (β-hCG), the free β-hCG analyte, detection IgG (cat. no. MAF05-043) and capture IgG (cat. no. MAF05-627) were supplied from Meridian (Saco, ME).

4.3.2.1 Spectroscopy of hydrogel waveguide modes

The HOWS biosensor was implemented by using an optical setup same as that used for SPR, see Section 2.4. The evanescent field of a laser beam that is totally internally reflected at the sensor surface penetrates through the gold layer and can couple to surface plasmon (SP) and hydrogel waveguide (HW) modes propagating along the outer metal interface. As Fig. 4.12 shows, the excitation of SP and HW modes is manifested as two distinct dips in the angular reflectivity spectrum. These dips are located at angles θ for which the propagation constant of the mode β matches the component of the reflected laser beam propagation constant that is parallel to the interface:

$$k_0 n_p \sin(\theta) = Re\beta, \tag{4.12}$$

where $k_0 = 2\pi/\lambda$ is the light propagation constant in vacuum. The propagation constant β_{HW} can be determined from the analytical dispersion relation:

$$\tan(\kappa d_h) = \frac{\gamma_b n_h^2/\kappa n_b^2 + \gamma_m n_h^2/\kappa n_m^2}{1 - (\gamma_b n_h^2/\kappa n_b^2)(\gamma_m n_h^2/\kappa n_m^2)}, \tag{4.13}$$

in which n_m is the refractive index of the metal, n_b is the refractive index of the analyzed dielectric medium (air or buffer) and $\kappa^2 = (k_0^2 n_h^2 - \beta^2)$, $\gamma_m^2 = \beta^2 - k_0^2 n_m^2$ and $\gamma_b^2 = \beta^2 - k_0^2 n_b^2$ are the transverse propagation constants in the hydrogel film, the metal and the analyzed medium, respectively. Further, the resonance coupling angle for HW mode is noted as θ_{HW} and the one for surface plasmons as θ_{SP}. Both coupling angles increase when increasing the refracting index of the dielectric adjacent to the gold surface n_h. In the further time resolved experiments, the angle of incidence θ was set to the location with highest slope $\partial R/\partial\theta$ at the edge of the HW or SP reflectivity dip below the resonant angles θ_{HW} and θ_{SP}, respectively. A shift in the resonant dips due to the refractive index variations δn_h was measured from induced changes in the reflected intensity δR. In order to determine the thickness d_h and the refractive index n_h of the hydrogel film binding matrix, the angular reflectivity spectrum exhibiting SP and HW resonance dips was fitted by transfer matrix-based model. Similar to our previous investigation in Section Sec:responsive, we assumed a constant refractive index of the gel n_h perpendicular to the surface from which the gel

surface mass density was calculated as $\Gamma = (n_h - n_b)d_h\partial c/\partial n_h$, where n_b is the refractive index of buffer and d_h is the thickness of hydrogel. The refractive index of the hydrogel layer was assumed to change with the concentration of the captured protein molecules and with the NIPAAm polymer chains as $\partial n_h/\partial c = 0.2$ mm^3 mg^{-1}.
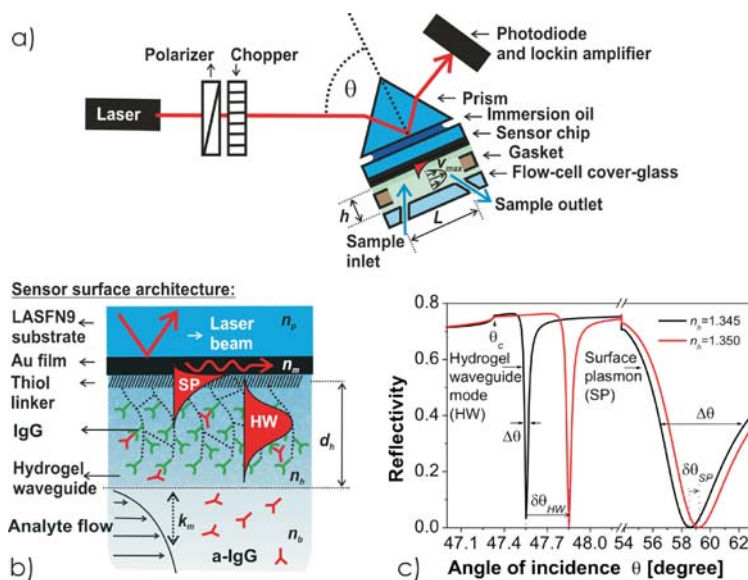
Figure 4.12: (a) Optical setup for the excitation of hydrogel waveguide (HW) and surface plasmon (SP) modes, (b) scheme of the sensor surface architecture and (c) simulated changes in the angular reflectivity spectra for the resonant excitation HW and SP modes due to the refractive index increase $\Delta n_h = 5\times10^{-3}$ for a hydrogel film with the thickness $d_h = 1.7$ μm and refractive index $n_h = 1.345$.

4.3.3 Results and discussion

4.3.3.1 Characterization of hydrogel thin film

Firstly, a hydrogel film attached to the gold surface was characterized by the spectroscopy of HW and SP modes. The angular reflectivity spectra R(θ) were measured for a hydrogel film in contact with air and after its swelling in PBS, see Fig. 4.13. By fitting the two distinct resonances at θ_{HW} = 21.9 deg and θ_{SP} = 76 deg that are associated with the excitation of HW and SP modes in a dry polymer layer, respectively, its thickness d_h = 230 nm and refractive index n_{h-dry} = 1.48 was determined. After the swelling in PBS buffer, the HW and SP coupling angles shifted to θ_{HW} = 47.75 deg and θ_{SP} = 58.20 deg, respectively. The fitting of corresponding reflectivity spectrum revealed that the thickness of the swollen gel

increased to d_h = 1.86 μm and the refractive index decreased to n_h = 1.3454. This refractive index is very close to that of the PBS buffer n_b = 1.3340 and it corresponds to the polymer volume fraction of 8% and swelling ratio 12.5 as estimated by using the effective medium theory [107]. Let us note that for the HOWS the thickness of the hydrogel film needs to be higher than so called cut-off thickness (typically d_h > 1 μm) below which the hydrogel waveguide modes cease to exist.
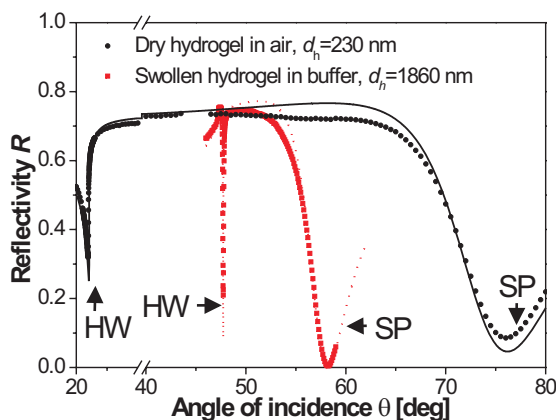
Figure 4.13: Angular reflectivity spectra measured for the hydrogel film in contact with air (black circles) and swollen in PBS (red squares). The spectra were fitted with transfer matrix-based model as indicated by lines.

4.3.3.2 Refractometric study of HOWS sensor

A refractometric study was performed in order to compare the accuracy with which the refractive index changes on the sensor surface can be measured by HOWS and SPR. In this experiment, changes in the reflectivity spectra were measured upon flowing a series of liquid samples with increasing n_b. These samples were prepared by spiking the PBS buffer (n_b = 1.3334) with ethylene glycol (EG, refractive index n = 1.4314) at concentrations between 0 and 8% (refractive index changes linear with the concentration of EG with the slope δn_b = 9.8$\times$10^{-4} RIU per % at the wavelength λ = 633 nm and room temperature). As seen in Fig. 4.14a, resonant dips associated with the excitation of HW and SP modes shift towards higher angles of incidence when the refractive index n_b of a liquid at the sensor surface increases. The fitting of the measured reflectivity spectra with a transfer matrix-based model revealed that the hydrogel thickness d_h was between 1.86 and 1.91 μm and its index n_h

linearly increased with the bulk refractive index of the sample with a slope of $dn_h/dn_b = 0.89$. These results indicate that approximately 90% of the hydrogel volume was accessible for EG molecules diffusing from the aqueous phase into the hydrogel film which is in agreement with the lower maximum shift of HW resonance angle (0.64 deg) compared to the corresponding critical angle shift (0.68 deg) (see Fig. 4.14a). The sensitivity to bulk refractive index changes δn_b was determined as $S = \delta\theta/\delta n_b$, where $\delta\theta$ is the angular shift of the reflectivity dip. The HOWS exhibited a sensitivity of $S = 81$ deg RIU^{-1} that is 1.3-fold lower than the one measured for SPR $S = 106$ deg RIU^{-1}. However, the full width in the half minimum (FWHM) of the HW resonance dip was of $\Delta\theta = 0.1$ deg which is approximately 50-fold lower compared to that of the SP dip of $\Delta\theta = 5.1$ deg. In refractometric sensors based on spectroscopy of guided waves, the figure of merit defined as $\chi = S\Delta\theta$ is inversely proportional to the resolution with which the refractive index variations can be measured [30]. By comparing the figure of merit of HOWS ($\chi = 810$) with that of SPR ($\chi = 20.8$), we estimated that HOWS can allow measurement of the refractive index variations on the sensor surface with an accuracy improved by a factor of about 40 with respect to regular SPR. Fig. 4.14b shows the time evolution of HOWS and SPR reflectivity signal R measured upon the successive flow of PBS samples spiked with EG at concentrations of 0%, 0.125% ($\delta n_b = 1.23 \times 10^{-4}$ RIU), 0.25% ($\delta n_b = 2.45 \times 10^{-4}$ RIU), 0.375% ($\delta n_b = 3.68 \times 10^{-4}$ RIU) and 0.5% ($\delta n_b = 4.9 \times 10^{-4}$ RIU). These data show that the reflectivity signal changed with a slope of dR/dn_b of 78 and 5.6 per RIU for HOWS and SPR-based measurements, respectively, which translated to 10 fold higher refractive index resolution provided by HOWS (1.3×10^{-6} RIU) compared to that of SPR (1.3×10^{-5} RIU) (defined as the ratio of standard deviation $\sigma(R)$ and the slope dR/dn_b). This factor is lower than that predicted by the previous comparison of figure of merit due to the lower coupling efficiency to HOW modes and due to the non-symmetrical SPR resonance dip which exhibited higher slope below the resonant angle θ_{SPR} than that above it.

4.3.3.3 Sensitivity to swelling changes of HOWS sensor

As shown in previous studies, changes in swelling of NIPAAMm hydrogel films occur upon the binding of biomolecules [69, 105] as well as due to variations in the ionic strength and pH [60, 105, 108] which may interfere with the response due to the specific capture of target analyte [109]. In general, the binding of target molecules as well as the swelling variations alter the thickness d_h and consequently refractive index n_h of the hydrogel film leading to a shift of the angular position of resonant dip associated with the excitation of hydrogel
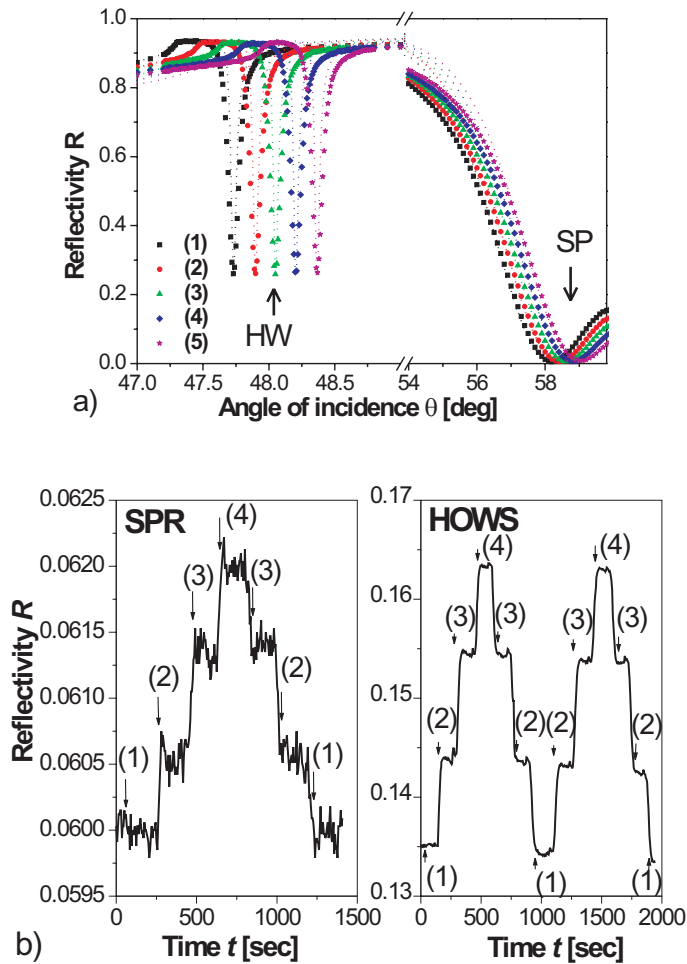
Figure 4.14: (a) Measured angular reflectivity spectra for a hydrogel waveguide film in contact with PBS buffer spiked with ethylene glycol (EG) at the concentration from (1) 0, (2) 2%, (3) 4%, (4) 6% and (5) 8%. The fitted spectra are shown as dotted line. (b) Comparison of the time evolution of the sensor signal measured by SPR and HOWS upon the successive injections of the PBS buffer spiked with EG at concentrations of (1) 0.125%, (2) 0.25%, (3) 0.375%, (4) 0.5%.

waveguide and surface plasmon modes. The sensitivity of HOWS and SPR to swelling changes of a binding matrix was investigated in an experiment in which buffers with pH between 4 and 7 were flowed over the hydrogel film. As seen in Fig. 4.15a, decreasing the pH causes an increase of the resonant angle θ_{SP} and a decrease of the resonant angle θ_{HW}. The fitting of measured angular reflectivity spectra presented in Fig. 4.15a revealed that the decrease of pH caused a collapse of the gel upon which the thickness decreased from $d_h =$

2600 nm (pH = 7) to d_h = 1400 nm (pH = 4). Let us note that in this experiment the surface mass density of the gel ($\Gamma = 10^5$ ng mm^{-2}) did not change upon the swelling and that the increased coupling efficiency observed for HW mode propagating along the hydrogel film with the lower thickness is caused by a stronger overlap of the field of the excitation incident wave and HW. In Fig. 4.15b, the experimental dependence of the resonant angles θ_{HW} and θ_{SP} on the thickness of the gel is compared to simulations based on transfer matrix model. These data reveal good agreement between theory and experiment and show that changes in θ_{HW} due to the swelling variations are an order of magnitude lower than those for θ_{SP}. In addition, the simulations show that the derivation $\partial\theta_{HW}/\partial d_h$ can reach zero for the certain thickness d_h which illustrates that the sensitivity of θ_{HW} to small swelling variations can be totally eliminated by a design of the hydrogel binding matrix. This is an important feature of HOWS as the regular SPR exploiting a three dimensional binding matrix does not allow distinguishing between the surface mass density and swelling changes.

4.3.3.4 Immobilization of catcher biomolecules

In order to demonstrate the application of HOWS for the monitoring of molecular binding events, IgG catcher molecules were firstly immobilized to the NIPAAm hydrogel. As seen in Fig. 4.16a, the covalent coupling of IgG to the gel shifted the angular position of the resonant dip from θ_{HW} = 47.68 deg to 47.80 deg. By fitting the changes in the angular reflectivity spectra, we determined that the surface mass density increased due to the loading of IgG molecules in the hydrogel from Γ = 98 ng mm^{-2} to 118 ng mm^{-2}. After the blocking the un-reacted TFPS groups by ethanolamine and rinsing with PBS, the surface mass density decreased to Γ = 114 ng mm^{-2}. This decrease can be attributed to the release of loosely bound polymer chains and IgG molecules from the hydrogel film. By comparing the surface mass density before and after the loading with IgG molecules, the surface coverage of the immobilized IgG can be estimated as $\Delta\Gamma$ = 16-20 ng mm^{-2}. The immobilization of IgG on a gold surface by using thiol SAM with carboxylic moieties resulted in the surface coverage of $\Delta\Gamma$ = 1.7 ng mm^{-2} as determined by the analysis of the angular reflectivity spectra in Fig. 4.16b.

4.3.3.5 Immunoassays-based HOWS biosensing

The affinity binding of a-IgG molecules was observed upon a sequential injection of a series of samples with a-IgG dissolved in PBST at concentrations ranging from 0.6 nM to 0.6 μM.
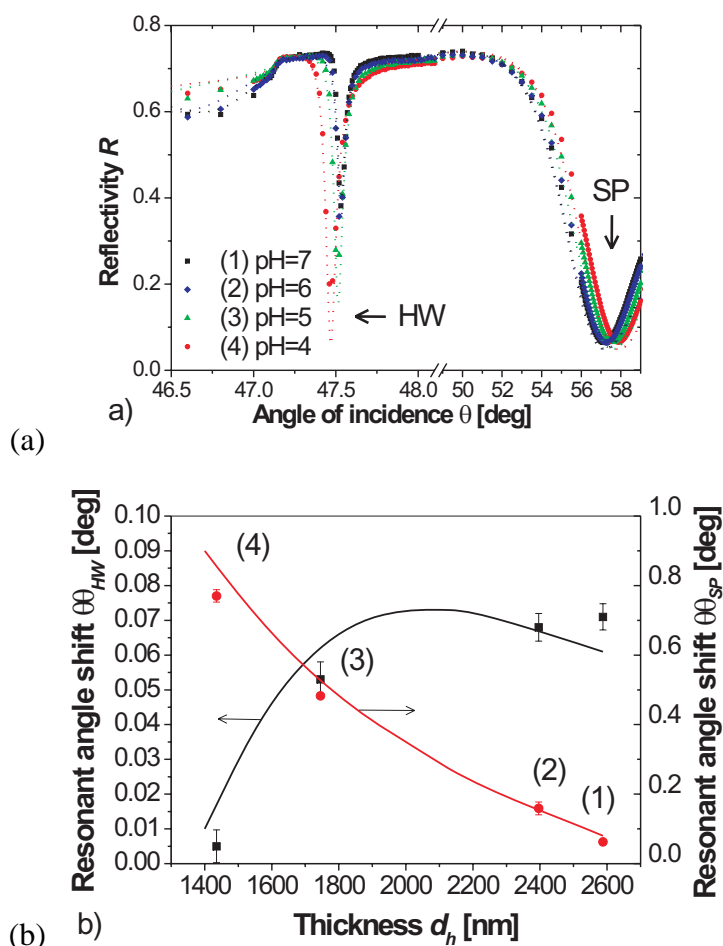
Figure 4.15: (a) Angular reflectivity spectra for a hydrogel film measured in buffer with pH value of (1) 7, (2) 6, (3) 5, (4) 4. (b) The dependence of the resonance angle for the excitation of HW and SP modes on the thickness of the hydrogel observed experimentally (dots) and obtained from transfer matrix-based simulations (line).

Each sample was flowed over the sensor surface with immobilized catcher molecules for 30 minutes followed by a 10-minute rinsing with PBST buffer. As seen in the Fig. 4.17a, the capture of a-IgG molecules during a sample flow was manifested as a gradual increase in the HOWS and SPR reflectivity signal δR due to the affinity binding-increased refractive index on the surface. In a control experiment, no measurable increase signal δR was observed for a flow of 6 and 60 nM a-IgG over the surfaces that were not modified with IgG molecules. The calibration curve showing the dependence of the reflectivity changes on the concentration of a-IgG in a sample is presented in Fig. 4.17b. These data reveal that the reflectivity changes δR observed by HOWS were larger compared to SPR and allowed
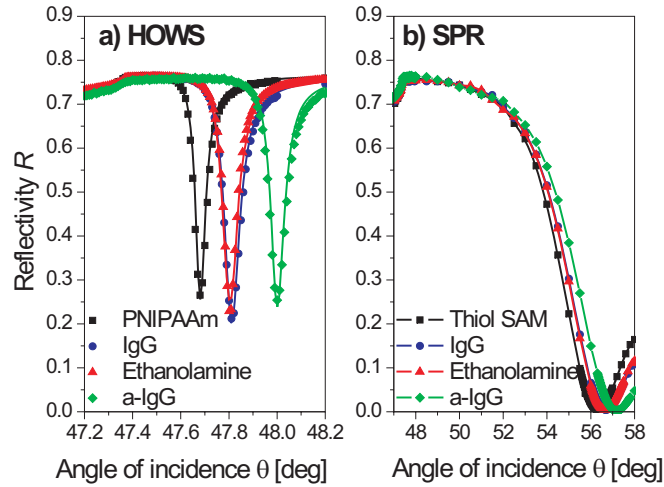
Figure 4.16: Angular reflectivity spectra of (a) a hydrogel film and (b) thiol SAM in contact with PBST buffer (black squares), after the immobilization of catcher molecules (blue circles, IgG), incubation in ethanolamine (red triangles) and saturation of affinity binding of analyte molecules (green diamonds, a-IgG), measured by (a) HOWS and (b) SPR, respectively.

for the detection of a-IgG with 5-fold improved limit of detection (LOD) of 10 pM. The limit of detection was determined as the concentration for which the calibration curve reaches the three-time standard deviation of reflectivity signal baseline $3\sigma(R)$. To observe the binding capacity of the sensor, a solution with a-IgG molecules at the concentration of 0.6 μM was flowed over the sensor surface until the sensor response was stabilized. The sensor response stabilized much slower for hydrogel binding matrix (the slope $\delta R/\delta t$ decreased 50-fold after 200 minutes) compared to SPR with monolayer surface architecture (after 17 minutes). From the induced shifts $\partial\theta_{SPR}$ = 0.55 deg measured by SPR and $\partial\theta_{HW}$ = 0.19 deg obtained by HOWS (Fig. 4.17), the amount of captured a-IgG was determined as 2.6 and 36 ng mm^{-2} on the thiol SAM and in the hydrogel, respectively. Let us note that we carried out similar experiment for the hydrogel matrix with SPR readout of a-IgG affinity biding (data not shown), and we observed 5-fold lower angular shift $\delta\theta_{SPR}$ (compared to that in Fig. 4.16b) owing to the fact that th binding-induced refractive index increase in the gel was compensated by the effect of increased hydrogel swelling (thickness). The HOWS angular shift was too large to be measured by tracking the reflectivity change δR. Therefore, the corresponding reflectivity change was estimated as $\delta R_{HW} = \delta\theta_{HW} \times \partial R/\partial\theta$ = 1.72 which is 14.3-fold larger than that measured by SPR of δR_{SPR} = 0.12. The reason for the slow sat-
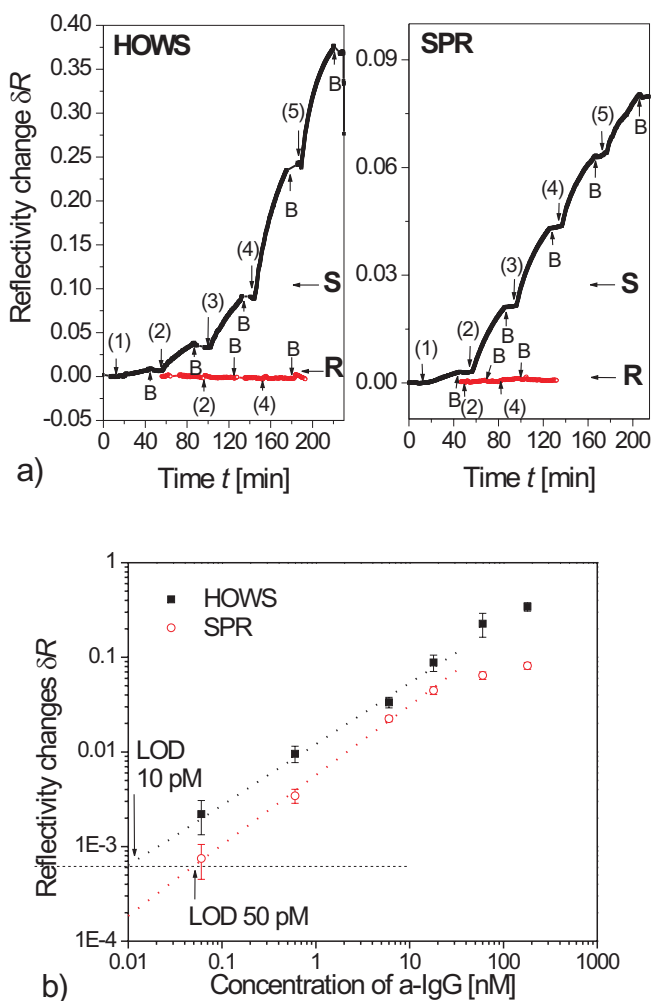
Figure 4.17: (a) The time kinetics of the SPR and HOWS reflectivity changes δR due to the affinity binding of analyte a-IgG molecules dissolved at the concentration of (1) 0.6, (2) 6, (3) 18, (4) 60 and (5) 180 nM flowed over the sensor surface, modified with IgG catcher molecules (S) and a reference surface without IgG molecules (R). In between injections of samples, the sensor surface was rinsed with PBST buffer (B). (b) The calibration curves for the detection of anti-IgG measured by HOWS (black squares) and SPR (red circles) fitted with linear function (correlation coefficients 0.9913 (n = 4) and 0.9961 (n = 4), respectively).

uration of the HOWS signal and for only five-fold improvement of LOD is owing to the slow diffusion of the analyte to the sensor surface. The mass transport coefficient of the a-IgG molecules to the hydrogel surface was calculated as $k_m \sim 3 \times 10^{-3}$ mm s^{-1} by using Eq. 1.36. By fitting the measured SPR kinetics $R(t)$ with the Langmuir adsorption model (data

not shown), the association rate constant for the a-IgG/IgG pair was estimated as $k_a > 10^5$ M^{-1} s^{-1}. For the receptor surface coverage in the hydrogel of $\Delta\Gamma \sim 1.3 \times 10^{-13}$ mol mm^{-2} (corresponding to IgG surface mass density of $\Delta\Gamma$ = 20 ng mm^{-2} determined previously and to the molecular weight of IgG 150 kDa), the affinity binding rate of $k_a \, \Delta\Gamma > 10^{-2}$ mm s^{-1} is obtained that is more than three times higher than k_m and which confirms that the molecular binding was diffusion controlled.

4.3.4 Summary

Implementation and applications of the hydrogel matrix in SPR-based biosensors have been carried out through refractometric measurements. In the biosensor scheme, the hydrogel adlayer plays not only a three dimensional binding matrix but a optical wave guiding layer. The surface grafted photo-crosslinkable carboxylated NIPAAm hydrogel is able to be modified with catcher molecules by amine coupling chemistry. The biosensors exploiting the hydrogel optical waveguide (HOW) mode exhibits better sensitivity with respect to those with regular SP mode for label-free detection for an immuno-affinity assay. The measured results indicated that HOW spectroscopy (HOWS) allow the limit of detection at the levels of picomolar.

4.4 Immunoassay-based biosensor exploiting HOW field-enhanced fluorescence spectroscopy

4.4.1 Motivation

According to the study in Section 4.2, the analyte in a sample dissolved at a low concentration is preferentially bound by the catcher molecules at the outer interface of hydrogel matrix due to the slow diffusion rate. This region overlaps with the strongest field intensity of the HOW mode which can be exploited for probing the binding of fluorophore-labeled molecules. Therefore, the HOW-field enhanced fluorescence spectroscopy (HOW-FS) was investigated for the detection of a trace of analytes. The hCG is a hormone comprising an α-subunit and a β-subunit which are held together by non-covalent hydrophobic and ionic interactions [110]. hCG only promotes progesterone production for 3-4 weeks following pregnancy implantation. Free β-subunit is the alternatively glycosylated monomeric variant of hCG made by all non-trophoblastic advanced malignancies [111], and promotes growth and malignancy

of advanced cancers [112, 113]. Therefore, the ability to measure the β-hCG level is critical in the monitoring germ cell and trophoblastic tumors. The potential of HOW-FS was demonstrated by using sandwich immunoassays for detection β-hCG.

4.4.2 Materials and methods

The preparation and characterization of the layer structures supporting regular SP, LRSP and HOW modes were described in Sections 4.2 and 4.3 as well as the modification of the hydrogel with IgG capture molecules. In a immunoassay model system, the protein materials were the same with those used in Sections 4.2 and 4.3, i.e. mouse IgG (IgG) and Alexa-Fluor-647 dye-labeled anti-mouse goat IgG (a-IgG). For the detection of β-hCG, capture IgG against β-hCG (c-IgG, Cat. no. MAF05-627) and detection monoclonal IgG against β-hCG (d-IgG, Cat. no. MAF05-043) were obtained from Meridian Life Science (Saco, ME). The d-IgG was labeled with Alexa-Fluor-647 dye by using a labeling kit (cat. No. A-20186) from Invitrogen (Carlsbad, CA).

The modification of c-IgG molecules via EDC/TFPS coupling chemistry in hydrogel followed the same protocol described in Section 4.3. Afterwards, the analyte samples containing β-hCG disolved at concentrations from 1 pM to 1 nM was flowed over the sensor surfaces for 20 min. After 3 minute buffer wash, solution of the d-IgG tagged with Alexa-flour 647 at a concentration of 5 nM was flowed into the flow-cell for 10 min.

4.4.3 Results and discussion

4.4.3.1 Immunoassay in a model system by HOW-FS

In this subsection, the performance of LRSP-FS biosensors with IgG-modified hydrogel matrices at thicknesses of n_h = 130, 1440 nm are in comparison with that of the HOW-FS biosensor with hydrogel matrix at a thickness of n_h = 1440 nm. Fig. 4.7b in Section 4.2 illustrates that after the capture of a-IgG molecules in the gel with the thickness of $d_h = 1400$ nm, the angular fluorescence spectrum $F(\theta)$ exhibits two strong fluorescence peaks located at the angles $\theta_{LRSP} = 48.95$ deg and $\theta_{HOW} = 47.60$ deg at which the LRSP and HOW modes are excited, respectively. In addition, the thickness n_h=130 nm of hydrogel was optimized in order to effectively probe a-IgG binding with the LRSP mode. Therefore, we examined the performance of fluorescence biosensors exploiting LRSP and HOW modes for probing hydrogel binding matrices through measuring a-IgG affinity binding upon a successive
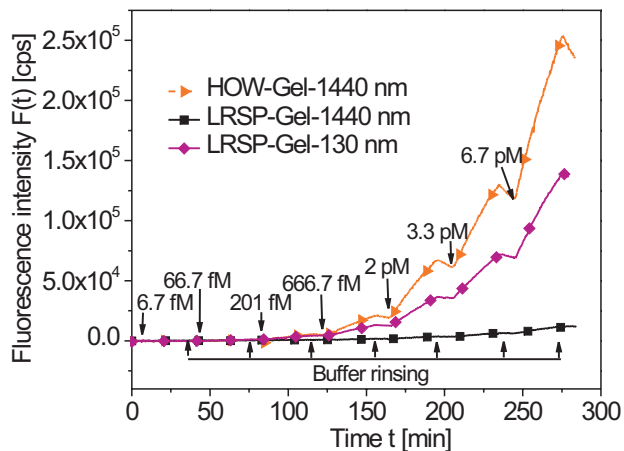
Figure 4.18: The binding kinetics observed from the flurescence signal $F(t)$ that was measured upon the successive flow of samples with a-IgG molecules (labeled with Alexa Fluor-647) at concentrations increasing from $\alpha_0 = 6.7$ fM to 6.7 pM. IgG-functionalized hydrogel binding matrices with the thickness of $d_h = 130$ (solid diamond), 1440 (solid square) nm were probed by LRSP mode and the hydrogel binding matrix with the thickness of $d_h = 1440$ nm was probed by HOW mode (solid triangle). Injection times for each sample with a-IgG molecules and rinsing of the sensor surface with buffer are clearly indicated.

flow of series of samples with increasing concentrations of a-IgG. The biosensor based on HOW-FS showed higher fluorescence responses F to the a-IgG detection than that based on LRSP-FS as seen in Fig. 4.18. According to the simulation for the electric intensity profile upon the resonant excitation of HOW (Fig. 4.5), the highest enhancement of the electromagnetic field intensity occurs in the vicinity to the gel outer interface where the analyte binding preferably occurs. However, the field intensity of the evanescent LRSP wave exponentially decays with the distance away from the gold surface. In addition, the further comparison in the LOD for a-IgG detection was demonstrated. For LRSP field-enhanced fluorescence spectroscopy with the d_h=130nm, noise of the fluorescence signal baseline $\sigma(F)$ = 55 cps (SD) and the maximum slope $dF/(dt\alpha_0)$ = 0.34 cps min^{-1} fM^{-1} were measured. For HOW field-enhanced fluorescence spectroscopy, higher noise of the fluorescence signal baseline $\sigma(F)$ = 107 cps (SD) and larger slope of $dF/(dt\alpha_0)$ = 0.59 cps min^{-1} fM^{-1} were observed. These data correspond to the similar limit of detection below 20 fM determined as $3 \times \sigma(F)/[\Delta t \cdot dF/(dt \cdot \alpha_0)]$ for both LRSP and HOW-based biosensors with hydrogel at

thicknesses of d_h = 130 and 1440 nm, respectively.

4.4.3.2 β-hCG detection by HOW-FS

(a)

(b)
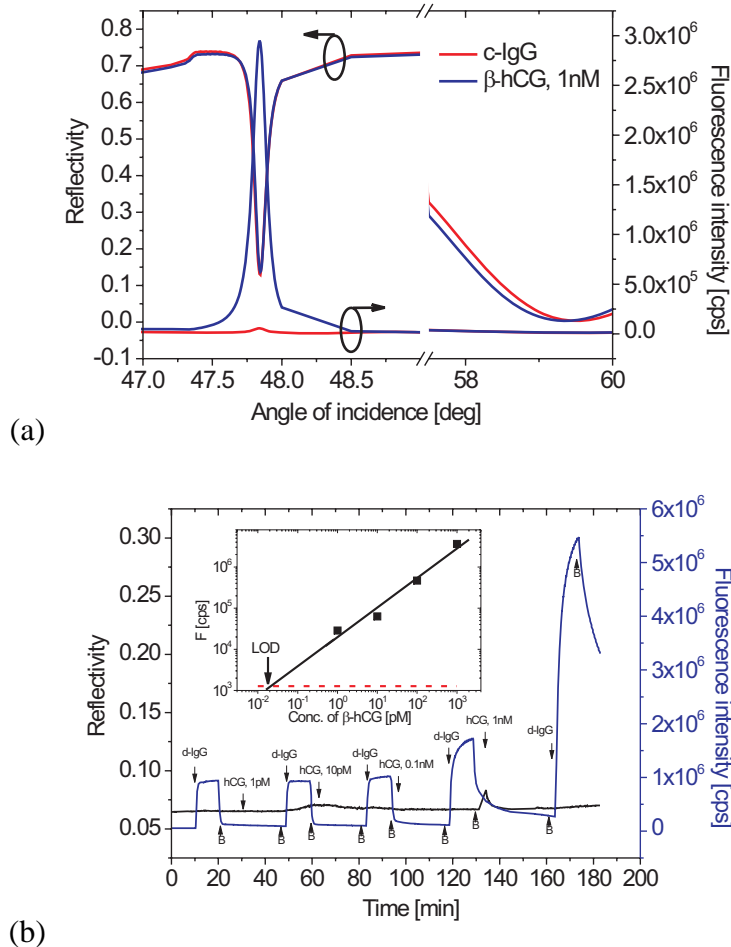
Figure 4.19: (a) Angular reflectivity and fluorescence spectra for detection of β-hCG analyte in sandwich immunoassy. (b) The time revolution of sandwich immunoassay for β-hCG dissolved in PBST at concentrations from 1 pM to 1 nM.

The sandwich immunoassay was applied in β-hCG detection. The angular reflectivity $R(\theta)$ and fluorescence $F(\theta)$ spectra for the IgG modified hydrogel and after the detection of 1 nM β-hCG sample show that a strong fluorescence peak appear at the resonant angle of HOW whereas no significant fluorescence response to the presence of β-hCG occurred with the probing of the SP mode. The reason for the difference between two optical modes should be due to slow diffusion of β-hCG and d-IgG, and limited profile of the SP field enhancement,

see Fig. 4.19a. This observation is in agreement with that in Subsection 4.4.3.1. The time evolution of the sensor fluorescence responses for the detection of β-hCG samples at concentrations from 1 pM to 1 nM measured by HOW-FS indicates that the fluorescence signal measured after the injection of d-IgG increases with the concentration of β-hCG (Fig. 4.19b). The calibration curve for β-hCG detection was inserted in the Fig. 4.19b and the LOD was determined from the concentration at the intersection of the calibration curve and three times standard deviation of the fluorescence signal baseline (dash line in red) as 20 fM which was improved from the previous study for the detection of β-hCG performed on a well-oriented c-IgG layer in SPFS by a factor of 30 [114].

4.4.4 Summary

Fluorescence immunoassay exploiting hydrogel optical waveguide modes (HOWs) for the detection β-hCG is presented. This HOW-enhanced fluorescence spectroscopy biosensor exhibits unique features including the large binding capacity, strong enhancement of electromagnetic field intensity at the interface between hydrogel and aqueous medium. In a immunoassay model system, the fluorescence readout in HOW-FS was stronger than that in surface plasmon-enhanced fluorescence spectroscopy (SPFS) with a hydrogel binding matrix at an optimized thickness. Furthermore, the ultra-low limit of detection was obtained as 20 fM for the model system and β-hCG detection in HOW-FS biosensors.

5 Bacterial detection

In important application areas including food control and medical diagnostics, SPR biosensors have the potential to be employed for simpler and faster detection of bacterial pathogens, which are currently routinely analyzed by time-consuming methods including culturing [115], polymerase chain reaction [116] and enzyme-linked immunosorbent assays. Up to now, SPR biosensors have been implemented for the detection of a range of bacterial pathogens including *Escherichia coli* O157:H7 [117, 118, 119], *Salmonella* [120] and *Listeria monocytogenes* [120, 121] and they were shown to detect these analytes at concentrations as small as 10^3 - 10^7 colony forming unit (cfu) per mL. However, this sensitivity is not sufficient as for many common pathogens even several cells in a sample can be infective [122]. In this chapter, we will discuss on the problems encountered in the bacterial detection by using the evanescent wave-based biosensors, including the capture efficiency of bacteria on surface and the profile of probing field. In addition, we employed SPFS based on extended LRSP mode for ultra-sensitive detection of pathogenic bacteria in a sandwich immunoassay platform.

5.1 On the role of the diffusion-driven mass transfer and profile of probing field

The limited sensitivity of SPR biosensors for the detection of bacterial pathogens is mainly caused by low efficiency of analyte capture and by small binding-induced refractive index changes associated with the binding of bacterial cells on the sensor surface. Owing to the micrometer size of these cells, their transfer to the sensor surface is strongly hindered by a slow diffusion and the captured cells are exposed to a shear stress, which results in the destabilization of the bonding between catcher and analyte molecules [123, 124, 125]. In addition, regular SPR biosensors typically probe the sensor surface with a surface plasmon field that evanescently decays to distances between 100-200 nm from the surface. Therefore, only a small portion of adhered bacteria is probed and finally detected. Several ap-

proaches have been investigated to advance the performance of SPR biosensors including pre-concentrating of bacteria by magnetic particles [126], di-electrophoresis [127, 128] and by disrupting the bacterial analyte [129]. In order to increase the refractive index changes, assays with nanoparticle-labels have been employed [129]. Only recently, a layer architecture that supports long range surface plasmons (LRSPs) was reported for the detection of bacterial pathogens [130]. These surface plasmon modes originate from the coupling of two SPs on the opposite interfaces of a thin metallic film embedded between dielectrics with similar refractive indices. LRSPs exhibit larger penetration depths that can be tuned to match the size of bacterial pathogens and response to the changes of the bulk refractive index with ultra high sensitivity [21].

5.1.1 Motivation

The objective of this study was to determine the dependence of the SPR biosensor signal intensity due to the capture of bacterial analyte on the flow-conditions and the profile of electromagnetic field of surface plasmon wave. In model experiments we analyzed the affinity binding of a non-harmful bacterial model strain (*E. coli* K12) to the surface functionalized with appropriate antibodies. We compared the sensitivity of sensor platforms with regular SPs and LRSPs and investigated the effects of diffusion mass transfer and shear force. To the best of our knowledge, detailed investigations on how these parameters affect the sensitivity of SPR biosensors for the detection of bacterial pathogens have not been addressed up to now. The obtained results will be valuable for future developments of SPR biosensors with improved sensitivity for the detection of microbial analytes.

5.1.2 Materials and methods

Goat polyclonal IgGs (positive control IgG, p-IgG) reacting with O and K antigenic serotypes of *E. coli* were purchased from Abcam (cat. No. ab13627, Cambridge, UK). Goat polyclonal IgG (negative control IgG, n-IgG,) targeting *E. coli* O157:H7 was obtained from KPL, Inc. (cat. No. 01-95-90, Gaithersburg, MD). The antibody against *E. coli* O157:H7 does not recognize *E. coli* K12 epitopes and was used in a control experiment.

5.1.2.1 Flow-cell

The optical setup for the SPR biosensor was described in Section 2.4. The preparaction and modification of layer structures for supporting SP and LRSP modes were present in

detail in Section 2.2 and 2.3.1, respectively. The flow chamber was fabricated by casting a photolithographically defined relief with a flow chamber into polydimethylsiloxane (PDMS). The depth of the flow chamber was h = 95 μm, length L = 9 mm and width w = 6 mm, see Fig. 5.1. The volumetric flow rate between 50 μL min^{-1} to 700 μL min^{-1} was used which corresponds to the Reynolds number between Re = 8.8 and 123. For these conditions, the flow in a flow chamber is laminar and the flow distribution $v_y(x)$ across the flow channel exhibits parabolic profile with the maximum flow velocity v_{max} in the middle of the cell ($x = h/2$) and $v = 0$ at the sensor surface ($x = 0$).
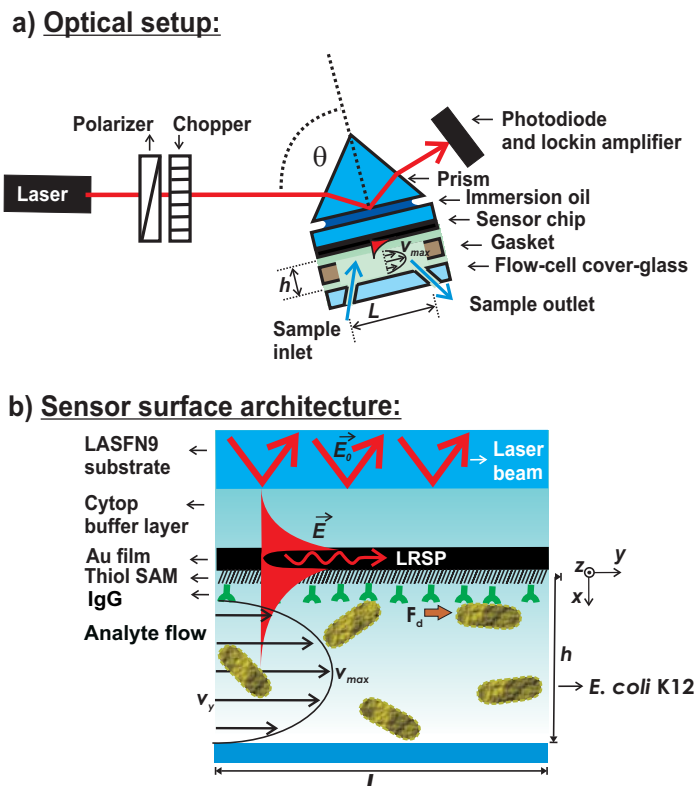
Figure 5.1: The scheme of (a) optical setup (b) sensor chip layer architecture supporting LRSP with antibody recognition elements for a capture of target analyte.

5.1.2.2 Sample preparation, characterization and detection assay

E. coli K12 was cultured overnight in tryptic soy broth (Merck, Darmstadt, Germany) with aeration at 37 °C. Then, 10 mL bacterial culture was centrifuged at 2000 g for 10 min at 4°C. The cell pellet was washed twice with PBS buffer and resuspended in 10 mL PBST buffer, aliquoted and stored at 4°C prior to the analysis. The cell concentration was determined

by using a conventional colony counting method. Cells were cultured on LB (10 g tryptone L^{-1}, 10 g NaCl L^{-1}, 5 g yeast extract L^{-1}, 15 g agar L^{-1}) plates for 4 days followed by the counting of colonies formed by viable cells. The average hydrodynamic diameter of *E. coli* was determined by dynamic light scattering as 1.57 μm. In this experiment, 0.5 mL PBST sample with the 10^7 cfu mL^{-1} concentration of *E. coli* K12 was analyzed by a Zetasizer (Malvern Instruments, Worcestershire, UK). For SPR biosensor detection, samples containing varying numbers of *E. coli* cells (ranging from 10^4 cfu mL^{-1} to 10^8 cfu mL^{-1}) were prepared and sequentially injected into the flow cell. After the flow of each sample, the sensor surface was rinsed with PBST buffer for 10 min in order to establish a baseline. For comparison, the number of captured *E. coli* K12 cells was determined by an optical microscope (Hund Wetzlar, Germany) into which the same sensor chip and the flow cell as used in SPR experiments were loaded. The images were taken with a time interval of 30 s and number of bound bacteria was evaluated by using ImageJ software (National Institutes of Health, USA).

5.1.2.3 Affinity binding of bacterial pathogens to the sensor surface

Upon the flow of bacterial pathogens, the analyte diffuses to the sensor surface with attached recognition elements. The diffusion mass transfer of an analyte from the solution to the surface can be described by a following diffusion rate [93]:

$$k_m = 1.378 \left(\frac{v_{max} D_s^2}{hL} \right)^{1/3}, \tag{5.1}$$

where D_s is a diffusion coefficient of an analyte in a sample (e.g., D_s = 2.8$\times$10^{-7} mm^2 s^{-1} for *E. Coli* was determined by dynamic light scattering). Upon a flow of a sample, a shear force parallel to the surface expose captured bacteria with around micrometer size to a significant drag force F_d that destabilizes bonds between the antibodies and bacteria membrane. This force is proportional to the maximum sample flow velocity v_{max} and can be expressed as:

$$F_d = 32a\eta \frac{dv_y}{dx} = 1.28 \cdot 10^2 a\eta \frac{v_{max}}{h}, \tag{5.2}$$

where a is the hydrodynamic radius of a bacteria and η is the viscosity of a sample. Due to the multiple point attachment, the affinity binding of bacteria to recognition elements on the sensor surface is more complex than that of smaller biomolecules [123]. Numerous models have been developed to describe the interaction of cells with surface under a flow [125].

In these models, the destabilization of bonds between a cell and a surface is described by dissociation affinity binding rate which is a function of the drag force F_d:

$$k_d = k_d^0 \exp\left(\frac{\gamma F_d}{k_b T}\right).$$

(5.3)

where k_d^0 is the dissociation rate constant for $v_{max} = 0$, k_b is the Boltzmann constant, T is the temperature and γ is a characteristic length of the interaction between receptors tethered to the surface and epitope on the cell membrane. There can be shown that for large flow velocities, the equilibrium surface density of captured bacteria on the surface is proportional to $1/k_d$ (proportional to the average time upon which the analyte stays captured on the surface). Let us note that in this simplified model other phenomena related to the multiple point attachment and shear force such as rolling of cells along the surface [125] were omitted.

5.1.3 Results and discussion

5.1.3.1 Characterization of a sensor surfaces supporting LRSP and SP modes

The angular reflectivity spectra $R(\theta)$ measured upon the probing of sensor surface with regular SPs and LRSPs are compared in Fig. 5.2a. The excitation of these modes was manifested as a sharp dip in the reflectivity spectrum and the full width of half maximum (FWHM) was $\Delta\theta = 4 \pm 0.11$ deg for SPs and $\Delta\theta = 0.3 \pm 0.01$ deg for LRSPs. The narrower resonance associated with the excitation of LRSPs allowed a more accurate measurement of refractive index changes on the sensor surface. As reported in our previous study [80], the figure of merit for the used LRSP-supporting structure was about 4-fold larger compared to that on which regular SPs propagate when detecting (bulk) refractive index changes within the whole evanescent field of these waves. The measured curves were fitted by a transfer matrix-based model of Fresnel reflectivity in order to calculate the profile of electric intensity field in the resonance. The results shown in Fig. 5.2b reveal that the LRSP evanescent field stretched deeper from the sensor surface into the sample with the penetration depth of $L_p = 550$ nm compared to $L_p = 181$ nm of SPs (the penetration depth is defined as the distance from the surface at which the amplitude the evanescent field drops to $1/e$). The surface mass density of IgG immobilized on LRSP and SP-supporting sensor chips was determined as $\Gamma = 3.43 \pm 0.96$ ng mm^{-2} by the analysis of reflectivity spectra measured before and after coupling of IgG recognition elements (see Fig. 5.2a), The surface mass density is close to a close packed monolayer [99] and it was obtained as $\Gamma = d_p(n_p - n_b)\partial c/\partial n$ where n_b is the refractive index for PBST buffer, n_p is refractive index of IgG layer fitted from measured

spectra, the coefficient $\partial n / \partial c$ of 0.1875 μL mg^{-1} was acquired from literature [97] and the thickness of IgG layer was assumed to be d_p = 5.5 $\pm$ 1.5 nm.

(a)

(b)
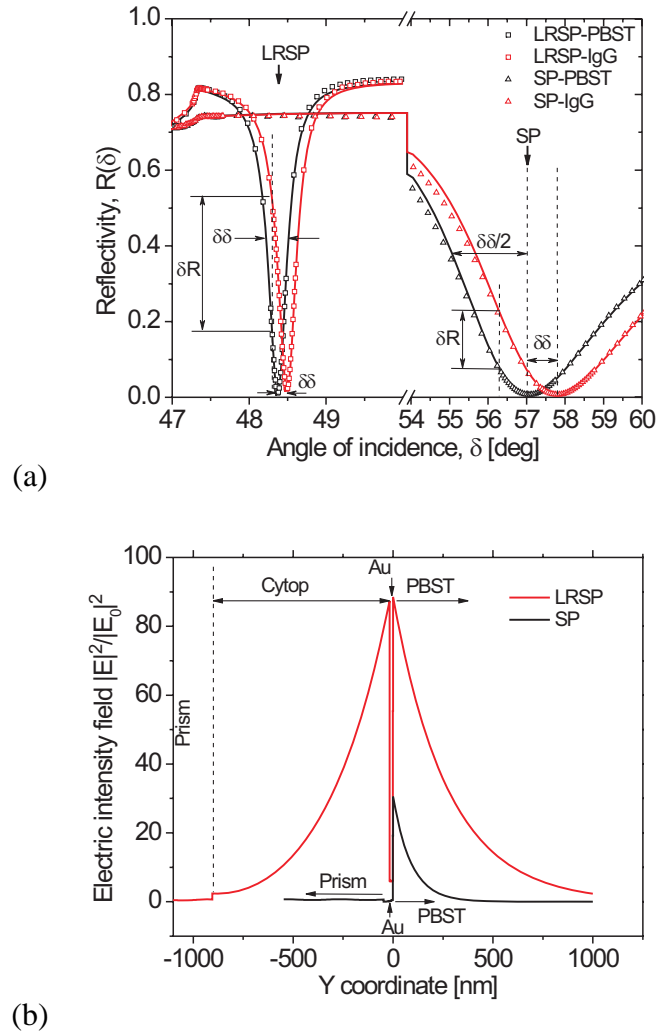
Figure 5.2: (a) Angular reflectivity spectra measured for sensors with layer structures for support-ing LRSPs (squares) and regular SPs (triangles). The measurements were performed in PBST before (in black) and after (in red) immobilization of antibody recognition ele-ments. The corresponding fitted curves are shown (lines). (b) Profile of electric intensity field of LRSPs (red curve) and regular SPs (black curve) obtained from simulations.

5.1.3.2 Observation of affinity binding of bacteria by LRSPs

In this experiment, a sample with *E. coli* dissolved in PBST at a concentration of 10^8 cfu mL^{-1} was flowed over the surface functionalized with antibody p-IgG at a flow rate with v_{max}

= 8.8 mm s^{-1} for 30 min followed by rinsing with PBST for 5 min. The binding of *E. coli* K12 cells was observed by probing the sensor surface with LRSPs and by using an optical microscope in order to correlate the measured reflectivity changes ΔR and the number of adhered cells. Fig. 5.3 shows that equilibrium in the reflectivity signal $R(t)$ was reached after ∼20 min flow of the sample. After that time, the 250±15 cells mm^{-2} adhered on the surface which corresponds to the measured reflectivity change of ΔR = 0.0247±8 × 10^{-4} (errors represent the standard deviation). For the average diameter of *E. coli* K12 of 1.54 μm, these data indicate that the surface coverage of bacteria was 0.047±0.003%, which is consistent with observations reported by other groups [131, 132, 133]. Assuming that the sensor response ΔR is proportional to the number of cells on the surface, these data indicate that the sensor is able to detect ∼20 cells adhered to the surface per mm^2. In the initial stage of the experiment presented in Fig. 5.3, the number of cells diffusing to the surface can be estimated by the diffusion rate k_m defined by Eq. 5.1 that is multiplied by the concentration of cells in the solution. For the used flow rate, the diffusion rate equals k_m = 1.27×10^{-4} mm s^{-1}, which corresponds to the flux of *E. coli* K12 of 12.7 cells mm^{-2} s^{-1}. This value is approximately ten times higher than the adhesion rate ∼1 cell mm^{-2} s^{-1} observed by probing with LRSPs and optical microscopy (see Fig. 5.3). As the density of bacteria is low, cells do not form a compact layer of which refractive index changes can be related to measured SPR variations. We assume that variations in the reflectivity spectrum are rather associated with increased losses of LRSP modes due to the scattering on sparsely distributed cells on the surface (data not shown). Let us note that besides the low number of captured cells, the signal strength measured by probing with LRSPs was limited by low refractive index contrast between bacteria (refractive index approximately 1.38 [134]) and the liquid sample (refractive index of water is n_b = 1.333 [89]).

5.1.3.3 Dependence of capture efficiency on the flow-rate

In order to investigate the effect of a flow rate to the strength of the sensor response signal ΔR, a similar experiment as in the previous section was performed using a flow velocity, which varied in the range between v_{max} = 2.2 and 30.7 mm s^{-1}. The results presented in Fig. 5.4 show that ΔR increased with the flow rate for flow velocities smaller than v_{max} = 8.8 mm s^{-1}. Above this value, the response ΔR rapidly decreased with the flow velocity v_{max}. The reason for the increasing number of cells adhering to the surface for v_{max} <8.8 mm s^{-1} was the increasing diffusion rate k_m that was proportional to $(v_{max})^{1/3}$ (see Eq. 5.1) as indicated in Fig. 5.4. The rapid decrease of the sensor response for flow velocities v_{max} >
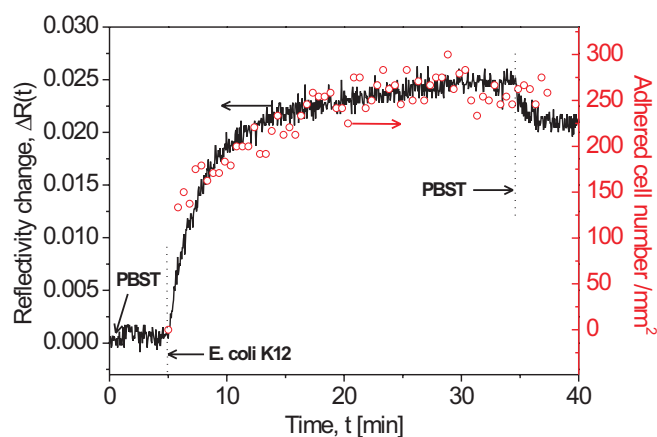
Figure 5.3: Time dependence of the sensor signal ΔR compared to the number of adhered cells upon a flow of a sample with 10^8 cfu mL^{-1} of *E. coli* K12 and the flow velocity of $v_{max} = 8.8$ mm s^{-1}.

8.8 mm s^{-1} was caused by the increasing shear force that translated to a larger dissociation constant k_d. In this study, adhered *E. coli* K12 were exposed to a drag force between 1.8 pN ($v_{max} = 2.2$ mm s^{-1}) and 25 pN ($v_{max} = 30.7$ mm s^{-1}), which was in the range of previously reported forces of 1-100 pN needed to induce the dissociation of protein bonds [135]. Our results suggest that the number of particles adhered to the surface exponentially decreases with the flow velocity v_{max} for large flow rates, which is also in agreement with the measured response (Fig. 5.4).

5.1.3.4 Comparison of sensor platforms with LRSP and regular SP

The sensitivity of biosensor for detection of bacterial pathogens relying on sensor architectures supporting LRSPs and regular SPs was evaluated. *E. coli* was dissolved in a series of samples at concentrations between 10^4 to 10^8 cfu mL^{-1} and successively flowed over the sensor surface for 20 min followed by rinsing with PBST for 20 min. The flow velocity of $v_{max} = 8.8$ mm s^{-1} which provides highest sensor response was used. Fig. 5.5 shows the measured calibration curves for the specific detection of binding of *E. coli* K12 and for a control experiment. For the specific interaction, antibody p-IgG was immobilized on the sensor surface and the antibody n-IgG, which is not specific for the *E. coli* K12 epitope, was used for the control experiment. The specific response for LRSP-supporting sensor chip was around three times larger compared to that measured with regular SPs. This im-
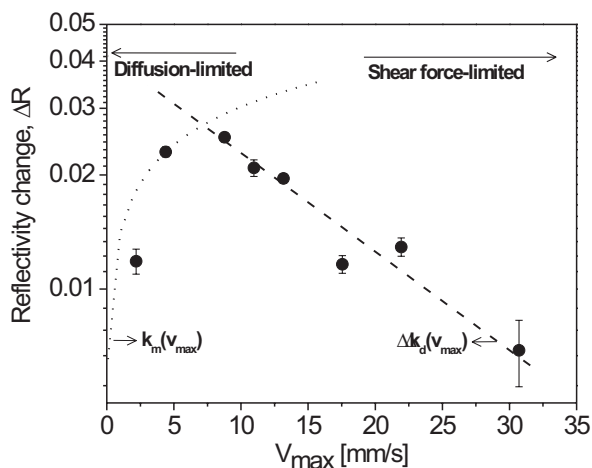
Figure 5.4: The dependence of a sensor signal ΔR measured after the flow of a sample with *E. coli* K12 dissolved at the concentration of 10^8 cfu mL^{-1} probed by LRSPs on the flow velocity v_{max}.

provement is comparable to the figure of merit enhancement by a factor of four [80] and it is similar to that reported recently by Vala et al. [130]. The control experiment revealed that on the surface with antibodies n-IgG the amount of captured *E. coli* cells was five times lower compared to that with specific antibodies.

5.1.4 Summary

The effect of diffusion mass transfer to the surface and shear force was studied in order to improve the sensitivity of SPR biosensors for direct detection of bacterial pathogens. The achieved results revealed that the flow rate dramatically changes the sensor response intensity. It is therefore of high importance to carefully control the flow rate and to stabilize the bonding between of the target bacteria and the surface as this bonding is restrained by the diffusion mass transfer of the analyte to the surface and destabilized by shear force. In addition, the SPR sensor response can be enhanced through increasing the overlap of the surface plasmon field profile with the bacterial analyte. Probing of the sensor surface by using a layer architecture supporting LRSP enhanced the sensor response due to the capture of the bacterial analyte by a factor of three when compared to regular SPs.
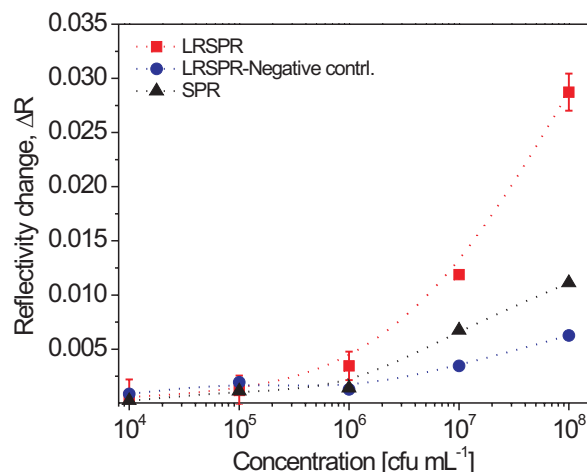
Figure 5.5: Calibration curve for detection of *E. coli* K12 by using sensor chips supporting LRSP and SP. Samples were flowed over surfaces modified with p-IgG specific to *E. coli* K12 epitopes on LRSP (solid squares) and SP (solid triangles) supporting chips. In addition, control experiment with reference n-IgG (against *E. coli* O157:H7) on the surface supporting LRSP was performed (solid circles).

5.2 LRSP-FS biosensor for ultrasensitive detection of *E. coli* O157:H7

Safety concerns about food, drinking water, and disease control related to microbial pathogens have attracted increasing attention worldwide. Among others, *Escherichia coli* O157:H7 producing Shiga-like toxins is a widespread foodborne pathogen and the infective dose is as low as 50 to 100 cells [136]. According to the Centers for Disease Control (CDC), outbreaks of *E. coli* O157:H7 cause annually ten thousands illnesses, thousands of hospitalizations and up to one hundred deaths in the USA. Conventional techniques used for the analysis of bacterial pathogens include culturing methods [115], polymerase chain reaction (PCR) [116] and enzyme linked immunosorbent assays (ELISA) [137]. These techniques can be performed only in specialized laboratories as they require trained personnel and laborious sample pretreatment. In addition, they are time-consuming as a standard confirmation process takes usually several hours [138]. Therefore, new tools that are suitable for routine detection and rapid identification of bacterial pathogens are urgently needed in order to reduce the risk to public health.

Biosensors are analytical devices extensively researched for the detection of pathogens

in food control and medical diagnostic [139]. Among these, biosensors based on surface plasmon resonance (SPR) hold a prominent position due to their advantage of real-time and direct detection as well as the possible implementation to portable devices [14]. Up to now, SPR biosensors for detecting a wide range of pathogens have been developed, however, they offer insufficient sensitivity as the limit of detection is typically larger than 10^3 cfu mL^{-1} [14]. In order to enhance the sensitivity, amplification of the sensor response by nanoparticle assays [129], improved sample preparation [121] and probing binding-induced refractive index changes by using more accurate SPR sensor schemes [130] have been investigated.

5.2.1 Motivation

In this Section, we report another approach to enhance the sensitivity for the detection of bacterial pathogens in which SPR is combined with fluorescence spectroscopy, referred to as surface plasmon field-enhanced fluorescence spectroscopy (SPFS) [82]. We advanced SPFS through a sensor architecture that enables probing the sensor surface with up to a micrometer distance by using long range surface plasmons (LRSPs) [80]. They allow probing the whole volume of captured bacterial pathogens with an approximately micrometer diameter.

5.2.2 Materials and methods

E. coli O157:H7 standard was obtained from KPL (Gaithersburg, MD) and the non-pathogenic, but highly related, *E. coli* strain K12 was cultivated in our laboratory. The average diameters of heat-killed *E. coli* O157:H7 and K12 cells were determined by dynamic light scattering (DLS) with Zetasizer from Malvern Instruments (Worcestershire, UK) as 1177 and 869 nm, respectively. Capture antibodies against *E. coli* O157:H7 (c-IgG) (cat. No. ab75244) were purchased from Abcam (Cambridge, UK). Affinity-purified detection antibodies (d-IgG) against *E. coli* O157:H7 (cat. No. 01-95-90) were acquired from KPL and labeled with Alexa-Fluor-647 dye (at a dye-to-protein molar ratio of about 4.5) by using a labeling kit (cat. No. A-20186) from Invitrogen (Carlsbad, CA). The used fluorophores exhibited the absorption and emission bands at λ_{ex} = 633 nm and λ_{em} = 670 nm, respectively. Samples for validating the method were prepared by spiking phosphate buffer saline containing 0.05% Tween 20 (PBST) with the *E. coli* O157:H7 (target analyte) or *E. coli* K12 (negative control) in the range 10^1-10^6 cfu mL^{-1}. The detection antibody was dissolved in PBST (1 nM).

5.2.2.1 Bacterial detection

(a)

(b)
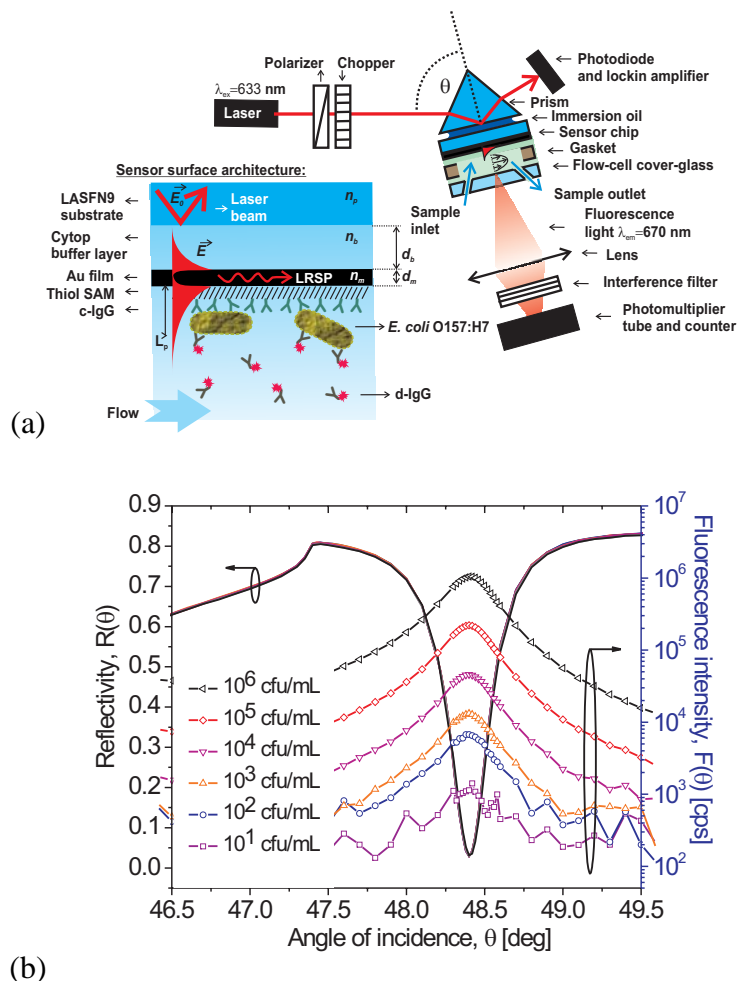
Figure 5.6: (a) The optical setup of a LRSP-FS biosensor, surface architecture and detection assay. (b) The angular reflectivity (left axis) and fluorescence (right axis) spectra measured after the analysis of *E. coli* O157:H7 at the concentrations between 10^1 and 10^6 cfu mL^{-1} (curves clearly indicated in the graph).

The optical setup for the SPFS biosensor was described in Section 2.4. The preparaction and modification of layer structure for supporting LRSP modes were present in detail in Section 2.2 and 2.3.1, respectively. Detection of the target analyte was performed by using a sandwich immunoassay format. Firstly, the sample (volume 1 mL) to be analyzed was circulated through the sensor flow cell for 20 min. Then, the sensor surface was successively rinsed with PBST for 5 min, incubated with d-IgG for 10 min and rinsed again with PBST buffer for 5 min. The analyte binding was observed after incubation with d-IgG by measuring the angular fluorescence intensity spectrum $F(\theta)$. In addition, fluorescence signal $F(t)$ was

detected in time upon the assay at an angle providing maximum signal strength.

5.2.3 Results and discussion

5.2.3.1 Characterization of LRSP

The coupling of a laser beam to LRSPs supported by the thin gold film is manifested as a narrow dip in the reflectivity spectrum $R(\theta)$, see Fig. 5.6b. Through an analysis of the reflectivity spectrum, we calculated the penetration depth of LRSPs of L_p = 1124 nm (defined as the distance from the surface at which the amplitude of the field intensity $|E|$ drops by $1/e$) which is comparable to the average size of the target analytes. As seen in Fig. 5.6b, the capture of target *E. coli* O157:H7 analyte followed by binding of fluorophore-labeled d-IgG was manifested as a strong peak in angular fluorescence spectrum $F(\theta)$ centered at the angle θ at which LRSPs are resonantly excited. The peak intensity of $F(\theta)$ increased with the concentration of *E. coli* cells. Let us note that the capture of bacteria induced a negligible shift of the LRSP dip in the angular reflectivity spectrum $R(\theta)$ indicating a superior sensitivity of SPFS with respect to SPR-based detection of binding-induced refractive index changes.

5.2.3.2 Detection *E. coli* O157:H7 in LRSP-FS

In order to determine the key performance characteristics of the LRSP-FS biosensor, the peak fluorescence signal was measured as a function of time $F(t)$ upon the analysis of samples containing target (*E. coli* O157:H7) and control (*E. coli* K12) analytes. The detection experiment was performed in cycles, in which the sensor surface was subsequently incubated with the analyte followed by the binding of labeled d-IgG. Fig. 5.7 shows the time evolution of the sensor signal $F(t)$ measured for samples with analyte concentrations between 10^1 and 10^6 cfu mL^{-1}. The abrupt increase of the fluorescence signal $\Delta F \sim 5 \cdot 10^3$ cps after the injection of d-IgG was associated with the excitation of fluorophore molecules present in a bulk solution. Afterwards, the fluorescence signal gradually increased in time due to the affinity binding of d-IgG to the *E. coli* OH157:H7 captured on the sensor surface. After rinsing with PBST, a fast decrease in the fluorescence signal was observed due to the removal of d-IgG from the bulk solution followed by the dissociation of d-IgG that was seen as a gradual decrease of the signal F. The data in Fig. 5.7 reveal that for *E. coli* O157:H7, a strong fluorescence signal was emitted and its intensity increased with increasing analyte concentration. In the control experiment, no response due to the binding of the analyte *E.*

coli K12 was observed as the fluorescence signal F dropped back to the original baseline after the incubation in d-IgG and rinsing with PBST.
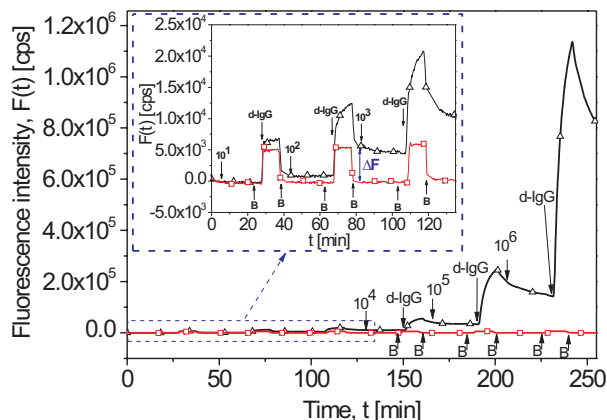
Figure 5.7: (a) Maximum fluorescence signal $F(t)$ measured upon a successive flow of target (*E. coli* O157:H7, triangles) and control (*E. coli* K12, squares) analyte dissolved at the concentrations 10^1-10^6 cfu mL^{-1}. Injections of a buffer (B), samples and d-Ab are clearly indicated in the graph. The inserted figure shows the magnified fluorescence signal $F(t)$ upon the analysis of target analyte at concentrations from 10^1 to 10^3 cfu mL^{-1}.

5.2.3.3 Sensitivity of LR-SPFS for detection of *E. coli* O157:H7

The sensor response ΔF was defined as a difference between the fluorescence signal F measured before and after the incubation with d-IgG, see Fig. 5.7. The calibration curve for the analysis of *E. coli* O157:H7 that is presented in Fig. 5.8 was averaged from a triplicate measurement and the error bars show the obtained standard deviation (SD). From this curve, the limit of detection (LOD) of 6 cfu mL^{-1} was determined as the concentration, for which the linear fit of calibration curve reaches three-fold SD of the baseline fluorescence signal $3\sigma(F) = 314$ cps. This limit of detection is in the range required by the Advisory Committee for Food and Dairy Products (ACFDP) in the UK [138] and the analysis time of 40 min is highly superior compared to that needed for the conventional analysis.
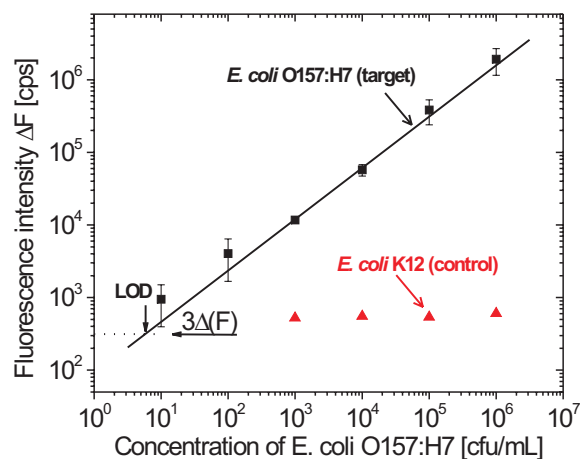
Figure 5.8: Calibration curve of LRSP-FS biosensor for detection of *E. coli* O157:H7 (squares) fitted with a linear function and the response obtained for control analyte *E. coli* K12 (triangles). The base line noise and LOD are indicated.

5.2.4 Summary

In conclusion, a new biosensor platform for ultra-sensitive detection of bacterial pathogens was developed based on long range surface plasmon-enhanced fluorescence spectroscopy (LRSP-FS). The performance characteristics of this method were evaluated for *E. coli* O157:H7, and a limit of detection of LOD = 6 cfu mL^{-1} and a detection time of 40 min per test were achieved. The high specificity was demonstrated by the lack of response for the strongly related but non-pathogenic *E. coli* strain K12. With respect to the conventional SPR biosensor technology, a substantially lower limit of detection (about 3-4 orders of magnitude lower) was achieved, which lies in the range required by regulatory bodies for the analysis of samples relevant to food control.

6 Summary

This thesis describes the efforts on advancing surface plasmon resonance (SPR)-based biosensors by exploiting long range surface plasmons (LRSPs), optical waveguide modes, and highly swollen responsive poly(N-isopropylacrylamide) (NIPAAm)-based hydrogel binding matrix. The achievements of this work cover following three key areas:

1. Optimization of LRSP-supporting layer structure was carried out in order to minimize the scattering losses of LRSPs and maximize the electromagnetic field intensity enhancement associated with the excitation of these modes for LRSP field-enhanced fluorescence spectroscopy (LRSP-FS) biosensing. In particular, the characteristics of thin gold films deposited by thermal evaporation on Cytop fluoropolymer layer were examined and there was investigated how they affect the performance of biosensors based on surface plasmon resonance (SPR) and surface plasmon-enhanced fluorescence spectroscopy (SPFS) employing the excitation of long range surface plasmons (LRSPs). We observed that the roughness of gold films deposited on Cytop is higher compared to that for gold films deposited on glass due to the low surface energy of Cytop fluoropolymer. The increasing surface energy of Cytop by etching with O_2 plasma allowed the preparation of smoother and more compact gold films. The prepared layer structures were used for the SPR and SPFS-based observation of affinity binding of protein molecules to the sensor surface that was modified by mixed thiol SAM. The results revealed that the gold roughness affects the binding capacity and non-specific interactions of protein molecules with the surface. By using the prepared structures for excitation of LRSPs, approximately two-fold increased enhancement of electric intensity field and fluorescence signal in close proximity to the surface was observed with respect to conventional SPFS. The simulations predict that further improving of the quality gold films on Cytop surfaces would allow for additional three-fold increasing the enhancement of electric intensity field through the excitation of LRSP on a surface of studied SPFS biosensor.

2. NIPAAm-based hydrogel binding matrix was implementated for highly sensitive detection of molecular analytes based on fluorescence (long range surface plasmon and hydrogel optical waveguide-enhanced fluorescence spectroscopy) and for monitoring of binding-induced refractive index changes (hydrogel optical waveguide spectroscopy). The experimental and theoretical study revealed that for detection of target analyte with maximum sensitivity, a delicate design of three-dimensional hydrogel binding matrix needs to be carried out. Particularly, the interplay of parameters including the profile of a probing wave, diffusion characteristics of an analyte to and through a gel, overall binding capacity and affinity rate constants k_a and k_d have to be taken to account. In a model immunoassay experiments, the limit of detection below 20 fM was achieved for optimized hydrogel matrix and long range surface plasmon and hydrogel optical waveguide field-enhanced fluorescence spectroscopy. The presented data indicate that large binding capacity schemes would be particularly beneficial for biosensing with lower-affinity biomolecular recognition elements or small molecules that diffuse fast from sample to the sensor surface and through the hydrogel binding matrix.

3. A new biosensor platform for ultra-sensitive detection of bacterial pathogens was developed based on long range surface plasmon-enhanced fluorescence spectroscopy (LRSP-FS). The performance characteristics of this method were evaluated for *E. coli* O157:H7, and the limit of detection of LOD = 6 cfu mL^{-1} and detection time of 40 min per test were achieved. High specificity was demonstrated by the reference measurement in which the biosensor did not show any response for *E. coli* K12. With respect to conventional SPR biosensor technology, of about 3-4 orders of magnitude lower limit of detection was achieved and it is within the range required by regulatory bodies for the analysis of samples relevant to food control.

Bibliography

[1] S. J. Updike and G. P. Hicks. Enzyme electrode. *Nature*, 214(5092):986–, 1967.

[2] A. P. F. Turner. Biochemistry - biosensors sense and sensitivity. *Science*, 290(5495):1315–1317, 2000.

[3] S. H. North, E. H. Lock, C. R. Taitt, and S. G. Walton. Critical aspects of biointerface design and their impact on biosensor development. *Analytical and Bioanalytical Chemistry*, 397(3):925–933, 2010.

[4] A. Chikoti and J. A. Hubbell. Biointerface science. *MRS Bulletin*, 30:175–179, 2005.

[5] L. Tiefenauer and R. Ros. Biointerface analysis on a molecular level - new tools for biosensor research. *Colloids and Surfaces B-Biointerfaces*, 23(2-3):95–114, 2002.

[6] H. M. Haake, A. Schutz, and G. Gauglitz. Label-free detection of biomolecular interaction by optical sensors. *Fresenius Journal of Analytical Chemistry*, 366(6-7):576–585, 2000.

[7] F. Ligler and C. Taitt. *Optical Biosensors: Present and Future*. Elsevier Science, Amsterdam, 1 edition, 2002.

[8] J. Homola. Present and future of surface plasmon resonance biosensors. *Analytical and Bioanalytical Chemistry*, 377:528–539, 2003.

[9] M. A. Gonzalez-Martinez, R. Puchades, and A. Maquieira. Optical immunosensors for environmental monitoring: How far have we come. *Analytical and Bioanalytical Chemistry*, 387(1):205–218, 2007.

[10] A. Rasooly and K. E. Herold. Biosensors for the analysis of food- and waterborne pathogens and their toxins. *Journal of Aoac International*, 89(3):873–883, 2006.

[11] T. Vo-Dinh and B. Cullum. Biosensors and biochips: advances in biological and medical diagnostics. *Fresenius Journal of Analytical Chemistry*, 366(6-7):540–551, 2000.

[12] B. Liedberg, C. Nylander, and I. Lundstrom. Surface-plasmon resonance for gas-detection and biosensing. *Sensors and Actuators*, 4(2):299–304, 1983.

[13] R. Karlsson. Spr for molecular interaction analysis: a review of emerging application areas. *Journal of Molecular Recognition*, 17(3):151–161, 2004.

[14] Jiri Homola. *Surface Plasmon Resonance Based Sensors*, volume 04 of *Chemical sensors and biosensors*. Springer-Verlag, New York, 2006.

[15] M. , K. Usui-Aoki, and H. Koga. Label-free detection of proteins in crude cell lysate with antibody arrays by a surface plasmon resonance imaging technique. *Analytical Chemistry*, 77(22):7115–7121, 2005.

[16] L. G. Carrascosa, A. Calle, and L. M. Lechuga. Label-free detection of dna mutations by spr: application to the early detection of inherited breast cancer. *Analytical and Bioanalytical Chemistry*, 393(4):1173–1182, 2009.

[17] E. A. Smith, W. D. Thomas, L. L. Kiessling, and R. M. Corn. Surface plasmon resonance imaging studies of protein-carbohydrate interactions. *Journal of the American Chemical Society*, 125(20):6140–6148, 2003.

[18] J. Melendez, R. Carr, D. U. Bartholomew, K. Kukanskis, J. Elkind, S. Yee, C. Furlong, and R. Woodbury. A commercial solution for surface plasmon sensing. *Sensors and Actuators B-Chemical*, 35(2-1):212–216, 1996.

[19] J. L. Elkind, D. I. Stimpson, A. A. Strong, D. U. Bartholomew, and J. L. Melendez. Integrated analytical sensors: the use of the tispr-1 as a biosensor. *Sensors and Actuators B-Chemical*, 54(2-1):182–190, 1999.

[20] X. D. Hoa, A. G. Kirk, and M. Tabrizian. Towards integrated and sensitive surface plasmon resonance biosensors: A review of recent progress. *Biosensors and Bioelectronics*, 23(2):151–160, 2007.

[21] R. Slavik and J. Homola. Ultrahigh resolution long range surface plasmon-based sensor. *Sensors and Actuators B-Chemical*, 123(1):10–12, 2007.

[22] T. Liebermann and W. Knoll. Surface-plasmon field-enhanced fluorescence spectroscopy. *Colloids and Surfaces a-Physicochemical and Engineering Aspects*, 171(1-3):115–130, 2000.

[23] F. Yu, B. Persson, S. Lofas, and W. Knoll. Attomolar sensitivity in bioassays based on surface plasmon fluorescence spectroscopy. *Journal of the American Chemical Society*, 126(29):8902–8903, 2004.

[24] D. Marcuse. *Integrated opticas*. IEEE Press, New York, 1973.

[25] A. W. Snyder and J. D. Love. Optical waveguide theories. In *Science paperbacks 190*, page 734. Chapman and Hall, London, 1983.

[26] D. Marcuse. *Theory of dielectric optical waveguides*. Academic, New York, 1974.

[27] D. Sarid. Long-range surface-plasma wave on very thin metal films. *Physical Review Letters*, 47:1927–1930, 1981.

[28] A. Kasry and W. Knoll. Long range surface plasmon fluorescence spectroscopy. *Applied Physics Letters*, 89(10):3, 2006.

[29] W. Knoll. Interfaces and thin films as seen by bound electromagnetic waves. *Annual Review of Physics and Chemistry*, 49:569–638, 1998.

[30] J. Homola, I. Koudela, and S. S. Yee. Surface plasmon resonance sensors based on diffraction gratings and prism couplers: sensitivity comparison. *Sensors and Actuators B-Chemical*, 54(1-2):16–24, 1999.

[31] B. Liedberg, I. Lundstrom, and E. Stenberg. Principles of biosensing with an extended coupling matrix and surface-plasmon resonance. *Sensors and Actuators B-Chemical*, 11(1-3):63–72, 1993.

[32] S. C. Kitson, W. L. Banes, J. R. Sambles, and N. P. K. Cotter. Excitation of molecular fluorescence via surface plasmon polaritons. *Journal of Modern Optics*, 43(3):573–582, 1996.

[33] K. Vasilev, W. Knoll, and M. Kreiter. Fluorescence intensities of chromophores in front of a thin metal film. *Journal of Chemical Physics*, 120(7):3439–3445, 2004.

[34] W. H. Weber and C. F. Eagen. Energy transfer from an excited dye molecule to the surface plasmons of an adjacent metal. *Optical Letters*, 4(236):236–238, 1979.

[35] N. Calander. Theory and simulation of surface plasmon-coupled directional emission from fluorophores at planar structures. *Analytical Chemistry*, 76(8):2168–2173, 2004.

[36] J. C. Love, L. A. Estroff, J. K. Kriebel, R. G. Nuzzo, and G. M. Whitesides. Self-assembled monolayers of thiolates on metals as a form of nanotechnology. *Chemical Reviews*, 105(4):1103–1169, 2005.

[37] E. Ostuni, R. G. Chapman, R. E. Holmlin, S. Takayama, and G. M. Whitesides. A survey of structure-property relationships of surfaces that resist the adsorption of protein. *Langmuir*, 17(18):5605–5620, 2001.

[38] E. Ostuni, R. G. Chapman, M. N. Liang, G. Meluleni, G. Pier, D. E. Ingber, and G. M. Whitesides. Self-assembled monolayers that resist the adsorption of proteins and the adhesion of bacterial and mammalian cells. *Langmuir*, 17(20):6336–6343, 2001.

[39] R. E. Holmlin, X. X. Chen, R. G. Chapman, S. Takayama, and G. M. Whitesides. Zwitterionic sams that resist nonspecific adsorption of protein from aqueous buffer. *Langmuir*, 17(9):2841–2850, 2001.

[40] R. L. C. Wang, H. J. Kreuzer, and M. Grunze. Molecular conformation and solvation of oligo(ethylene glycol)-terminated self-assembled monolayers and their resistance to protein adsorption. *Journal of Physical Chemistry B*, 101(47):9767–9773, 1997.

[41] P. Harder, M. Grunze, R. Dahint, G. M. Whitesides, and P. E. Laibinis. Molecular conformation in oligo(ethylene glycol)-terminated self-assembled monolayers on gold and silver surfaces determines their ability to resist protein adsorption. *Journal of Physical Chemistry B*, 102(2):426–436, 1998.

[42] S. F. Chen, J. Zheng, L. Y. Li, and S. Y. Jiang. Strong resistance of phosphorylcholine self-assembled monolayers to protein adsorption: Insights into nonfouling properties of zwitterionic materials. *Journal of the American Chemical Society*, 127(41):14473–14478, 2005.

[43] S. D. Carrigan and M. Tabrizian. Reducing nonspecific adhesion on cross-linked hydrogel platforms for real-time immunoassay in serum. *Langmuir*, 21(26):12320–12326, 2005.

[44] T. Ekblad, O. Andersson, F. I. Tai, T. Ederth, and B. Liedberg. Lateral control of protein adsorption on charged polymer gradients. *Langmuir*, 25(6):3755–3762, 2009.

[45] B. T. Houseman, J. H. Huh, S. J. Kron, and M. Mrksich. Peptide chips for the quantitative evaluation of protein kinase activity. *Nature Biotechnology*, 20(3):270–274, 2002.

[46] B. V. Slaughter, S. S. Khurshid, O. Z. Fisher, A. Khademhosseini, and N. A. Peppas. Hydrogels in regenerative medicine. *Advanced Materials*, 21(32-33):3307–3329, 2009.

[47] A. K. Bajpai, S. K. Shukla, S. Bhanu, and S. Kankane. Responsive polymers in controlled drug delivery. *Progress in Polymer Science*, 33(11):1088–1118, 2008.

[48] M. Guenther Gerlach and G. Hydrogels for chemical sensors. In G.A. Urban, editor, *Hydrogel sensors and actuators*, volume 6 of *Chemical Sensors and Biosensors*, page 165. Springer, Heidelberg, 2009.

[49] I. Tokarev and S. Minko. Stimulli-responsive hydrogel thin films. *Soft Matter*, 5:511–524, 2009.

[50] S. M. Murphy, C. J. Hamilton, M. L. Davies, and B. J. Tighe. Polymer membranes in clinical sensor applications 2. the design and fabrication of permselective hydrogels for electrochemical devices. *Biomaterials*, 13(14):979–990, 1992.

[51] Y. Wang, C. J. Huang, U. Jonas, T. X. Wei, J. , and W. Knoll. Biosensor based on hydrogel optical waveguide spectroscopy. *Biosens. Bioelectron.*, 25(7):1663–1668, 2010.

[52] O. Andersson, A. Larsson, T. Ekblad, and B. Liedberg. Gradient hydrogel matrix for microarray and biosensor applications: An imaging spr study. *Biomacromolecules*, 10(1):142–148, 2009.

[53] N. Yang, X. Sub, V. Tjong, and W. Knoll. Evaluation of two- and three-dimensional streptavidin binding platforms for surface plasmon resonance spectroscopy studies of dna hybridization and protein¡vdna binding. *Biosensors and Bioelectronics*, 22:2700¡V2706, 2008.

[54] J. Berger, M. Reist, J. M. Mayer, O. Felt, N. A. Peppas, and R. Gurny. Structure and interactions in covalently and ionically crosslinked chitosan hydrogels for biomedical applications. *Eur. J.Pharm. Biopharm.*, 57(1):19–34, 2004.

[55] N. Li, Z. Z. Liu, and S. G. Xu. Dynamically formed poly (vinyl alcohol) ultrafiltration membranes with good anti-fouling characteristics. *J. Membrane Sci.*, 169(1):17–28, 2000.

[56] A. Bakshi, O. Fisher, T. Dagci, B. T. Himes, I. Fischer, and A. Lowman. Mechanically engineered hydrogel scaffolds for axonal growth and angiogenesis after transplantation in spinal cord injury. *J. Neurosurg.-Spine*, 1(3):322–329, 2004.

[57] M. Guvendiren, S. Yang, and J. A. Burdick. Swelling-induced surface patterns in hydrogels with gradient crosslinking density. *Adv. Funct. Mater.*, 19(19):3038–3045, 2009.

[58] I. Tokarev, I. Tokareva, and S. Minko. Gold-nanoparticle-enhanced plasmonic effects in a responsive polymer gel. *Adv. Mater.*, 20(14):2730–2734, 2008.

[59] K. Ishihara, M. Kobayashi, N. Ishimaru, and I. Shinohara. Glucose induced permeation control of insulin through complexmembrane consisting of immobilized glucose oxidase and a poly(amine). *Polym. J.*, 16(625-631), 1984.

[60] P. W. Beines, I. Klosterkamp, B. Menges, U. Jonas, and W. Knoll. Responsive thin hydrogel layers from photo-cross-linkable poly(n-isopropylacrylamide) terpolymers. *Langmuir*, 23(4):2231–2238, 2007.

[61] C. L. Smith, J. S. Milea, and G. H. Nguyen. Immobilization of nucleic acids using biotin-strept(avidin) systems. In *Immobilisation of DNA on Chips Ii*, volume 261 of *Topics in Current Chemistry*, pages 63–90. Springer-Verlag Berlin, Berlin, 2005.

[62] J. Turkova. Oriented immobilization of biologically active proteins as a tool for revealing protein interactions and function. *Journal of Chromatography B*, 722(1-2):11–31, 1999.

[63] L. G. Fagerstam, A. Frostellkarlsson, R. Karlsson, B. Persson, and I. Ronnberg. Biospecific interaction analysis using surface-plasmon resonance detection applied to kinetic, binding-site and concentration analysis. *Journal of Chromatography*, 597(1-2):397–410, 1992.

[64] Y. S. N. Day, C. L. Baird, R. L. Rich, and D. G. Myszka. Direct comparison of binding equilibrium, thermodynamic, and rate constants determined by surface- and solution-based biophysical methods. *Protein Science*, 11(5):1017–1025, 2002.

[65] S. Sjolander and C. Urbaniczky. Integrated fluid handling-system for biomolecular interaction analysis. *Analytical Chemistry*, 63(20):2338–2345, 1991.

[66] D. A. Edwards, B. Goldstein, and D. S. Cohen. Transport effects on surface-volume biological reactions. *Journal of Mathematical Biology*, 39(6):533–561, 1999.

[67] K. R. Gee, E. A. Archer, and H. C. Kang. 4-sulfotetrafluorophenyl (stp) esters: New water-soluble amine-reactive reagents for labeling biomolecules. *Tetrahedron Letters*, 40(8):1471–1474, 1999.

[68] W. Knoll, M. Zizlsperger, T. Liebermann, S. Arnold, A. Badia, M. Liley, D. Piscevic, F. J. Schmitt, and J. Spinke. Streptavidin arrays as supramolecular architectures in surface-plasmon optical sensor formats. *Colloids and Surfaces a-Physicochemical and Engineering Aspects*, 161(1):115–137, 2000.

[69] A. Aulasevich, R.F. Roskamp, U. Jonas, B. Menges, J. Dostalek, and W. Knoll. Optical waveguide spectroscopy for the investigation of protein-funcionalized hydrogel films. *Macromolecular Rapid Communications*, 30:872–877, 2009.

[70] P. Yeh. *Optical waves in layered media*. John Wiley and Sons, New York, 1998.

[71] A. Boltasseva, T. Nikolajsen, K. Leosson, K. Kjaer, M. S. Larsen, and S. I. Bozhevol-nyi. Integrated optical components utilizing long-range surface plasmon polaritons. *Journal of Lightwave Technology*, 23(1):413–422, 2005.

[72] R. Charbonneau, C. Scales, I. Breukelaar, S. Fafard, N. Lahoud, G. Mattiussi, and P. Berini. Passive integrated optics elements used on long-range surface plasmon polaritons. *Journal of Lightwave Technology*, 24(1):477–494, 2006.

[73] H. J. Simon, Y. Wang, L. B. Zhou, and Z. Chen. Coherent backscattering of optical 2nd-harmonic generation with long-range surface-plasmons. *Optics Letters*, 17(18):1268–1270, 1992.

[74] G. Winter, S. Wedge, and W. L. Barnes. Can lasing at visible wavelengths be achieved using the low-loss long-range surface plasmon-polariton mode? *New Journal of Physics*, 8, 2006.

[75] T. Okamoto, J. Simonen, and S. Kawata. Plasmonic band gaps of structured metallic thin films evaluated for a surface plasmon laser using the coupled-wave approach. *Physical Review B*, 77(11), 2008.

[76] T. Inagaki, M. Motosuga, E. T. Arakawa, and J. P. Goudonnet. Coupled surface-plasmons in periodically corrugated thin silver films. *Physical Review B*, 32(10):6238–6245, 1985.

[77] J. Dostalek, R. F. Roskamp, and W. Knoll. Coupled long range surface plasmons for the investigation of thin films and interfaces. *Sensors and Actuators B: Chemical*, 139(1):9–12, 2009.

[78] K. Matsubara, S. Kawata, and S. Minami. Multilayer system for a high-precision surface-plasmon resonance sensor. *Optics Letters*, 15(1):75–77, 1990.

[79] G. G. Nenninger, P. Tobiska, J. Homola, and S. S. Yee. Long-range surface plasmons for high-resolution surface plasmon resonance sensors. *Sensors and Actuators B-Chemical*, 74(1-3):145–151, 2001.

[80] J. Dostalek, A. Kasry, and W. Knoll. Long range surface plasmons for observation of biomolecular binding events at metallic surfaces. *Plasmonics*, 2(3):97–106, 2007.

[81] A. W. Wark, H. J. Lee, and R. M. Corn. Long-range surface plasmon resonance imaging for bioaffinity sensors. *Analytical Chemistry*, 77(13):3904–3907, 2005.

[82] J. Dostalek and W. Knoll. Biosensors based on surface plasmon-enhanced fluorescence spectroscopy. *Biointerphases*, 3(3):FD12–FD22, 2008.

[83] P. D. Keathley and J. T. Hastings. Optical properties of sputtered fluorinated ethylene propylene ands its application to surface-plasmon resonance sensor fabrication. *J. Vac. Sci. Technol. B*, 26(6):2473–2477, 2008.

[84] M Vala, J. Dostalek, and J. Homola. Diffraction grating-coupled surface plasmon resonance sensor based on spectroscopy of long-range and short-range surface plasmons. *SPIE*, 6585:658522–1, 2007.

[85] S. R. Kim. Surface modification of poly(tetrafluoroethylene) film by chemical etching, plasma, and ion beam treatments. *Journal of Applied Polymer Science*, 77(9):1913–1920, 2000.

[86] M. A. Ordal, L. L. Long, R. J. Bell, S. E. Bell, R. R. Bell, R. W. Alexander, and C. A. Ward. Optical-properties of the metals al, co, cu, au, fe, pb, ni, pd, pt, ag, ti, and w in the infrared and far infrared. *Applied Optics*, 22(7):1099–1119, 1983.

[87] E.D. Palik. *Handbook of Optical Constants of Solids*. Academic press, New York, 1985.

[88] A. Rueda, N. Vogel, and M. Kreiter. Characterization of gold films by surface plasmon spectroscopy: Large errors and small consequences. *Surface Science*, 603:491–497, 2009.

[89] G. M. Hale and M. R. Querry. Optical-constants of water in 200-nm to 200-mum wavelength region. *Applied Optics*, 12(3):555–563, 1973.

[90] F. Horkay, P. J. Basser, A. M. Hecht, and E. Geissler. Osmotic and sans observations on sodium polyacrylate hydrogels in physiological salt solutions. *Macromolecules*, 33(22):8329–8333, 2000.

[91] A. R. Khare and N. A. Peppas. Swelling deswellling of anionic copolymer gels. *Biomaterials*, 16(7):559–567, 1995.

[92] J. Ostroha, M. Pong, A. Lowman, and N. Dan. Controlling the collapse/swelling transition in charged hydrogels. *Biomaterials*, 25(18):4345–4353, 2004.

[93] D.A. Edwards. The effect of a receptor layer on the measurement of rate constants. *Bull. Math. Biol.*, 63:301–327, 2001.

[94] P. Schuck. Kinetics of ligand binding to receptor immobilized in a polymer matrix, as detected with an evanescent wave biosensor .1. a computer simulation of the influence of mass transport. *Biophysical Journal*, 70(3):1230–1249, 1996.

[95] V. Sikavitsas, J.M. Nitsche, and T.J. Mountziaris. Transport and kinetic processes underlying biomolecular interactions in the biacore biosensor. *Biotechnol. Prog.*, 18:885–897, 2002.

[96] C.J. Huang, J. Dostalek, and W. Knoll. Optimization of layer structure supporting long range surface plasmons for surface plasmon-enhanced fluorescence spectroscopy biosensors. *Journal of Vacuum Science and Technology B*, 28(1):66–72, 2010.

[97] G. E. Perlmann and L. G. Longsworth. The specific refractive increment of some purified proteins. *Journal of American Chemical Society*, 70(8):2719¡V2724, 1948.

[98] T. Jossang, J. Feder, and E. Rosenqvist. Photon correlation spectroscopy of human igg. *J. Proten. Chem.*, 7(2):1573–4943, 1988.

[99] C. Vollenkle, S. Weigert, N. Ilk, E. Egelseer, V. Weber, F. Loth, D. Falkenhagen, U. B. Sleytr, and M. Sara. Construction of a functional s-layer fusion protein comprising an immunoglobulin g-binding domain for development of specific adsorbents for extracorporeal blood purification. *Applied and Environmental Microbiology*, 70(3):1514–1521, 2004.

[100] F. Yu, B. Persson, S. Lofas, and W. Knoll. Surface plasmon fluorescence immunoassay of free prostate-specific antigen in human plasma at the femtomolar level. *Analytical Chemistry*, 76(22):6765–6770, 2004.

[101] R Raccis. Phd. thesis.

[102] X. D. Fan, I. M. White, S. I. Shopoua, H. Y. Zhu, J. D. Suter, and Y. Z. Sun. Sensitive optical biosensors for unlabeled targets: A review. *Analytica Chimica Acta*, 620(1-2):8–26, 2008.

[103] G. Gauglitz. Direct optical sensors: principles and selected applications. *Analytical and Bioanalytical Chemistry*, 381(1):141–155, 2005.

[104] W. Knoll, A. Kasry, F. Yu, Y. Wang, A. Brunsen, and J. Dostalek. New concepts with surface plasmons and nano-biointerfaces. *Journal of Nonlinear Optical Physics and Materials*, 17(2):121–129, 2008.

[105] Y. Wang, A. Brunsen, U. Jonas, J. Dostalek, and W. Knoll. Prostate specific antigen biosensor based on long range surface plasmon-enhanced fluorescence spectroscopy and dextran hydrogel binding matrix. *Analytical Chemistry*, 81(23):9625–9632, 2009.

[106] D. Kuckling and P. Pareek. Bilayer hydrogel assembly. *Polymer*, 49(6):1435–1439, 2008.

[107] S. K. Ghosh and T. Pal. Interparticle coupling effect on the surface plasmon resonance of gold nanoparticles: From theory to applications. *Chemical Reviews*, 107(11):4797–4862, 2007.

[108] Jonas U. Dostalek J. Knoll W. Huang, C.J. Biosensor platform based on surface plasmon-enhanced fluorescence spectroscopy and responsive hydrogel binding matrix. *Proc. SPIE*, 7356:735625, 2009.

[109] F. Xu, B. Persson, S. Lofas, and W. Knoll. Surface plasmon optical studies of carboxymethyl dextran brushes versus networks. *Langmuir*, 22(7):3352–3357, 2006.

[110] L. A. Cole. New discoveries on the biology and detection of human chorionic gonadotropin. *Reproductive Biology and Endocrinology*, 7:37, 2009.

[111] L. A. Cole, D. H. Dai, S. A. Butler, K. K. Leslie, and E. I. Kohorn. Gestational trophoblastic diseases: 1. pathophysiology of hyperglycosylated hcg. *Gynecologic Oncology*, 102(2):145–150, 2006.

[112] S. A. Butler, M. S. Ikram, S. Mathieu, and R. K. Iles. The increase in bladder carcinoma cell population induced by the free beta subunit of human chorionic gonadotrophin is a result of an anti-apoptosis effect and not cell proliferation. *British Journal of Cancer*, 82(9):1553–1556, 2000.

[113] R. K. Iles. Ectopic hcg beta expression by epithelial cancer: Malignant behaviour, metastasis and inhibition of tumor cell apoptosis. *Molecular and Cellular Endocrinology*, 260:264–270, 2007.

[114] M. L. M. Vareiro, J. Liu, W. Knoll, K. Zak, D. Williams, and A. T. A. Jenkins. Surface plasmon fluorescence measurements of human chorionic gonadotrophin: Role of antibody orientation in obtaining enhanced sensitivity and limit of detection. *Analytical Chemistry*, 77(8):2426–2431, 2005.

[115] K. S. Gracias and J. L. McKillip. A review of conventional detection and enumeration methods for pathogenic bacteria in food. *Canadian Journal of Microbiology*, 50(11):883–890, 2004.

[116] S. Yaron and K. R. Matthews. A reverse transcriptase-polymerase chain reaction assay for detection of viable escherichia coli o157 : H7: investigation of specific target genes. *Journal of Applied Microbiology*, 92(4):633–640, 2002.

[117] A. D. Taylor, Q. M. Yu, S. F. Chen, J. Homola, and S. Y. Jiang. Comparison of e-coli o157 : H7 preparation methods used for detection with surface plasmon resonance sensor. *Sensors and Actuators B-Chemical*, 107(1):202–208, 2005.

[118] B. K. Oh, W. Lee, W. H. Lee, and J. W. Choi. Nano-scale probe fabrication using self-assembly technique and application to detection of escherichia coli o157 : H7. *Biotechnology and Bioprocess Engineering*, 8(4):227–232, 2003.

[119] P. M. Fratamico, T. P. Strobaugh, M. B. Medina, and A. G. Gehring. Detection of escherichia coli o157 : H7 using a surface plasmon resonance biosensor. *Biotechnology Techniques*, 12(7):571–576, 1998.

[120] V. Koubova, E. Brynda, L. Karasova, J. Skvor, J. Homola, J. Dostalek, P. Tobiska, and J. Rosicky. Detection of foodborne pathogens using surface plasmon resonance biosensors. *Sensors and Actuators B-Chemical*, 74(1-3):100–105, 2001.

[121] A. D. Taylor, J. Ladd, Q. M. Yu, S. F. Chen, J. Homola, and S. Y. Jiang. Quantitative and simultaneous detection of four foodborne bacterial pathogens with a multi-channel spr sensor. *Biosensors and Bioelectronics*, 22(5):752–758, 2006.

[122] O. Tokarskyy and D. L. Marshall. Immunosensors for rapid detection of escherichia coli o157 : H7 - perspectives for use in the meat processing industry. *Food Microbiology*, 25(1):1–12, 2008.

[123] S. C. Kuo, D. A. Hammer, and D. A. Lauffenburger. Simulation of detachment of specifically bound particles from surfaces by shear flow. *Biophysical Journal*, 73(1):517–531, 1997.

[124] Z. J. Li, N. Mohamed, and J. M. Ross. Shear stress affects the kinetics of staphylococcus aureus adhesion to collagen. *Biotechnology Progress*, 16(6):1086–1090, 2000.

[125] C. Verdier, C. Couzon, A. Duperray, and P. Singh. Modeling cell interactions under flow. *Journal of Mathematical Biology*, 58(1-2):235–259, 2009.

[126] M. D. Zordan, M. M. G. Grafton, G. Acharya, L. M. Reece, C. L. Cooper, A. I. Aronson, K. Park, and J. F. Leary. Detection of pathogenic e. coli o157:h7 by a hybrid microfluidic spr and molecular imaging cytometry device. *Cytometry Part A*, 75A(2):155–162, 2009.

[127] A. Ghubade, S. Mandal, R. Chaudhury, R. K. Singh, and S. Bhattacharya. Dielectrophoresis assisted concentration of micro-particles and their rapid quantitation based on optical means. *Biomedical Microdevices*, 11(5):987–995, 2009.

[128] L. J. Yang. Dielectrophoresis assisted immuno-capture and detection of foodborne pathogenic bacteria in biochips. *Talanta*, 80(2):551–558, 2009.

[129] N.S. Eum, S.H Yeom, D.H. Kwon, and S.W. Kang. Enhancement of sensitivity using gold nanorods-antibody conjugation of e.coli o157:h7. *Sensors and Actuators B-Chemical*, 143:784–788, 2010.

[130] M. Vala, S. Etheridge, J. A. Roach, and J. Homola. Long-range surface plasmons for sensitive detection of bacterial analytes. *Sensors and Actuators B-Chemical*, 139(1):59–63, 2009.

[131] A. G. Gehring, D. M. Albin, A. K. Bhunia, S. A. Reed, S. I. Tu, and J. Uknalis. Antibody microarray detection of escherichia coli o157 : H7: Quantification, assay limitations, and capture efficiency. *Analytical Chemistry*, 78(18):6601–6607, 2006.

[132] J. M. Simpson-Stroot, E. A. Kearns, P. G. Stroot, S. Magana, and D. V. Lim. Monitoring biosensor capture efficiencies: Development of a model using gfp-expressing escherichia coli o157 : H7. *Journal of Microbiological Methods*, 72(1):29–37, 2008.

[133] J. D. Brewster, A. G. Gehring, R. S. Mazenko, L. J. VanHouten, and C. J. Crawford. Immunoelectrochemical assays for bacteria: Use of epifluorescence microscopy and rapid-scan electrochemical techniques in development of an assay for salmonella. *Analytical Chemistry*, 68(23):4153–4159, 1996.

[134] A. E. Balaev, K. N. Dvoretski, and V. A. Doubrovski. Refractive index of escherichia coli cells. In V. V. Tuchin, editor, *Saratov Fall Meeting 2001: Optical Technologies in Biophysics and Medicine Iii*, volume 4707 of *Proceedings of the Society of Photo-Optical Instrumentation Engineers (Spie)*, pages 253–260. Spie-Int Soc Optical Engineering, Bellingham, 2001.

[135] M. Strigl, D. A. Simson, C. M. Kacher, and R. Merkel. Force-induced dissociation of single protein a-igg bonds. *Langmuir*, 15(21):7316–7324, 1999.

[136] P. Singleton. *Bacteria in Biology, Biotechnology and Medicne*. John Wiley and Sons, 3rd edition, 1995.

[137] H. D. Kovacs and K. Rasky. Testing of a chemiluminescence enzyme immunoassay for selective detection of e-coli o157 from ground beef samples. *Acta Veterinaria Hungarica*, 49(4):377–383, 2001.

[138] A. K. Deisingh and M. Thompson. Strategies for the detection of escherichia coli o157 : H7 in foods. *Journal of Applied Microbiology*, 96(3):419–429, 2004.

[139] O. Lazcka, F. J. Del Campo, and F. X. Munoz. Pathogen detection: A perspective of traditional methods and biosensors. *Biosensors and Bioelectronics*, 22(7):1205–1217, 2007.

List of Figures

List of Tables